

# The Unified Autonomy Stack: Toward a Blueprint for Generalizable Robot Autonomy

Journal Title  
XX(X):1–35  
©The Author(s) 2026  
Reprints and permission:  
sagepub.co.uk/journalsPermissions.nav  
DOI: 10.1177/ToBeAssigned  
www.sagepub.com/

SAGE

Mihir Dharmadhikari\*, Nikhil Khedekar\*, Mihir Kulkarni\*, Morten Nissov\*, Martin Jacquet, Angelos Zacharia, Marvin Harms, Albert Gassol Puigjaner, Philipp Weiss, Kostas Alexis

## Abstract

We introduce and open-source the *Unified Autonomy Stack*, a system-level solution that enables resilient autonomy across diverse aerial and ground robot morphologies. The architecture centers on three synergistic modules –multi-modal perception, multi-behavior planning, and multi-layered safe navigation– that together deliver comprehensive mission autonomy. The stack fuses data from LiDAR, radar, vision, and inertial sensing, enabling (a) robust localization and mapping through factor graph-based fusion, (b) semantic scene understanding, (c) motion and informative path planning through sampling-based techniques adaptive across spatial scales, as well as (d) multi-layered safe navigation both through planning on the online reconstructed map and deep learning-driven exteroceptive policies alongside last-resort safety filters using control barrier functions. The resulting behaviors include safe GNSS-denied navigation into unknown and perceptually-degraded regions, exploration of complex environments, object discovery, and efficient inspection planning. The stack has been field-tested and validated on both aerial (rotorcraft) and ground (legged) robots operating in a host of demanding environments, including self-similar and smoke-filled settings, with complex geometries and high obstacle clutter. These tests demonstrate resilient performance in challenging conditions. To facilitate ease of adoption, we open-source the implementation alongside supporting documentation, validation, and evaluation datasets [https://github.com/ntnu-arl/unified\\_autonomy\\_stack](https://github.com/ntnu-arl/unified_autonomy_stack). A video giving the overview of the paper and the field experiments is available at <https://youtu.be/l8Su8OXsM-E>.

## Keywords

Autonomy, Perception, Planning, Navigation

## 1 Introduction

Mobile robots are increasingly deployed to operate in environments where Global Navigation Satellite System (GNSS) is unavailable, perception is degraded, geometry is self-similar, and safe navigation is broadly challenged [Tranzatto et al. \(2022\)](#); [Harlow et al. \(2024\)](#); [Ebadi et al. \(2023\)](#); [Datar et al. \(2025\)](#); [Chung et al. \(2023\)](#). Although the robotics community has developed mature components for many individual functionalities such as localization, planning and control, existing autonomy stacks (e.g., the works in [Fernandez-Cortizas et al. \(2023\)](#); [Sanchez-Lopez et al. \(2016\)](#); [Baca et al. \(2021\)](#); [Mohta et al. \(2018\)](#); [Foehn et al. \(2022\)](#); [Goodin et al. \(2024\)](#); [AirLab \(2025\)](#); [Real et al. \(2020\)](#)) remain largely specialized to a particular robot morphology, sensor suite, or mission class. This specialization limits reuse across platforms, makes systematic field evaluation difficult, slows the accumulation of shared deployment experience, and hinders both consolidation and broader uptake of autonomy across robot categories.

At the same time, limited attention has been given to feature-rich autonomy stacks readily delivering complex behaviors and functionalities such as resilient GNSS-denied navigation in perceptually-degraded environments, combined with sophisticated informative path planning and assured safety ensuring robust operation across operational environments and conditions. However, recent advances

across the “sense-think-act” loop -from perception to planning and deep control policies- point toward the potential for a resilient and, to a significant extent, unified autonomy engine. Although research on universal autonomy is still in its early stages, the benefits of unification and the collective need to advance robot capabilities underscore the need for general autonomy solutions.

Motivated by the above, we present the Unified Autonomy stack (*UAsTack*), a comprehensive open-source autonomy stack that can support mission-level operation across diverse aerial and ground robot configurations. The *UAsTack* represents a step towards a common autonomy blueprint across diverse robot types -from multirotors and other rotorcrafts to ground robots such as legged systems- delivering mission-complete capabilities for navigation and complex information sampling behaviors (e.g., exploration, inspection, object discovery) in diverse settings, including in strenuous, high-risk natural and industrial environments.

All authors are affiliated with the Autonomous Robots Lab, Norwegian University of Science and Technology (NTNU), Trondheim, Norway

### Corresponding author:

Kostas Alexis, Department of Engineering Cybernetics, Norwegian University of Science and Technology, Høgskoleringen 1, Trondheim 7034, Norway. \* indicates equal contribution.

Email: [konstantinos.alexis@ntnu.no](mailto:konstantinos.alexis@ntnu.no)

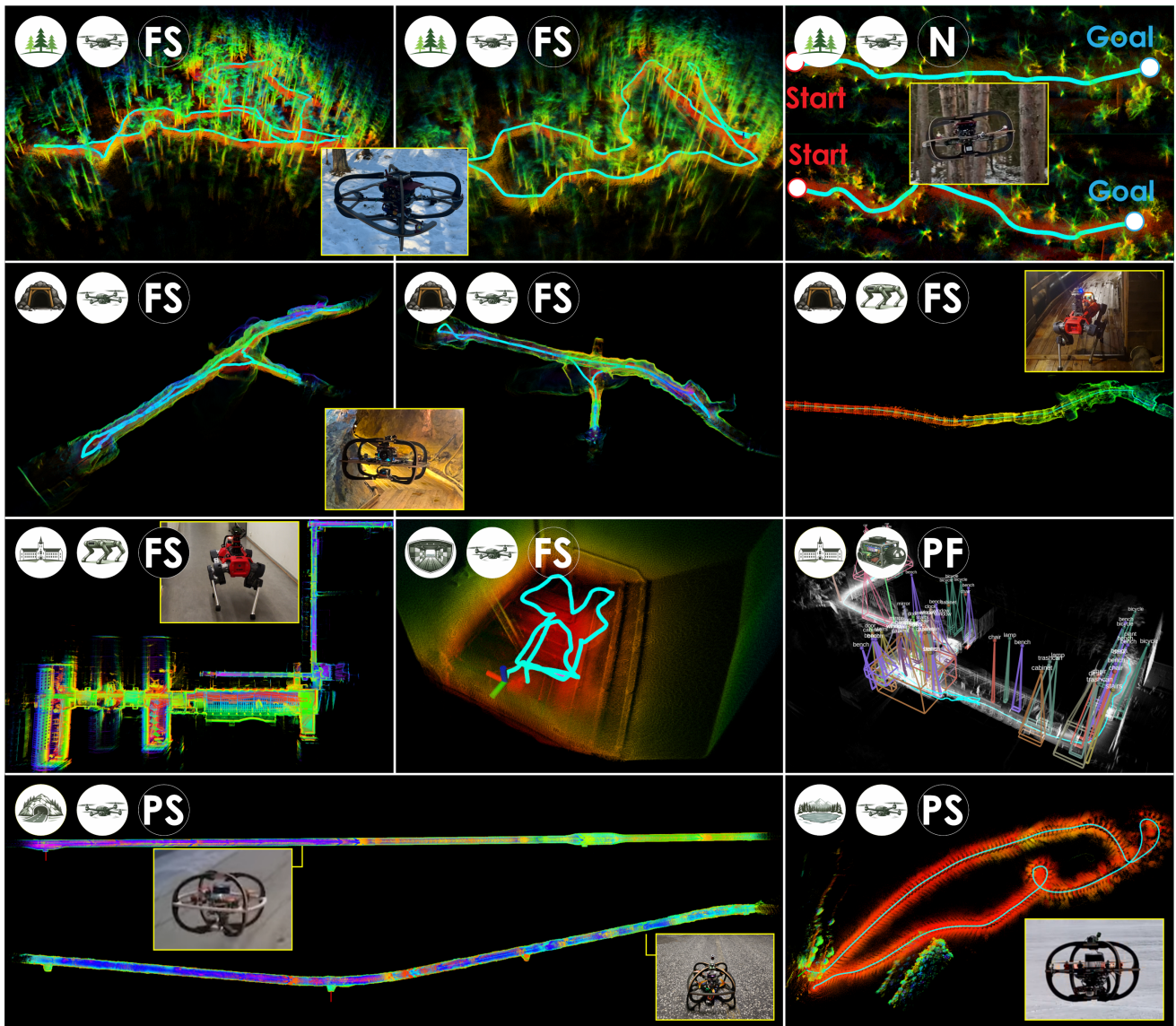


**Figure 1.** Indicative subset of the evaluation studies conducted to validate and assess the performance of the Unified Autonomy Stack. The tests involve both aerial and ground robots operating in diverse GNSS-denied and at instances perceptually-degraded environments including (a) snow-covered forests, (b) underground mines, (c) road tunnels, (d) a frozen lake, (e) ship cargo holds, as well as (f) the university campus with subsets of it filled with fog. All core modules of the autonomy stack were evaluated independently, alongside full-stack experiments. In this image “FS” stands for Full-Stack deployments (involving the synergy of the perception module, planning module, and navigation module), “N” for deployments to evaluate the navigation module, “PF” for testing both the localization and mapping as well as object-level reasoning of the perception module, while “PS” marks tests focusing only on localization and mapping. The presented instances are from a subset of the experiments as detailed in the paper. The full datasets of the experiments are also released to support verifiability.

Its design emphasizes resilience in that it presents robustness (e.g., against noisy sensor data and mapping imperfections), resourcefulness (e.g., multiple solutions for safety in navigation), and redundancy (e.g., complementary sensor data to handle single-modality failures), enabling it to retain high performance across environments and conditions, including GNSS-denied, perceptually-degraded, geometrically complex, and potentially adversarial settings that typically challenge safe navigation and mission autonomy.

The UAstack builds upon three core modules and associated contributions. The perception module is centered around a novel approach to multi-modal Simultaneous Localization And Mapping (SLAM) based on factor

graphs, enabling robust fusion of LiDAR, Frequency Modulated Continuous Wave (FMCW) radar, visual perception, and Inertial Measurement Unit (IMU) cues. This supports resilient performance in GNSS-denied environments with multiple perceptual degradations, including geometric self-similarity, low texture, icy scenes, and dense obscurants (e.g., fog, smoke). Furthermore, the perception module integrates scene reasoning through Vision-Language Models (VLMs) enabling object discovery and visual question & answering (Q&A). The planning module builds upon OmniPlanner [Zacharia et al. \(2026\)](#), facilitating target reaching, exploration, and inspection path planning through sampling-based methods over an online-derived volumetric map of the environment. It provides a versatile framework that abstracts vehicle configuration and supports diverse

mission objectives, which the planner optimizes accordingly. The navigation module builds upon the contributions in [Jacquet et al. \(2025\)](#); [Harms et al. \(2025\)](#), alongside introducing a novel approach to exteroceptive reinforcement learning for navigation. Recognizing that localization errors and mapping imperfections may arise, we adopt a redundant, multi-layered safety approach in which depth-based exteroceptive navigation policies and last-resort control barrier function-based safety filters enhance safety by providing direct and reactive collision avoidance. As a result, the UAstack is tailored to environments that challenge localization and mapping, both by leveraging sensor multi-modality to maintain perception under degraded conditions, and by implementing reactive safety mechanisms to reduce reliance on perfect scene understanding.

To evaluate the performance and assess its resilience, the UAstack is evaluated onboard multiple robot configurations and within a diverse set of environments, an indicative subset of which is shown in [Figure 1](#). First, a detailed quantitative evaluation of the perception module is presented, covering 2 urban tunnels, a frozen lake and a university campus environment characterized by geometric self-similarity, low visibility, and heavy airborne obscuration. It displays the superior performance of the perception module compared to State-of-the-Art LiDAR-Inertial, LiDAR-Radar-Inertial, LiDAR-Visual-Inertial, or Visual-Inertial SLAM methods. Object-level reasoning is assessed by building 3D scene graphs with object-level annotations, alongside enabling visual Q&A on online camera data. Next, the navigation module is evaluated in two real-world deployments. First, in a forest environment for a waypoint-navigation task requiring maneuvering to avoid trees, while map-based path planning is disabled to isolate the reactive layer. Second, we evaluate safety under map discrepancies by introducing previously unmapped obstacles along the path planned by the planning module and demonstrate that the navigation module layer can handle such unseen obstacles. These experiments highlight the importance of the multi-layered safety approach and the complementary roles of each safety method. Finally, the full UAstack is evaluated on aerial and legged robots performing autonomous exploration and inspection missions guided by the planning module. The aerial robot is deployed in a) a low-visibility, multi-branched underground mine, and b) a forest with thin obstacles and local clutter, performing exploration missions, with navigation module modalities being tested. Additionally, the aerial robot is deployed in the cargo hold of a ship performing an exploration and inspection mission. On the other hand, the legged robot is deployed in a university campus, and inside the same underground mine as the aerial robot. This demonstrates large-scale missions across heterogeneous platforms and environments.

Importantly, the Unified Autonomy Stack is open to extension, both from the perspective of the robots it readily supports and the missions it enables. Our team is targeting its full-fledged expansion to a diverse set of robot configurations and the extension of the enabled behaviors. To that end, the full implementation is open-sourced ([https://github.com/ntnu-ar1/unified\\_autonomy\\_stack](https://github.com/ntnu-ar1/unified_autonomy_stack)), alongside documentation and

supporting datasets ([https://ntnu-ar1.github.io/unified\\_autonomy\\_stack/](https://ntnu-ar1.github.io/unified_autonomy_stack/)).

The remainder of this paper is structured as follows. [Section 2](#) overviews related work in autonomy stacks. The UAstack and its modules are detailed in [Section 3](#). Evaluation studies are presented in [Section 4](#), followed by conclusions and plans for future work in [Section 5](#).

## 2 Related Work

Research in autonomy is a particularly active field. The robotics community has increasingly released reusable autonomy components, while more complete autonomy stacks remain less common. Driven by the major success of open-source autopilot releases, such as PX4 and ArduPilot [Meier et al. \(2015\)](#), these developments aim to accelerate research on robot autonomy and democratize its adoption through open implementations and standards. In this section, we review relevant literature and position how the UAstack contributes to this landscape.

Typically, major building blocks of autonomy are often documented and released as separate publications and open-source contributions. Indicative examples span SLAM [Xu et al. \(2022\)](#); [Vizzo et al. \(2023\)](#); [Koide et al. \(2024\)](#); [Campos et al. \(2021\)](#); [Geneva et al. \(2020a\)](#); [Qin et al. \(2019\)](#), motion and path planning [Sucan et al. \(2012\)](#); [Wang et al. \(2022\)](#); [Mellinger and Kumar \(2011\)](#); [Likhachev et al. \(2003\)](#), control [Verschuere et al. \(2022\)](#); [Andersson et al. \(2018\)](#); [Gifftaler et al. \(2018\)](#), robot learning [Petrenko et al. \(2020\)](#); [Makoviichuk and Makoviychuk \(2021\)](#); [Schwarke et al. \(2025\)](#); [NVIDIA et al. \(2025\)](#); [Zakka et al. \(2025\)](#), and navigation frameworks [Macenski et al. \(2020\)](#); [Planning \(2012\)](#). While these works provide an important foundation for robot autonomy, they are not the focus of this section. Instead, this section assesses and compares existing integrated, open-source autonomy stacks for mobile robots, including aerial and ground systems.

Autonomous driving is among the most mature fields in terms of integrated autonomy stacks. The Autoware Universe [Autoware Foundation \(2021\)](#); [Kato et al. \(2018\)](#) is a modular ROS2 autonomous driving stack that involves a highly-integrated perception, planning, and control solution. Apollo Auto [\(2017\)](#) is another flagship open autonomous driving project, targeting autonomy in structured urban streets. A comparative analysis of major autonomous driving stacks is provided in [Jung et al. \(2025\)](#), reflecting the broader community interest in open autonomy frameworks. Off-road autonomy is addressed in NATURE [Goodin et al. \(2024\)](#), which introduces an open-source stack, providing a self-contained pipeline with perception, global and local planning, and control components, with support for both ROS1 and ROS2.

Beyond autonomous driving, aerial robotics has seen some of the most active development of autonomy stacks. The MRS UAV System [Baca et al. \(2021\)](#) is among the most complete open-source autonomy stacks for multirotor aerial robots. It supports LiDAR-based SLAM state estimation, several control methods including SE(3) formulations and model predictive control, trajectory generation, and selected multi-robot capabilities. From a complementary perspective,

**Table 1.** Comparison with existing autonomy stacks.

Stack	Modular	Modalities <sup>1</sup>	Embodiments <sup>2</sup>	Verified <sup>3</sup>	Autonomy Features <sup>4</sup>										
					Perception			Planning			Safety				
					SLAM	OD	LQ	EP	IP	TP	M	T	Ct	LR	
AeroStack	✓	<u>C</u>	A	SL	✓	✗	✗	✗	✗	✗	✓	✓	—	✗	✗
AeroStack2	✓	C	A	SL	✗	✗	✗	✗	✗	✓	✓	—	✗	✗	✗
MRS UAV	✓	<u>C</u> <u>L</u> <u>G</u>	A	SLF	E	✗	✗	✗	✗	✓	✓	—	✗	✗	✓
Nebula	✓	<u>CL</u>	AG	SLF	✓	†	✗	†	✗	†	†	✓	✗	✗	✗
Agilicious	✓	<u>C</u>	A	SLF	✗	✗	✗	✗	✗	✓	✗	—	✗	✗	✗
KR Aut. Flight	✓	<u>CL</u>	A	SLF	✓	✗	✗	✗	✗	✓	✓	—	✗	✗	✗
NATURE	✗	L	G	SLF	✗	✗	✗	✗	✗	✓	✓	✓	✗	✗	✗
AirStack	✓	<u>CL</u>	A	SL	✓	†	✗	✓	✗	✓	†	—	†	✗	✗
Nav2	✓	<u>L</u>	G	SLF	✓	✗	✗	✗	✗	✓	✓	✓	✗	✗	✓
Autoware	✓	<u>CRLG</u>	G	SLF	✓	✓	✓	✗	✗	✓	✓	✓	✗	✗	✓
Apollo	✓	<u>CRLG</u>	G	SLF	✓	✓	✗	✗	✗	✓	✓	✓	✗	✗	✓
Ours (UAS <sub>stack</sub> )	✓	<u>CRL</u>	AG	SLF	✓	✓	✓	✓	✓	✓	✓	✓	✓	✓	✓

<sup>1</sup> Supported perception modalities, where C: camera, R: radar, L: LiDAR, G: GNSS. The underline denotes modalities which are used by SLAM, and breaks indicate non-multi-modal SLAM usage.

<sup>2</sup> Supported embodiments, where A: aerial, G: ground.

<sup>3</sup> How the autonomy stack was tested, where S: simulation, L: lab, F: field

<sup>4</sup> Presence of feature, where: ✓: feature exists and open-sourced, †: exists and not open-sourced, ✗: does not exist, E: external package integrated as is, —: not applicable

OD: Object Detection      LQ: Language Query      EP: Exploration Planning  
 IP: Inspection Planning      TP: Planning to Target      M: Map-based safety  
 T: Traversability checking      Ct: Safety at control layer      LR: Last resort safety

Aerostack2 [Fernandez-Cortizas et al. \(2023\)](#) is a ROS2-based autonomy framework for aerial robots that emphasizes standardization, modularity, and reusability. It provides replaceable and dynamically configurable components, enables behavior-based mission planning, and supports multi-robot coordination. Unlike more integrated systems, it does not provide a comprehensive perception-planning-control pipeline and does not include some components required for autonomy (e.g., a SLAM solution). Aerostack2 builds upon Aerostack [Sanchez-Lopez et al. \(2016\)](#), which was an early effort to standardize aerial robot frameworks. Going further, Aerostack2 provides better modularity, a wider set of controller/estimator options, a richer behavior tree, and is implemented in ROS 2. AirStack [AirLab \(2025\)](#) targets modular aerial autonomy and provides a research-to-deployment pipeline with tight support for testing in both simulation and reality. Released as an alpha version at the time of writing, it is not yet fully available; instead, only a subset of its modules is open at the time of writing (e.g., exploration planning, visual-inertial odometry). Following a different direction, the unmanned aerial vehicle abstraction layer (UAL) [Real et al. \(2020\)](#) contributes a layered design providing a standard API for aerial robot control and abstracts specific autopilot implementations. Through a namespaced design, it facilitates multi-robot support, but does not provide higher-level autonomy components. Agilicious [Foehn et al. \(2022\)](#) differs from these systems by offering a hardware-software stack for agile vision-based quadrotor flight, with an emphasis on tight integration of the perception-action loop. Compared with systems such as the MRS UAV System and Aerostack, it follows a performance-first philosophy, resulting in a tightly coupled but necessarily less modular solution. The `kr_autonomous_flight` stack [Mohta et al. \(2018\)](#) also provides a complete autonomy stack for GNSS-denied aerial

robot missions, integrating vision-based odometry, LiDAR-based SLAM, global planning for target reaching, trajectory generation, while also supporting downstream tasks such as semantic SLAM. Beyond aerial robotics, Nav2 [Macenski et al. \(2020\)](#) provides a navigation framework for ground robots in predominantly indoor environments. Built around behavior trees, it includes LiDAR-based SLAM, global and local planning, and control, offering a ROS2-compatible navigation stack for ground robots.

Targeting a more unified approach to autonomy, Nebula [NASA CoSTAR \(2022\)](#); [Agha et al. \(2021\)](#) is team CoSTAR’s architecture for their participation in the DARPA Subterranean Challenge. The public release includes components such as the multi-robot SLAM method [Chang et al. \(2022\)](#), while other elements of the perception-action loop and the complete autonomy stack are not open. Beyond autonomy stacks themselves, recent work has also explored how such systems can support higher-level autonomy. For example, [Ravichandran et al. \(2025\)](#) present progress in Large Language Model (LLM)-enabled autonomy in field settings with the LLM orchestrating autonomous operations over several kilometers across aerial and ground systems. This direction aligns with ongoing efforts on Vision-Language-Action (VLA) models for autonomy [Zhang et al. \(2026\)](#); [Serpiva et al. \(2025\)](#); [Xu et al. \(2026\)](#); [Wu et al. \(2025\)](#), building on core modules such as works in SLAM and control.

Table 1 summarizes how various autonomy stacks compare in terms of functionalities and features. Specifically, we compare across four aspects: (a) supported sensing modalities and multi-layered safety mechanisms; (b) breadth of capabilities, including supported mission objectives; (c) design modularity and support for different robot embodiments; and (d) open-source availability and field evaluation.

Compared with existing works, the UAstack presents distinct contributions. First, it represents a functionality-rich autonomy stack experimentally validated on heterogeneous platforms, including multirotors and legged robots. It provides complete implementations of all the core modules (in perception, planning, and navigation) and the overarching architecture for high-performance autonomy. This includes SLAM, VLM-based scene reasoning, motion, and informative path planning, and multi-layered safe navigation and control. Second, the UAstack incorporates design choices aimed at enhanced resilience. Aiming to enable resilient operations in strenuous environments, the UAstack builds upon lessons learned from prior works in field autonomy such as [Tranzatto et al. \(2022\)](#); [Ebadi et al. \(2023\)](#); [Agha et al. \(2021\)](#); [Kottege et al. \(2024\)](#); [Dharmadhikari and Alexis \(2025\)](#) and combines multi-modal sensor fusion (combining the complementary benefits of LiDAR, vision, and radar in order to penetrate through GNSS-denied and perceptually-degraded environments) with multi-layered safety (such that collision-avoidance is assured through three distinct but synergetic methodological pathways). Targeting advanced behaviors, the UAstack supports advanced mission-level behaviors, offering exploration and coverage in complex, large-scale, geometrically complex environments. Finally, the complete implementation of the UAstack is released open-source with supporting datasets and, where applicable, simulation integration, to accelerate testing, verification, adoption, and extension by the community.

### 3 Unified Autonomy

This section presents the architecture and key modules of the unified autonomy stack.

#### 3.1 Autonomy Architecture

The Unified Autonomy Stack is organized around three core modules – perception, planning, and navigation – following the principles of the “sense-think-act” loop, while targeting generalizability across aerial and ground robot configurations, and resilience in demanding environments. Its overall architecture is presented in Figure 2. The UAstack consumes diverse sensor data and outputs low-level commands to standard controllers available in most modern robotic systems, for example, on PX4-based drones [Meier et al. \(2015\)](#) (or any other MAVLink-compatible autopilot [Koubâa et al. \(2019\)](#)) and standard (linear and angular) velocity controllers on ground platforms. Its key features are as follows:

**Generalizability:** The UAstack applies with few adjustments to a wide range of robot configurations, offering a consistent user experience for navigation and informative path planning tasks across platforms. Currently out-of-the-box supporting multirotors and other rotorcrafts, alongside several ground systems and especially legged robots, it provides a strong foundation for research in unified embodied AI. In this paper, we present experimental verification with multirotors and quadrupeds, while the associated open-source repository includes examples with additional morphologies such as ground rovers and helicopters.

**Multi-modality:** The UAstack fuses complementary sensor cues, currently including LiDAR, FMCW radar, vision, and IMU, enabling resilience in perceptually-degraded and GNSS-denied conditions [Chung et al. \(2023\)](#), including settings characterized by self-similar geometries, dark or low-texture scenes, icy regions, and obscurants such as smoke and dust. We emphasize the tight fusion of LiDAR and radar data focusing on their complementary role in numerous perceptually-degraded environments as discussed in the evaluation section.

**Multi-layer Safety:** The UAstack departs from conventional architectures in which safety is ensured by solutions with a single point-of-failure. Most commonly, modern autonomy solutions rely on a cascade of calculations in which collision-free planning takes place only on an online reconstructed map. In practice, it entails that non-trivial localization or mapping errors (e.g., such as those often encountered in perceptually-degraded settings or when encountering thin obstacles) can lead to collisions. The UAstack combines map-based motion planning with deep learning-driven navigation strategies and safety filters that directly consume online exteroceptive depth measurements and, if necessary, adjust the robot’s path to re-assert safety.

**Methodological Plurality:** The UAstack integrates both “conventional” model-based control, estimation, perception, optimization and planning techniques, as well as deep learning-based methods alongside hybrid techniques. Indicative examples include its factor graph-based multi-modal SLAM and its navigation policies offering options for Deep Reinforcement Learning (DRL)-based and Neural Model Predictive Control (NMPC).

Subsequently, we outline the key modules of the UAstack and point to prior works as applicable. Furthermore, we discuss the interfaces considered and how UAstack can be extended to new robot configurations. Importantly, all autonomy modules described hereafter operate subject to the information provided to the stack’s Robot Abstraction Layer and the Mission Abstraction Layer.

**Robot Abstraction Layer:** This layer defines the robot type (e.g., multirotor, quadruped, etc.) and its key motion parameters, alongside its sensor suite  $\mathcal{S}$  including the sensor types (e.g., LiDAR, Radar, cameras, IMU) and their configurations (e.g., fields of view, effective ranges, calibration constants). Based on this layer, the modules of the UAstack determine the robot motion constraints  $\mu_R$  to be applied (e.g., robot size, potentially applicable traversability constraints, kinematic constraints), the sensor data to be fused, sensor intrinsic and extrinsic calibration parameters, time-synchronization information between the sensors, as well as the command interface to be used (e.g., acceleration commands for multirotors, velocity commands to a quadruped legged robot) as detailed in Section 3.5. It also sets if certain modules of the UAstack are enabled such as if multi-layered safety will be employed and if yes, which submodules of it will be engaged.

**Mission Abstraction Layer:** This layer sets the task for the robot, including if this relates to reaching a target, exploring an unknown area, inspecting a previously explored region, any combination among those, or any

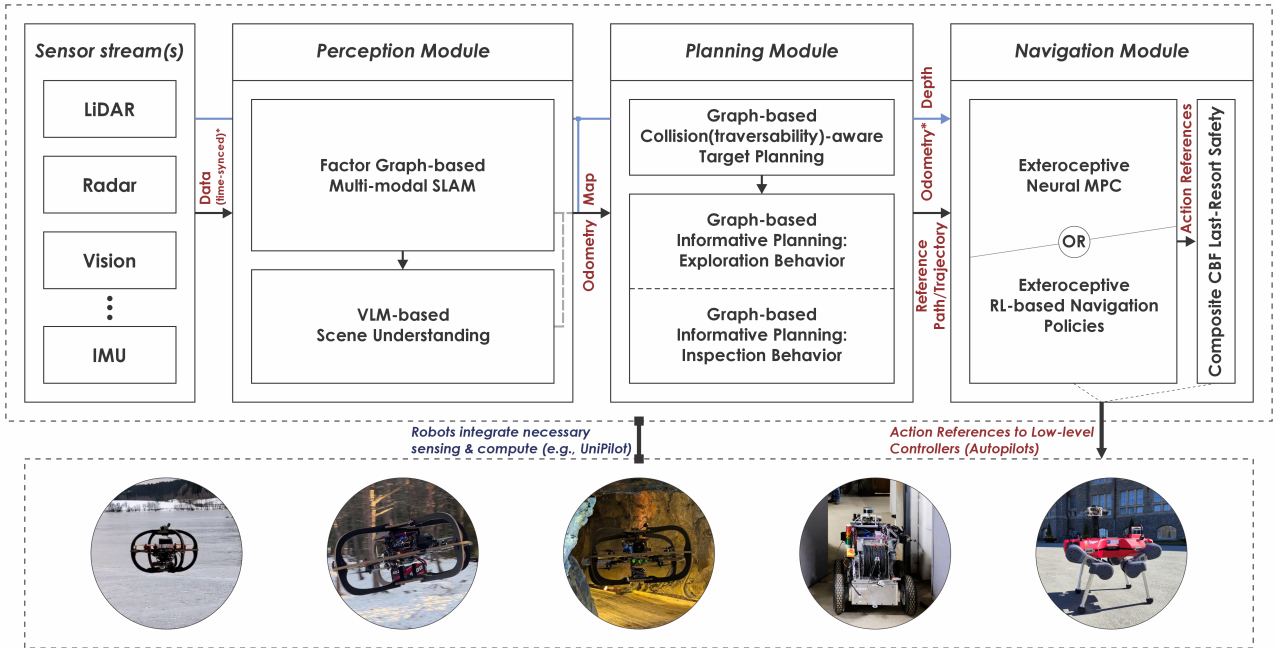


**Figure 2.** The architecture of the UAstack. The stack involves three core modules, on perception, planning, and navigation that operate in a synergistic fashion. Aiming for operational resilience in diverse GNSS-denied, perceptually-degraded environments the UAstack emphasizes multi-modal sensor fusion merging data from LiDAR, radar, and camera sensing, alongside IMU cues. VLM-based reasoning builds upon the geometric reconstruction and supports object discovery and visual question/answering. The stack’s planning layer offers diverse behaviors, with ready-made implementations for target-reach, unknown area exploration and inspection, across robot morphologies. Even though map-based collision avoidance and traversability analysis are provided within the planning module, the stack’s navigation module further offers a multi-layered approach to safety involving deep exteroceptive navigation strategies, either through neural model predictive control or reinforcement learning, alongside formal last-resort safety based on control barrier functions. In terms of morphologies, the UAstack currently supports aerial and ground robots, especially rotorcrafts (e.g., multirotors), legged robots and ground rovers. Experimental validation has taken place on different multirotor systems and quadruped legged robots, while simulation examples in the released code include additional morphologies such as ground rovers and helicopters.

other behavior built beyond the existing capabilities of the UAstack. It accordingly defines the objective of the planning module. It also sets if certain modules are active such as the VLM-based scene reasoning.

### 3.2 Perception Module

The perception module includes our solution for multi-modal SLAM, alongside integration with a VLM-based reasoning step.

**3.2.1 Multi-Modal SLAM** The proposed novel multi-modal SLAM system (dubbed MIMOSA-X, where ‘X’ denotes the modalities used) uses a factor graph estimator to fuse LiDAR, radar, camera, and IMU measurements using a windowed smoother Dellaert and GTSAM Contributors (2022) for computational efficiency. This architecture, as shown in Figure 2, builds upon ideas proposed in Khedekar et al. (2022); Nissov et al. (2024b), with improvements drawn from further developments in Khedekar and Alexis (2025); Nissov et al. (2024a) for enhanced LiDAR and radar integration, alongside vision integration. Unlike loosely coupled approaches Khedekar et al. (2022); Khattak et al. (2020); Shan et al. (2020), MIMOSA-X fuses LiDAR registration factors, radar Doppler factors, and preintegrated IMU factors in a tightly-coupled manner to avoid degenerate optimizations returning partially observable results. Vision is further optionally fused through between factors.

The estimator considers a state space comprised of the position  $p_{WB}^W$ , velocity  $v_{WB}^W$ , and attitude  $R_B^W$  of the body IMU frame  $\{B\}$  with respect to an inertial (map) frame  $\{W\}$ . Note that  $\{W\}$  is not perfectly gravity aligned, i.e., gravity in  $\{W\}$  does not point exactly down. Furthermore, calibration states such as the accelerometer  $b_a$  and gyroscope  $b_g$  biases and gravity direction  $g^W$  in the map frame are also included. The online gravity estimation has been shown to improve performance Nemiroff et al. (2023), as initial uncertainty regarding the platform attitude can result in map-errors which compound over large distances. The state space  $x$  is thus decomposed into local  $x_L$  and global  $x_G$  states such that

$$x = \underbrace{\begin{pmatrix} p_{WB}^W & v_{WB}^W & R_B^W & b_a & b_g \end{pmatrix}}_{x_L} \underbrace{\begin{pmatrix} g^W \end{pmatrix}}_{x_G}. \quad (1)$$

By concatenating the states from times  $t_{k-l}$  to  $t_k$ , the windowed set of states  $\mathcal{X}_{k-l:k}$  is defined as

$$\mathcal{X}_{k-l:k} = \{x_{L,k-l} \quad x_{L,k-l+1} \quad \dots \quad x_{L,k} \quad x_G\}. \quad (2)$$

The states over this temporal window of size  $l+1$  are thus estimated by the iSAM2 Kaess et al. (2011) nonlinear optimizer, where the optimal estimate  $\mathcal{X}_{k-l:k}^*$  is found by minimizing the covariance-weighted ( $\Sigma_*$ ) sum of the residuals  $e_*$  derived from the IMU, LiDAR, radar, and vision sensor measurements included in the temporal window,

denoted by  $\mathcal{I}$ ,  $\mathcal{L}$ ,  $\mathcal{R}$ , and  $\mathcal{V}$ , respectively. This minimization problem can thus be written as follows

$$\begin{aligned} \mathcal{X}_{k-l:k}^* = \arg \min_{\mathcal{X}_{k-l:k}} & \left[ \|e_0\|_{\Sigma_0}^2 + \sum_{i \in \mathcal{F}_{k-l:k}^{\mathcal{I}}} \|e_{\mathcal{I}_i}\|_{\Sigma_{\mathcal{I}_i}}^2 \right. \\ & + \sum_{i \in \mathcal{F}_{k-l:k}^{\mathcal{L}}} \|e_{\mathcal{L}_i}\|_{\Sigma_{\mathcal{L}_i}}^2 + \sum_{i \in \mathcal{F}_{k-l:k}^{\mathcal{R}}} \|e_{\mathcal{R}_i}\|_{\Sigma_{\mathcal{R}_i}}^2 \\ & \left. + \sum_{i \in \mathcal{F}_{k-l:k}^{\mathcal{V}}} \|e_{\mathcal{V}_i}\|_{\Sigma_{\mathcal{V}_i}}^2 \right], \end{aligned} \quad (3)$$

for the marginalization prior  $e_0$ ,  $\Sigma_0$ , and the IMU, LiDAR, radar, and vision factors  $\mathcal{F}_{k-l:k}^*$  in the window time frame, denoted with the same notation as the residuals and covariance matrices. For each IMU measurement, a prediction is made from the current graph state, resulting in a high-rate odometry output. Upon receiving a new exteroceptive sensor measurement, the graph is updated with the relevant factors, and the optimal state estimate is calculated, alongside maps updated if the measurement was a LiDAR measurement.

It is not required that all sensors operate at the same frequency, nor that their measurements arrive chronologically by their timestamps. The method does, however, assume that the timestamps of the input measurements are accurate, i.e., some effort from the implementer has been taken to ensure the accuracy of the timestamping of the sensor data in the form of hardware or software-based time synchronization, such that all timestamps are on a common time axis. A representative factor graph constructed by the multi-modal estimator is shown in Figure 3. We first give an overarching view of the operation of the system and later detail how each of the sensor measurements is used.

**Initialization** The method assumes the system is stationary at startup. During this period, IMU measurements are accumulated over a 1 s window and averaged, yielding the mean accelerometer reading  $\mu_a$  and mean gyroscope reading  $\mu_g$ . Since the system is at rest, the gyroscope mean is a direct estimate of the gyroscope bias, so we set  $b_{g,0} = \mu_g$ . The accelerometer mean satisfies  $\mu_a = b_{a,0} + (R_{B,0}^w)^\top g_w$ , under the assumption that  $b_{a,0}$  is constant over the initialization window and that measurement noise is negligible. Because the accelerometer bias is not yet known, we approximate  $R_{B,0}^w$  by aligning  $\mu_a$  with the gravity direction  $[0 \ 0 \ 1]^\top$ , which determines the roll and pitch components. The yaw component is unobservable from accelerometry alone and is set to zero. This approximation introduces an attitude error proportional to the magnitude of  $b_{a,0}$ ; for instance, a bias of  $1 \text{ m/s}^2$  yields an initial attitude error of approximately  $5^\circ$ , following Farrell (2008). The gravity direction  $g_w$  is estimated, instead of being fixed, to account for this error. The initial position  $p_{WB,0}^w$  and velocity  $v_{WB,0}^w$  are both set to zero.

Initialization is triggered upon arrival of the first exteroceptive sensor measurement, provided the IMU buffer spans at least 1 s. In the case of LiDAR, this step additionally initializes the global map, as described in the following section.

**Propagation** Upon receiving a new measurement from the IMU, the measurement is added to a buffer for future use in the main thread. In a separate thread, this measurement is used to propagate the latest state in the graph, which is then published to provide high-rate odometry for feedback control.

Upon receiving a new measurement from an exteroceptive sensor, typically, the method (a) creates a new state at the timestamp derived from the measurement, (b) connects the new state with the remaining graph with a preintegrated IMU factor derived from the IMU buffer, (c) adds a factor derived from the measurement, (d) optimizes the graph, and (e) publishes the new state. However, depending upon the actual sensor stream and system, the method may deviate slightly from this. We now detail these deviations. If the timestamp of the incoming measurement is older than the lag window, it is discarded prioritizing low-latency data. If the timestamp of the new measurement is very close (i.e., there are no IMU measurements in between) to the timestamp of any of the states in the window, then we treat the measurement as having the same timestamp as that state, i.e., we do not create a new state and use the matched state for adding a measurement-derived factor. This has the added advantage that late measurements arriving to the graph out-of-order can seamlessly be integrated, assuming they are within the smoother window. If the timestamp is older than the newest state in the window (i.e., it arrived with high latency), then we identify the correct location that it should have been added as well as the preintegrated IMU factor that currently connects the states straddling this timestamp. The preintegrated IMU factor is then replaced by a new state at the new timestamp, along with the measurement-derived factor and two new preintegrated IMU factors.

The next paragraphs detail the specifics on the handling of each sensor modality. Note, some factor residuals are constructed on a per-point basis, e.g., in the case of the LiDAR and radar factors. For computational savings, these are implemented as a single Hessian factor by summing individual contributions. For brevity, the factor residuals will be defined on a per-point basis, and the summation implied.

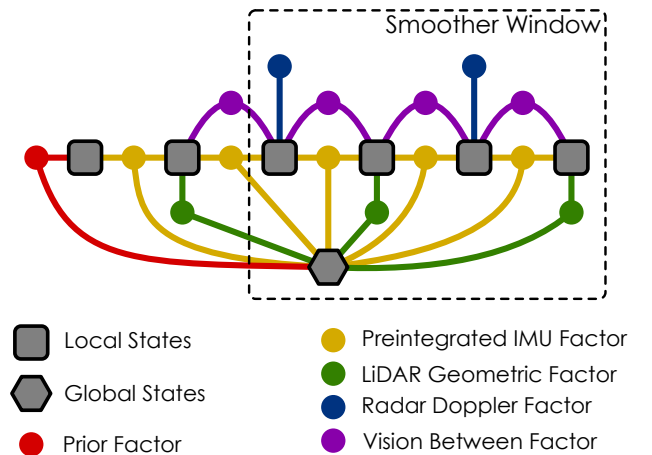


**Figure 3.** Representative exemplary factor graph constructed by the multi-modal estimator.

**Inertial Measurement Unit** IMU measurements are stored in a buffer on arrival, for easy use upon receiving

measurements from one of the aiding sensors. At that point, the corresponding exteroceptive factors are created and connected to the graph by an IMU preintegration factor, following Forster et al. (2017), with the following residuals that preintegrate the measurements between times  $i$  and  $j$

$$e_{\mathcal{I}} = [e_{\mathcal{I},\mathbf{R}}^{\top} \quad e_{\mathcal{I},\mathbf{p}}^{\top} \quad e_{\mathcal{I},\mathbf{v}}^{\top}]^{\top}, \quad (4)$$

including attitude  $e_{\mathcal{I},\mathbf{R}}$ , position  $e_{\mathcal{I},\mathbf{p}}$ , and velocity  $e_{\mathcal{I},\mathbf{v}}$  error terms. The reader is referred to Forster et al. (2017); Dellaert and GTSAM Contributors (2022) for a detailed description of each term.

**LiDAR** The point cloud measurement obtained from a LiDAR typically contains several thousand points that were sampled at various instants between  $[t, t + t_s]$  where  $t$  is the timestamp of the measurement and  $t_s$  is the duration of the sweep. Since the LiDAR is likely to have moved during this time, it is necessary to deskew the point cloud to account for this motion. As the IMU measurements for this duration are available, we use them to propagate the latest state in the graph up to  $t + t_s$ , storing the intermediate pose  $\tilde{\mathbf{T}}_{\mathbf{B},t+t_s}^{\mathbf{W}}$  for every unique timestamp  $t + t_k$  in the point cloud. Using these intermediate poses, we iterate over the points  $\mathbf{r}^{\mathbf{L},t+t_k}$  at each unique timestamp and transform them to the body frame at the timestamp of the last point  $t + t_s$  as given by

$$\mathbf{r}^{\mathbf{B},t+t_s} = \tilde{\mathbf{T}}_{\mathbf{W}}^{\mathbf{B},t+t_s} \tilde{\mathbf{T}}_{\mathbf{B},t+t_s}^{\mathbf{W}} \mathbf{T}_{\mathbf{L}}^{\mathbf{B}} \circ \mathbf{r}^{\mathbf{L},t+t_k}, \quad (5)$$

where  $\circ$  denotes the homogeneous transformation action on a vector in  $\mathbb{R}^3$ .

For further processing, assuming that the IMU propagation was correct, the point cloud is considered to have been sampled instantaneously at  $t + t_s$ . Afterwards, the point cloud is downsampled, for computational efficiency, first by removing three out of four points, and second by organizing the point cloud into a voxel grid and subsampling, ensuring a maximum of  $n_p$  points per voxel and a minimum distance of  $\eta_p$  between any two points in a voxel. Afterwards, the correspondences are found by relating points in the current cloud with planes fit in the map; these correspondences are added to the graph in the form of point-to-plane residuals. This per-point residual  $\epsilon_{\mathcal{L}}$  is calculated as follows

$$\epsilon_{\mathcal{L}} = \mathbf{n}^{\mathbf{W}} \cdot (\mathbf{R}_{\mathbf{B}}^{\mathbf{W}} \tilde{\mathbf{r}}_{\mathcal{L}}^{\mathbf{B}} + \mathbf{p}_{\mathbf{WB}}^{\mathbf{W}} - \mathbf{r}_0^{\mathbf{W}}), \quad (6)$$

for a plane defined by the normal  $\mathbf{n}^{\mathbf{W}}$  and point  $\mathbf{r}_0^{\mathbf{W}}$  and the corresponding transformed point  $\tilde{\mathbf{r}}_{\mathcal{L}}^{\mathbf{B}}$  from the downsampled LiDAR point cloud. The per-point residuals are whitened using the point noise covariance  $\sigma_{\epsilon_{\mathcal{L}}}^2$  and assembled into a single dense hessian factor. For outlier rejection, these residuals are augmented with Huber M-estimators Huber (1964). Post-optimization, the pose is compared with previous key frames, and if a significant difference in position or attitude is detected, a new key frame is created, and the current point cloud is added to maintain a monolithic map.

**Radar** In the context of this method, FMCW radars are assumed to return point cloud measurements, where each point is defined by its 3D position  $\mathbf{r}_{\mathcal{R}}$  and radial speed  $v_r$ . Unlike the estimator proposed in Nissov et al. (2024b), here the RANdom SAMple Consensus (RANSAC) least-squares calculation of linear velocity from the radar point

cloud is omitted. Instead, the individual points from the radar point cloud are integrated into the graph. By directly integrating the radial speed measurements, we avoid the potential limitations associated with first estimating linear velocity independently. Namely, these are the minimum number and diversity of points required for fully resolving the 3 axes of linear velocity. Even with sufficient points, low point cloud sizes can still result in poor estimation of either the velocity or the covariance matrix, leading to degraded performance.

Thus, the per-point residual  $\epsilon_{\mathcal{R}}$  for the radar Doppler factor is

$$\epsilon_{\mathcal{R}} = -\hat{\mathbf{v}}_{\mathbf{WR}}^{\mathbf{R}} \cdot \frac{\tilde{\mathbf{r}}_{\mathcal{R}}}{\|\tilde{\mathbf{r}}_{\mathcal{R}}\|} - \tilde{v}_r, \quad (7)$$

where  $\hat{\mathbf{v}}_{\mathbf{WR}}^{\mathbf{R}}$  is the radar-frame velocity estimate and  $\tilde{\mathbf{r}}$ ,  $\tilde{v}_r$  are the radar point position and radial speed measurements. The radar-frame velocity is composed from the state estimates as

$$\hat{\mathbf{v}}_{\mathbf{WR}}^{\mathbf{R}} = \mathbf{R}_{\mathbf{B}}^{\mathbf{R}} \left( (\hat{\mathbf{R}}_{\mathbf{B}}^{\mathbf{W}})^{\top} \hat{\mathbf{v}}_{\mathbf{WB}}^{\mathbf{W}} + (\hat{\boldsymbol{\omega}}_{\mathbf{WB}}^{\mathbf{B}} \times \mathbf{p}_{\mathbf{BR}}^{\mathbf{B}}) \right), \quad (8)$$

assuming the extrinsic translation  $\mathbf{p}_{\mathbf{BR}}^{\mathbf{B}}$  and rotation  $\mathbf{R}_{\mathbf{B}}^{\mathbf{R}}$  between  $\{\mathbf{B}\}$  and  $\{\mathbf{R}\}$  is known a priori, and that the angular rate during a given radar chirp period  $\hat{\boldsymbol{\omega}}_{\mathbf{WB}}^{\mathbf{B}}$  can be accurately estimated by averaging the IMU gyroscope measurements. As the radar sensor is known to generate spurious points Harlow et al. (2024), the residual is augmented with a Cauchy M-estimator for outlier rejection. This has the added benefit of improved resilience against dynamic objects by suppressing the influence of such outliers. The choice of Cauchy is motivated by the desire for an M-estimator that more rapidly nullifies the impact of significantly large outliers.

**Vision** Vision factors are added in a loosely-coupled manner, taking advantage of the wealth of capable estimators that exist in the vision community. Specifically, a visual-inertial estimator based on Bloesch et al. (2017) processes the camera and IMU measurements, creating odometry estimates as a result. The pose estimates  $\hat{\mathbf{T}}_{\mathbf{B}}^{\mathbf{W}}$  from this external method are stored in a buffer. This information is incorporated, if it passes a D-Optimality pose quality check Carrillo et al. (2012), into the factor graph with a relative transform factor, which compares the relative transform between pose estimates  $\hat{\mathbf{T}}_{\mathbf{B}}^{\mathbf{W}}$  and the aforementioned measurements across the same time interval. Assuming vision pose measurements are available for times  $t_i$  and  $t_j$ , the factor residual can be calculated as

$$e_{\mathcal{V}} = \text{Log} \left( \left( (\hat{\mathbf{T}}_{\mathbf{B},i}^{\mathbf{W}})^{-1} \tilde{\mathbf{T}}_{\mathbf{B},j}^{\mathbf{W}} \right)^{-1} \left( (\hat{\mathbf{T}}_{\mathbf{B},i}^{\mathbf{W}})^{-1} \hat{\mathbf{T}}_{\mathbf{B},j}^{\mathbf{W}} \right) \right), \quad (9)$$

where Log denotes the logarithmic map from the  $SE(3)$  manifold to its Lie algebra  $\mathfrak{se}(3)$ . This approach draws inspiration from Khattak et al. (2020); Khedekar et al. (2022).

**3.2.2 Vision-Language Reasoning** Our semantic reasoning system integrates two complementary vision-language model (VLM) capabilities: (i) open-vocabulary object perception with semantic 3D mapping, and (ii) binary visual

question-answering (Yes/No) for high-level scene reasoning. Together, these capabilities collectively enable semantic scene understanding and contextual judgment and decision making from online visual data. The VLM-based functionality is illustrated in Figure 4. Even though our implementation employs YOLOe Wang et al. (2025) and GPT-5, the proposed semantic reasoning system is designed to be compatible with other open-source and proprietary VLMs that support open-vocabulary object detection and visual question-answering tasks.

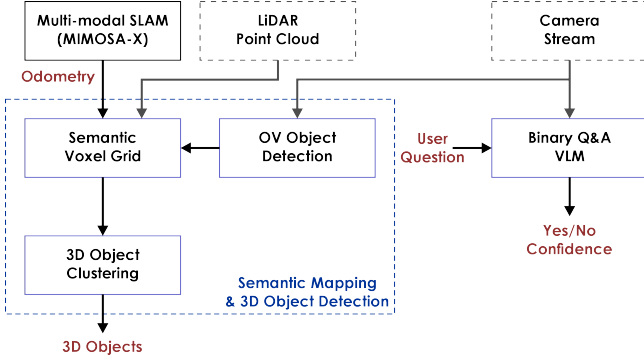


**Figure 4.** Illustration of the current VLM-based functionality of the UAstack for semantic scene mapping and visual Q&A.

*Open-Vocabulary Object Detection and Semantic 3D Mapping* 3D object detection is formulated as a semantic mapping problem. Objects are detected on the camera image using an open-vocabulary detector (YOLOe) or a VLM-based detector (GPT-5) initialized with a set of labels. These models produce labeled 2D bounding boxes and associated detection confidences. In parallel, a 3D voxel grid is maintained using LiDAR measurements and pose estimates from our SLAM solution.

To integrate semantic detections into the 3D representation, voxel grid points are projected into the camera frame using the camera extrinsics and the current odometry estimate. For each 2D detection, the subset of projected points that fall within the corresponding bounding box is extracted and clustered to remove outliers. The resulting points are used to update the voxels’ semantic values via Bayesian fusion, which uses the object detector’s confidences.

Finally, Euclidean clustering is performed for each semantic class present in the voxel grid to extract 3D object instances. These objects are represented as 3D bounding boxes, enabling semantic and spatial reasoning.

*Binary Visual Question-Answering* For high-level semantic assessment, a VLM (GPT-5) processes the front-camera image together with a binary “Yes/No” question. These visual question-answering tasks typically focus on safety- or navigation-related properties of the scene (e.g., “is an object blocking a door?”), which can be challenging to infer from geometric information alone. The model produces a binary answer, alongside its response confidence (ranging from 0 to 1) and a brief explanation of its reasoning.

### 3.3 Planning Module

The planning module in the UAstack is facilitated through OmniPlanner Zacharia et al. (2026), a graph-based planner designed to work across diverse aerial, ground, and

#### Algorithm 1 planning module

```

1:  $\mu_R \leftarrow \text{GetRobotConstraints}()$  ▷ Robot
   Abstraction Layer
2:  $\{\mathcal{D}, \mathcal{C}\} \leftarrow \text{GetSensorParams}()$  ▷ Robot
   Abstraction Layer
3:  $\mathcal{J} \leftarrow \text{GetMissionObjective}()$  ▷ Mission
   Abstraction Layer
4: repeat
5:    $\mathbb{G}_L \leftarrow \text{BuildLocalGraph}(\mu_R, \mathcal{M}, \mathcal{H})$  ▷ Planning
   Kernel
6:    $\mathbb{G}_G \leftarrow \text{UpdateGlobalGraph}(\mu_R, \mathbb{G}_L)$  ▷ Planning
   Kernel
7:   if  $\mathcal{J} = \mathcal{J}_{TP}$  then
8:     PlaningToTarget $(\mu_R, p_t, \mathcal{D}, \mathbb{G}_L, \mathbb{G}_G)$ 
9:   else if  $\mathcal{J} = \mathcal{J}_{EP}$  then
10:    ExplorationPlanning $(\mu_R, \mathcal{D}, \mathbb{G}_L, \mathbb{G}_G, \mathcal{M})$ 
11:  else if  $\mathcal{J} = \mathcal{J}_{IP}$  then
12:    InspectionPlanning $(\mu_R, \mathcal{D}, \mathcal{C}, \mathbb{G}_L, \mathcal{M})$ 
13:  end if
14: until Robot Endurance Critical
15: ReturnToHome $(\mathbb{G}_L, \mathbb{G}_G, \mu_R)$  ▷ Planning Kernel

```

underwater robot morphologies. The planner is currently applicable to systems for which graph-based planning is a viable option (e.g., various thrust-controlled aerial and underwater systems such as multirotors and ROVs, legged robots, and differential drive ground rovers). At the core, the planner utilizes a unified planning kernel that is agnostic to robot morphology, environment type, and mission objective and provides both target navigation as well as informative planning behaviors, such as exploration and inspection, based on the task objective  $\mathcal{J}$  ( $\mathcal{J}_{TP}$ : Planning to a target,  $\mathcal{J}_{EP}$ : Exploration Planning,  $\mathcal{J}_{IP}$ : Inspection Planning) set by the Mission Abstraction Layer. Algorithm 1 gives a high-level overview of the planning module, while Figure 5 illustrates the different parts of the module and their interactions. The reader is referred to Zacharia et al. (2026) for the algorithmic details regarding this module.

*3.3.1 Planning Kernel* The Planning Kernel of OmniPlanner serves as the backbone of the methodology, providing the data structures and functions for searching the robot’s admissible configuration space to enable the desired behaviors. All operations take place on a dual environment representation consisting of a) a Volumetric Map  $\mathcal{M}$  (in this work Voxblox Oleynikova et al. (2017)), with voxel size  $v_m$ , and, when applicable, b) an elevation map  $\mathcal{H}$  for ground robots (utilizing the work from Fankhauser et al. (2018, 2014)), with grid size  $v_h$ . The kernel employs a bifurcated local/global planning architecture. The *Local Planning Submodule* operates in a local volume  $\mathbf{b}_L$  and constructs a bounded, sampling-based, dense graph  $\mathbb{G}_L$ , with its vertex and edge sets  $\mathcal{V}_L, \mathcal{E}_L$  inside  $\mathbf{b}_L$  spanning the locally reachable configuration space. All vertices and edges are sampled such that they lie entirely in collision-free space and respect the robot motion constraints  $\mu_R$  defined by the Robot Abstraction Layer (e.g., traversability, robot size  $\mathbf{b}_R$ , etc.). The graph  $\mathbb{G}_L$  is used by the planning module for local information gathering and collision-free navigation as described in the subsequent subsections. The

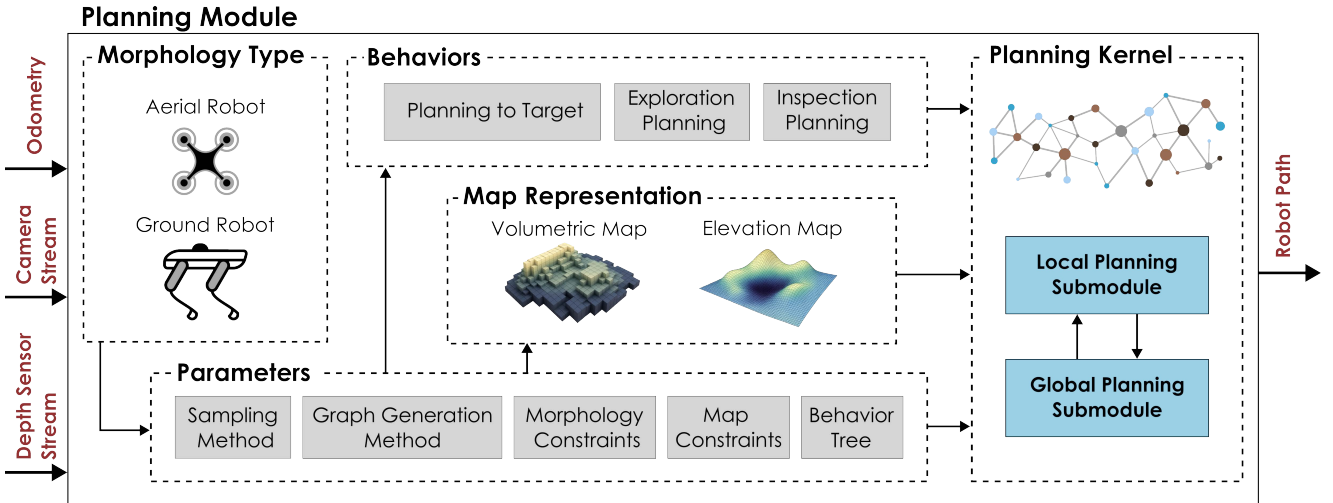


**Figure 5.** Planning module architecture. The planning module is facilitated through OmniPlanner designed to work universally across aerial, ground, and underwater robot morphologies. At the core, the planner integrates a domain- and morphology-agnostic planning kernel that utilizes the dual map representation to build local and global graphs, both satisfying the robot motion constraints set by the Robot Abstraction Layer. The local graph is used for local information gathering and collision-free navigation, whereas the global graph is used for fast but coarse planning in the entire known space. Utilizing these, the appropriate behavior (Exploration, Inspection, Planning to Target) is executed as per the task set by Mission Abstraction Layer.

*Global Planning Submodule* maintains a sparse global graph  $\mathbb{G}_G = \{\mathcal{V}_G, \mathcal{E}_G\}$  built by aggregating the sparsified local planning graphs across the mission. This graph is used to represent the entire known space, providing fast global planning functionality. As  $\mathbb{G}_G$  is built from  $\mathbb{G}_L$ , all vertices and edges in  $\mathcal{V}_G, \mathcal{E}_G$  are in free space and satisfy the robot motion constraints. The Global Planning Submodule also keeps track of the robot's remaining endurance (or otherwise-defined remaining mission time). At each planning iteration, the Planning Kernel checks if the remaining time is sufficient to execute the path given by the specific behavior and return to the start location. If yes, that path is executed, else, the Kernel triggers a homing maneuver to guide the robot back to the starting location.

**3.3.2 Planning to a Target** *UStack* facilitates planning to a desired waypoint  $\mathbf{p}_t$  both within the already explored space, as well as in the unknown, as long as this is iteratively found to be possible. In each planning iteration, first, a guiding path  $\sigma_t$  is calculated. If  $\mathbf{p}_t$  lies in the known (explored) space,  $\sigma_t$  is simply calculated as the shortest path along  $\mathbb{G}_G$  to the vertex in  $\mathcal{V}_G$  closest to  $\mathbf{p}_t$ . Otherwise,  $\sigma_t$  is calculated as the path towards the vertex that is on the frontier of the explored space and is closest to  $\mathbf{p}_t$ . Next,  $\mathbb{G}_L$  is used to calculate a local path  $\sigma_{TP}$  guiding the robot along  $\sigma_t$  which is then commanded to the subsequent modules to track. When the robot reaches within a distance  $d_{path}$  from the last point in  $\sigma_{TP}$ , the next iteration of the planner is triggered. This entire process is repeated until the robot reaches  $\mathbf{p}_t$  or no progress can be made towards it, at which point the planner declares that the waypoint is unreachable. It is highlighted that the homing maneuver mentioned in Section 3.3.1 uses the Planning to Target behavior with the starting location as  $\mathbf{p}_t$ .

**3.3.3 Exploration Planning** The first informative planning behavior supported by OmniPlanner is the Volumetric Exploration (VE), where the robot is tasked to iteratively uncover the unknown volume using an Field of View (FoV)-

and range-constrained depth sensor  $\mathcal{D}$  (whose parameters are given by the Robot Abstraction Layer). In each planning iteration,  $\mathbb{G}_L$  is used to find the path that leads to uncovering the largest amount of unknown space. First, shortest paths from the current robot location to each vertex in  $\mathcal{V}_L$  are calculated. An information gain, called Volume Gain, related to the amount of unknown volume mapped by  $\mathcal{D}$  from a robot configuration, is calculated for each vertex in  $\mathcal{V}_L$ . The path  $\sigma_{EP}$  with the highest aggregated Volume Gain is selected as the next exploration path. When the robot reaches within a distance  $d_{path}$  from the last point in  $\sigma_{EP}$ , the next iteration of the planner is triggered and the process is repeated. When no informative path is found in  $\mathbb{G}_L$ , the  $\mathbb{G}_G$  is utilized to reposition the robot to a frontier of the explored space. The planner tracks vertices in  $\mathbb{G}_G$  having high Volume Gain (called frontier vertices), and repositions the robot to the frontier vertex having the highest gain using the Planning to Target behavior described in Section 3.3.2. Upon reaching the frontier, local exploration continues.

**3.3.4 Inspection Planning** In the Visual Inspection (VI) behavior, the planner is tasked to inspect a subset of the occupied surface in the mapped volume using an FoV- and range-constrained camera sensor  $\mathcal{C}$  (whose parameters are given by the Robot Abstraction Layer) at the desired viewing distance  $d_{view}$  (given by the Mission Abstraction Layer). A set  $\mathbb{V}$  of viewpoints, at a distance  $d_{view}$  from the occupied surface, is built. A graph  $\mathbb{G}_{VI}$  is built using the Local Planning Submodule to connect the viewpoints in  $\mathbb{V}$ . The minimal viewpoint set  $\mathbb{V}_{best}$  viewing the entire surface is selected, and the order to visit them is calculated by solving the Traveling Salesman Problem (TSP) problem. The shortest paths along  $\mathbb{G}_{VI}$  connecting the subsequent viewpoint in the tour are concatenated to form the inspection path.

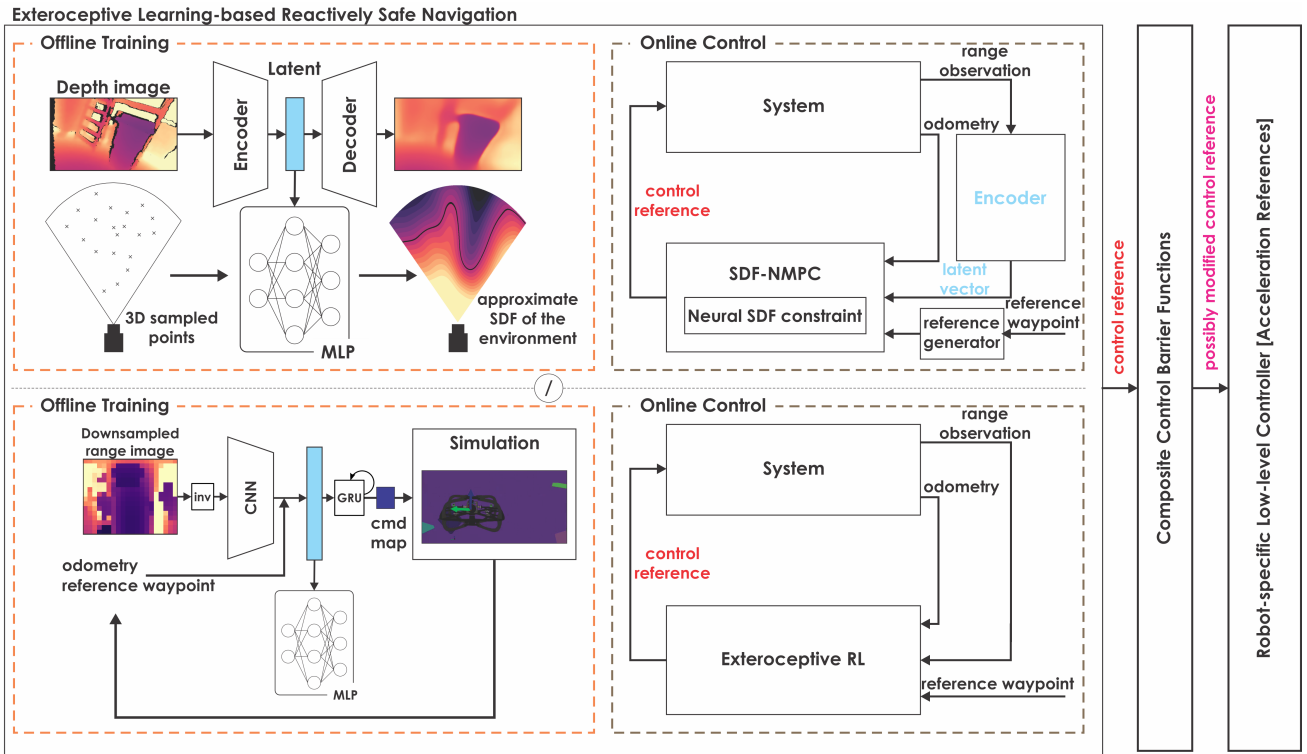


**Figure 6.** Navigation module architecture. Two swappable local navigation modalities are offered: (top) SDF-NMPC, which encodes depth images into a latent SDF representation online and embeds it as a constraint in an NMPC controller; and (bottom) ExRL, which combines inverted range images with proprioceptive state through a policy trained using PPO in simulation to directly output acceleration commands for waypoint-directed collision-free navigation. In both cases, the resulting acceleration control reference is passed through the C-CBF safety filter, which composes range measurements into a composite barrier function to reactively modify the reference acceleration and guarantee collision-free operation as a last resort, before forwarding to the robot-specific low-level controller.

### 3.4 Navigation Module

The UAstack takes a multi-layered approach to safety, illustrated in Figure 6. Conventional modern safe navigation and collision avoidance are based on the planning of paths subject to map constraints, which are then blindly followed by an onboard controller. Despite the major success of this paradigm in many environments and mission profiles, as discussed in Jacquet et al. (2025); Kulkarni and Alexis (2024) and demonstrated in field experience Ebadi et al. (2023) it represents a single point of failure which can lead robots to collisions due to odometry errors or erroneous/incomplete mapping. Although such errors are not common, experience shows that they do manifest and are often catastrophic, at least regarding a robot’s ability to continue its mission. Furthermore, odometry and mapping challenges manifest more frequently in perceptually-degraded and geometrically complex environments Ebadi et al. (2023). While the UAstack does perform map-based avoidance through volumetric mapping for collisions and traversability analysis for ground systems, it further adds two redundant layers of safety: depth sensor-based trajectory tracking and a last-resort safety filtering based on Control Barrier Functions (CBFs). With respect to depth sensor-driven navigation policies, two approaches are offered within the stack, owing to their distinct benefits in certain conditions: (i) a Signed Distance Function (SDF)-based neural NMPC Jacquet et al. (2025) or (ii) a novel DRL-based policy trained for safe navigation and smooth collision avoidance. These methods

enable local deviations from the reference trajectory if and when necessary, to ensure collision avoidance. Both methods provide swappable local navigation policies with distinct performance characteristics that will be discussed in Section 3.4.4. To further assert safety with formal guarantees, a composite CBF-based formulation building upon Harms et al. (2025) is introduced as a last-resort safety filter allowing to modify the control references in the unlikely situation that all other collision-avoidance methods in the stack fail. Importantly, this additional safety layer within the UAstack is currently implemented for obstacle avoidance and not for traversability analysis, predominantly targeting flying robots. This architecture extends upon recent ideas and developments in the research community, such as the perceptive locomotion in Miki et al. (2022), which indeed may also be used as an alternative to the exteroceptive depth navigation strategies discussed below when it comes to quadruped robots.

**3.4.1 Neural SDF-NMPC** Detailed in Jacquet et al. (2025), the SDF-NMPC enables collision-free navigation in unknown environments relying only on depth sensing and (possibly drifting) odometry. In its current implementation, it emphasizes rotorcraft navigation.

The SDF-NMPC represents the visible environment as a Euclidean SDF, defined to be positive in visible free space and negative in occluded regions (i.e., behind obstacles). For efficient computation and to provide a representation compatible with gradient-based NMPC, this SDF is approximated by a neural network, online, from the

latest depth measurement. As a result, the environment is described purely locally, improving robustness to potentially drifting odometry. To keep the representation compatible with a compact neural model, the SDF is saturated beyond a threshold  $T_{\text{SDF}}$ . This SDF is constructed online from the latest depth measurement. As a result, the environment is described purely locally, improving robustness to potentially drifting odometry.

A two-stage neural network is used. First, the input depth image is clamped at a distance  $d_{\text{max}}$ , since only short-range surroundings are relevant for short-horizon collision avoidance. Compression into a low-dimensional latent space  $\mathbf{z}$  is achieved via a convolutional encoder, trained jointly with a decoder to reconstruct the input, ensuring that  $\mathbf{z}$  captures a reliable latent representation of the depth data. Notably, the encoding is biased to place greater emphasis on obstacles close to the robot, encouraging accurate encoding of nearby geometry. The decoder is used only during training, while the encoder provides input to a downstream Multi-Layer Perceptron (MLP) network that reconstructs the SDF.

Specifically, this MLP takes as input the latent vector and a 3D position, and approximates the corresponding SDF value evaluated in that point. The regression task is trained in a supervised manner, including losses that enforce consistency of the SDF gradient. In this way, the trained MLP represents the following parametric function:

$$\begin{aligned} \mathbb{R}^3 &\rightarrow \mathbb{R} \\ \mathbf{p} &\mapsto \text{SDF}_{\theta, \mathbf{z}}(\mathbf{p}), \end{aligned} \quad (10)$$

where  $\theta$  are the neural network weights, and  $\mathbf{z}$  is the latent code corresponding to the depth measurement.

Finally, the neural SDF is embedded into the nonlinear NMPC controller as an explicit position constraint. The following constraint is enforced over the receding horizon:

$$\text{SDF}_{\theta, \mathbf{z}}(\mathbf{p}_S^B) \geq r, \quad (11)$$

where  $r$  is a user-defined threshold accounting for the robot radius and a possible safety margin, and  $\mathbf{p}_S^B$  denotes the position of the robot expressed in the frame  $\{S\}$  in which the depth measurement was captured. Note that additional constraints further ensure that the robot remains within the sensor frustum, i.e., within the region that is currently observable and where the neural SDF is defined. This follows the intuitive principle of “look where you move”, effectively restricting motion to visible free space.

Critically, the method enforces feasibility and stability-type criteria (under fixed sensor observations), with a terminal condition ensuring that the terminal state allows a collision-free braking maneuver to hover. This is assessed by computing the minimum braking distance given the input bounds, and evaluating the SDF at the predicted hovering position. Under this condition, recursive feasibility is ensured, and with a suitable quadratic terminal cost, the optimal value is shown to be non-increasing over time. The NMPC generates acceleration commands from a velocity reference trajectory, since velocity tracking prevents the accumulation of position errors when collision constraints prevent accurate tracking of a nominal trajectory. Accordingly, the interface with the planning module

provides such velocity references derived from planned paths.

**3.4.2 Exteroceptive Deep Reinforcement Learning** The UASTack further offers exteroceptive DRL-based navigation (dubbed ExRL). The proposed novel Exteroceptive DRL (ExRL) approach is formulated as a waypoint navigation problem and considers as input the vector to goal location, the robot orientation, velocity, and angular rates alongside the instantaneous depth image from an exteroceptive sensor (including stereo or RGB-D cameras, Time-of-Flight camera sensors, or LiDARs). We employ end-to-end learning to train a navigation policy to generate commands directly from the robot’s current state and range measurement. The policy is trained using the Aerial Gym Simulator [Kulkarni et al. \(2025b\)](#) to command acceleration and yaw-rate setpoint commands (as commonly provided by most autopilots such as PX4 [Meier et al. \(2015\)](#) and ArduPilot [ArduPilot Dev Team \(2024\)](#)). Relevant open-source examples for training are provided in Aerial Gym, while the policy can be trained on any compatible simulation tool. Similar to the SDF-NMPC, ExRL ensures safe collision-free navigation without a map and thus contributes to multi-layered safety. This work is distinct from prior work of the authors in [Kulkarni et al. \(2023\)](#); [Kulkarni and Alexis \(2023\)](#), by a) departing from a modularized two-step approach and introducing an end-to-end methodology, b) introducing a novel reward function incorporating Time-to-Collision (TTC), and c) commanding acceleration and yaw-rate setpoints instead of velocity references.

**Observations** The observation vector for training the policy consists of both proprioceptive and exteroceptive components. The proprioceptive components are expressed in a yaw-aligned, roll and pitch stabilized coordinate frame  $\{V\}$  sharing the same origin as the robot body IMU frame  $\{B\}$ . Let  $\mathbf{p}^W, \mathbf{p}_*^W \in \mathbb{R}^3$  be the robot and target positions,  $\psi, \psi^*$  be the robot and target yaw respectively, the yaw error be  $\psi_e = ((\psi^* - \psi + \pi) \bmod 2\pi) - \pi$ , and  $\delta^W = \mathbf{p}_*^W - \mathbf{p}^W$  be the position error with  $\delta = \|\delta^W\|$  the vector to the goal. During training, the goal direction  $\delta^V/\delta$ , roll  $\phi$  and pitch  $\theta$  measurements are perturbed by adding noise sampled from a uniform distribution before populating the observation tensor. The linear  $\mathbf{v}_{WB}^B$  and angular velocities  $\boldsymbol{\omega}_{WB}^B$  are not perturbed. The range measurements from the exteroceptive sensor are min-pooled to  $16 \times 20$  pixels and inverted as a 2D inverse range-image  $\mathbf{I}_r$ .

**Table 2.** Observation vector  $\mathbf{o}_t \in \mathbb{R}^{337}$ .

Index	Symbol	Description
0:2	$\delta^V/\delta$	Goal direction in $\{V\}$
3	$\delta$	Distance to goal (m)
4	$\phi$	Roll (rad)
5	$\theta$	Pitch (rad)
6	$\psi_e$	Yaw error (rad)
7:9	$\mathbf{v}_{WB}^B$	Linear velocity in $\{B\}$ (m/s)
10:12	$\boldsymbol{\omega}_{WB}^B$	Angular velocity in $\{B\}$ (rad/s)
13:16	$\mathbf{u}_{t-1}^{acc}$	Previous setpoint (m/s <sup>2</sup> , rad/s)
17:336	$\mathbf{I}_r$	Inverse-range image (m <sup>-1</sup> )

**Actions** The DRL policy outputs a normalized action command  $\mathbf{a}_t = \{a_x, a_y, a_z, a_{\dot{\psi}}\} \in [-1, 1]^4$  that is scaled and mapped to linear acceleration and yaw-rate setpoint commands at time  $t$  as  $\mathbf{u}_t^{acc} = (u_n^x a_x, u_n^y a_y, u_n^z a_z, u_n^{\dot{\psi}} a_{\dot{\psi}})$ , where  $u_n^x, u_n^y, u_n^z, u_n^{\dot{\psi}}$  are tunable scaling parameters, with their values described in Table 6.

**Time-to-Collision (TTC)** We propose the usage of an expected ‘‘time-to-collision’’ metric at each timestep that provides a dense reward signal to the robot. This metric is distinct compared to approaches that directly reward based on raw range data Kulkarni and Alexis (2024), thus prioritizing the relationship between velocity and distance to measured obstacles, only penalizing rapid approaches to obstacles. This metric is calculated only in simulation and is treated as privileged information that is not available to the policy, yet influences the reward signal. For each point  $i$  in the full-resolution point cloud expressed in a sensor frame  $\{S\}$ , the vector from the sensor is calculated as  $\mathbf{r}_i^S$ . The linear component of velocity of the robot along the direction to each point is computed as the projection of  $\mathbf{v}_{WB}^S$  onto the unit direction vector of  $\mathbf{r}_i^S$ . This is subsequently used to calculate the expected time to collision  $\tau_i$  using the distance of the point from the robot:

$$v_i^\perp = \mathbf{v}_{WB}^S \cdot \frac{\mathbf{r}_i^S}{\|\mathbf{r}_i^S\|}, \quad \tau_i = \begin{cases} \|\mathbf{r}_i^S\|/v_i^\perp & v_i^\perp > 0, \\ 10s & v_i^\perp \leq 0. \end{cases} \quad (12)$$

Positive time-to-collision values are clamped between 0s and 10s. Negative values indicate that the robot is moving away from an obstacle, hence they are set to 10s to make their effect negligible. The minimum time-to-collision  $\tau_{min} = \min_i \tau_i$  across all points is considered and used to penalize the robot, emphasizing imminent collisions while largely ignoring well-separated obstacles.

**Policy Architecture** The observation vector  $\mathbf{o}_t$  is partitioned into a proprioceptive and an exteroceptive component, as detailed in Table 2. The latter is treated as a single-channel 2D image and processed by a Convolutional Neural Network (CNN)-based encoder  $f_{CNN}$  with three convolutional blocks. Each block consists of a  $3 \times 3$  convolution with padding of width 1, an Exponential Linear Unit (ELU) activation, and a  $3 \times 3$  max-pooling layer. The resulting feature map is flattened into a 128-dimensional range embedding, which is concatenated with the proprioceptive state vector. This combined representation is then passed through an MLP with hidden layer sizes [256, 128, 64] and ELU activations, followed by a 128-dimensional Gated Recurrent Unit (GRU) layer. The policy is trained using Proximal Policy Optimization (PPO) Schulman et al. (2017) implementation provided by Sample Factory Petrenko et al. (2020). The training time is about 60 min on a consumer grade laptop with an NVIDIA RTX 3080 Ti GPU.

**Environment Setup and Curriculum** Each simulated environment is composed of a rectangular room with dimensions ranging from  $10 \times 10 \times 6$  to  $15 \times 15 \times 10$  m. A simulated robot is initialized on one side of the environment while the goal position is sampled on the opposite side with an arbitrary yaw setpoint. The acceleration and yaw-rate setpoint is

tracked using a controller derived from the work in Lee et al. (2010), whose parameters are randomized at each episode to increase robustness and improve sim2real performance. Within each environment, 25 to 70 cuboidal obstacles of various sizes are sampled. An episode is marked as a *success* if the robot reaches within 1 m of the goal after a predefined number of time steps. If the robot remains collision-free but does not reach the goal, the episode is marked as a *timeout*. Collisions with obstacles are detected by the physics engine, terminate the episode, and are recorded as *crashes*. To encourage stable learning across various environment complexities, a curriculum adjusts the number of obstacles  $n_{obs}$  in each environment. The number is increased or decreased when the average success rate  $\zeta_s$  over 2048 episodes crosses the upper or lower thresholds,  $\zeta_s^+ = 0.70$  and  $\zeta_s^- = 0.60$ , respectively:

$$n_{obs} \leftarrow \begin{cases} \min(n_{obs} + 2, 70) & r_s > \zeta_s^+, \\ \max(n_{obs} - 1, 25) & r_s < \zeta_s^-, \\ n_{obs} & \text{otherwise.} \end{cases} \quad (13)$$

The normalized progress fraction  $\varphi = (n_{obs} - 25)/(70 - 25)$  is calculated and used to scale all non-terminal reward terms by  $K(\varphi) = 1 + 2\varphi \in [1, 3]$ , amplifying training signal as task difficulty increases.

**Reward Function** The reward function is designed to encourage the robot to navigate efficiently to the goal while maintaining safe separation from obstacles and smooth control behavior. It contains three groups of terms: (i) goal-directed terms that reward proximity and velocity alignment toward the goal, (ii) stabilization terms that encourage low velocity, correct heading, and low angular rate when in the vicinity of the goal, and (iii) penalty terms that discourage excessive speed, large control increments, and proximity to obstacles as captured by the TTC metric.

Let the speed  $v = \|\mathbf{v}_{WB}^B\|$ ,  $\mathbf{u}_{t-1}^{acc} \in \mathbb{R}^4$  the previous command;  $\tau_{min} \in [0, 10]$ s the minimum time-to-collision across all rays; and  $\varphi \in [0, 1]$  the curriculum progress fraction. Two kernel functions compose all reward and penalty terms:

$$\mathfrak{R}(\mathbf{m}, \mathbf{a}, \mathbf{v}) = \mathbf{m} \exp(-\mathbf{a}\mathbf{v}^2), \quad (14)$$

$$\mathfrak{F}(\mathbf{m}, \mathbf{a}, \mathbf{v}) = \mathbf{m}(\exp(-\mathbf{a}\mathbf{v}^2) - 1). \quad (15)$$

The following intermediate quantities are defined for compactness and summarized in Table 3, while all reward terms are presented in Table 4.

**Table 3.** Intermediate quantities used in the reward function.

Symbol	Definition	Description
$w(\psi_e)$	$\mathfrak{R}(1, 2, \psi_e)$	Heading gate
$s$	$\mathfrak{R}(2, 2, v - 2)$	Speed-saturation gate
$\xi$	$\mathbf{v}_{WB}^V \cdot \boldsymbol{\delta}^V / (v \cdot \delta)$	Cosine alignment
$w(\delta)$	$1 - \mathfrak{R}(1, 2, \delta)$	$\approx 0$ near, $\approx 1$ far
$\Delta \mathbf{u}$	$\mathbf{u}_t^{acc} - \mathbf{u}_{t-1}^{acc}$	Control increment

The total reward at each timestep takes the form:

**Table 4.** Reward terms.

Term	Formula
$r_{\text{pos}}$	$\mathfrak{R}(3, 1, \delta)$
$r_{\text{prox}}$	$\mathfrak{R}(5, 8, \delta) \cdot w(\psi_e)$
$r_{\text{lin}}$	$(20 - \delta)/20$
$r_{\text{vel}}$	$[\xi s \text{ if } \xi > 0, \text{ else } -0.2] \cdot \min(\delta/3, 1)$
$r_{\text{spd}}$	$\mathfrak{R}(1.5, 10, v) + \mathfrak{R}(1.5, 0.5, v)$
$r_{\text{hdg}}$	$\mathfrak{R}(2, 0.2, \psi_e) + \mathfrak{R}(4, 15, \psi_e)$
$r_{\omega}$	$\mathfrak{R}(1.5, 5, \omega_{\text{WBz}}^B) \cdot w(\psi_e)$
$r_{\text{stab}}$	$(r_{\text{spd}} + r_{\text{hdg}} + r_{\omega}) \cdot \mathbf{1}_{\delta < 1 \text{ m}}$
$P_{\text{spd}}$	$\mathfrak{P}(2, 2, \max(v - 3, 0))$
$P_{+x}$	$\mathfrak{P}(2, 8, \max(\mathbf{v}_{\text{WBx}}^V, 0)) \cdot w(\delta)$
$P_{\Delta \mathbf{u}}$	$\sum_{i \in \{x, y, z, \psi\}} \mathfrak{P}(0.3, 5, \Delta u_n^i)$
$P_{ \mathbf{u} }$	$\mathfrak{P}(0.1, 0.3, u_n^x) + \mathfrak{P}(0.1, 0.3, u_n^y)$ $+ \mathfrak{P}(0.15, 1, u_n^z) + \mathfrak{P}(0.15, 2, u_n^{\psi})$
$P_{\text{ctrl}}$	$P_{\Delta \mathbf{u}} + P_{ \mathbf{u} }$
$P_{\text{TTC}}$	$\mathfrak{R}(-3, 2, \tau_{\text{min}}^2)$

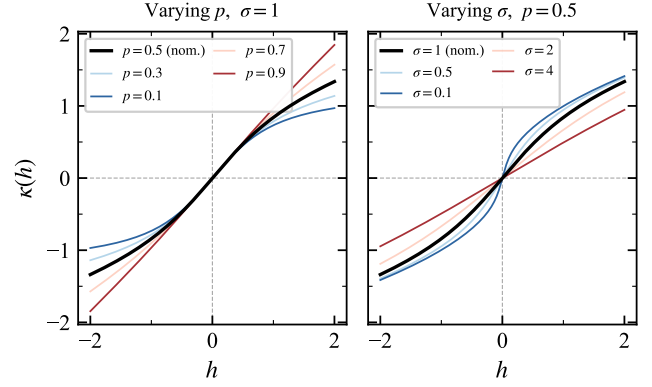
$$r_t = \begin{cases} -10 & \text{collision,} \\ K(\varphi)(r_{\text{pos}} + r_{\text{prox}} + r_{\text{vel}} & \text{otherwise.} \\ + r_{\text{lin}} + r_{\text{stab}} + P_{\text{spd}} \\ + P_{+x} + P_{\text{ctrl}} + P_{\text{TTC}} \end{cases} \quad (16)$$

**3.4.3 Composite CBF-based Safety Filter** Beyond the aforementioned navigation approaches –which combine map-based safety of the `planning` module with reactive collision avoidance control– the `UASTack` further provides a last-resort safety filter. The rationale for adding this final layer is twofold. On the one hand, both the Neural NMPC through Signed Distance Field Encoding for Collision Avoidance (SDF-NMPC) and the DRL navigation strategies involve deep neural network processing, which, despite training to consider noise and other imperfections, is treated as a source of possible (albeit unlikely) error. On the other hand, using fundamentally different collision-checking at different spatiotemporal scales –spanning map-based planning, the navigation strategies, and the safety filter– offers resourcefulness. It thus reflects a conservative but meaningful choice to safeguard the robot from a collision which represents one of the most problematic events during a mission.

Based on Composite Control Barrier Functions (C-CBFs) formalism for safe navigation [Harms et al. \(2025\)](#), we compose a C-CBF directly from recent range measurements as in [Misyats et al. \(2025\)](#) to modify the acceleration setpoint when an unexpected impending collision is detected. It is a key module to fully and formally safeguard autonomous robots. The C-CBF is described hereafter considering the case of a flying robot. First, the system model is approximated to be of degree 2 and takes the form:

$$\mathbf{x} = \begin{bmatrix} \mathbf{p}_{\text{WB}}^W \\ \mathbf{v}_{\text{WB}}^W \end{bmatrix}, \quad \mathbf{u} = [\mathbf{a}^W]. \quad (17)$$

For a rotorcraft such as a multirotor aerial robot, we here use the simplified linear system model

**Figure 7.** Visualization of the used kappa function with nominal values  $\lambda = 1, p = 0.5, \sigma = 1$ .

$$\dot{\mathbf{x}} = \underbrace{\begin{bmatrix} \mathbf{0}_3 & \mathbf{I}_3 \\ \mathbf{0}_3 & \mathbf{0}_3 \end{bmatrix}}_{f(\mathbf{x})} \mathbf{x} + \underbrace{\begin{bmatrix} \mathbf{0}_3 \\ \mathbf{I}_3 \end{bmatrix}}_{g(\mathbf{x})} \mathbf{u}, \quad (18)$$

where  $\mathbf{a}_{\text{WB}}^W$  is the linear acceleration. Here  $f(\mathbf{x})$  and  $g(\mathbf{x})\mathbf{u}$  denote the state system dynamics vectors.

Considering the above, the method then represents the “free-space” set as  $\mathcal{C}_{\mathbf{x}} = \bigcap_{i=1}^N \{\mathbf{x} : \|\mathbf{p}_{\text{WB}}^W - \mathbf{p}_{\text{WO}_i}^W\|^2 \geq \varepsilon\}$  with  $\varepsilon > 0$  representing safety radius around each obstacle point  $\mathbf{p}_{\text{WO}_i}^W$ . A condensed set of  $N$  points is obtained by means of the most recent, sparsified depth observation. This is then associated with equivalent scalar “distance-squared” functions  $\nu_{i,0}(\mathbf{x}) := \|\mathbf{p}_{\text{WB}}^W - \mathbf{p}_{\text{WO}_i}^W\|^2 - \varepsilon^2$  with the safety for obstacle  $i$  being  $\nu_{i,0} \geq 0$ . Note that there is no dependence on any consistent world frame as only the relative distances are used in the construction. Subsequently, we define higher-order CBF (HO-CBF) functions as:

$$\nu_i := \mathfrak{L}_f \nu_{i,0} - \varsigma(\nu_{i,0}), \quad (19)$$

where  $\mathfrak{L}_f$  is the Lie derivative along the drift dynamics and  $\varsigma$  is a tunable class  $\mathcal{K}_{\infty}$  function of the form

$$\varsigma(h) = \lambda \cdot h (h^2 + \sigma^2)^{(p-1)/2}. \quad (20)$$

The used function  $\varsigma$  with parameters  $\lambda > 0, \sigma > 0, p > 0$  is displayed in Fig. 7. For  $p < 1$  the tuneable parameters allow for a more rapid convergence behavior than a for  $p = 1$ .

We formulate the C-CBF as

$$h(\mathbf{x}) := -\frac{\gamma}{\kappa} \log \left( \sum_{i=1}^N e^{-\kappa \tanh(\nu_i(\mathbf{x})/\gamma)} \right), \quad (21)$$

with saturation parameter  $\gamma$  and temperature parameter  $\kappa$ .

To enforce invariance of the safe set  $\mathcal{X}_{\text{safe}} = \{\mathbf{x} \mid h(\mathbf{x}) \geq 0\}$ , the condition for a Robust Control Barrier Function (R-CBF) [Nanayakkara et al. \(2025\)](#) reads

$$\mathfrak{L}_g h(\mathbf{x})\mathbf{u} \geq \vartheta(\mathbf{x}), \quad (22)$$

$$\vartheta(\mathbf{x}) := -\mathfrak{L}_f h(\mathbf{x}) - \alpha h(\mathbf{x}) + \rho(\|\mathfrak{L}_g h(\mathbf{x})\|), \quad (23)$$

for a scalar  $\alpha \in \mathbb{R}^+$  and a *robustness function*  $\rho(y) = \rho_1 y + \rho_2 y^2$ . For a valid C-CBF  $h$ , the satisfaction of condition (22) is sufficient to ensure forward invariance of the safe set  $\mathcal{X}_{\text{safe}}$ , even for inputs with unknown, additive disturbances  $\mathbf{d}$  added

to the undisturbed input  $\mathbf{u}_n$ , e.g.  $\mathbf{u} = \mathbf{u}_n + \mathbf{d}$ , accounting for tracking errors satisfying  $\|\mathbf{d}\| \leq \inf_{y \in \mathbb{R}_{\geq 0}} \frac{\rho(y)}{y}$  in the low-level controllers. This scheme can thus be used to certify collision-free navigation in spite of imperfect tracking. We enforce the condition (22) for a nominal input  $\mathbf{u}_{sp}$  by means of a reactive safety filter Quadratic Programming (QP) of the form

$$\begin{aligned} \mathbf{u}^* &= \arg \min_{\mathbf{u} \in \mathbb{R}^3} \|\mathbf{u} - \mathbf{u}_{sp}\|^2 \\ \text{s.t. } & \mathcal{L}_g h(\mathbf{x}) \mathbf{u} \geq \vartheta(\mathbf{x}). \end{aligned} \quad (24)$$

For the case of one single constraint, an analytical solution to (24) can be computed Alan et al. (2023) as

$$\mathbf{u}^* = \mathbf{u}_{sp} + \max(0, \eta(\mathbf{x})) \mathcal{L}_g h(\mathbf{x})^\top, \quad (25)$$

where

$$\eta(\mathbf{x}) = \begin{cases} -\frac{\mathcal{L}_g h(\mathbf{x}) \mathbf{u}_{sp} - \vartheta(\mathbf{x})}{\|\mathcal{L}_g h(\mathbf{x})\|^2} & \text{if } \mathcal{L}_g h(\mathbf{x}) \neq \mathbf{0} \\ 0 & \text{if } \mathcal{L}_g h(\mathbf{x}) = \mathbf{0}. \end{cases} \quad (26)$$

This computationally cheap and flexible scheme to reactively enforce collision avoidance of any higher level control policy. To further reduce chattering of the safety filter, we further apply Exponential Moving Average (EMA) filtering to the output.

**3.4.4 Ablation Studies** A set of evaluation studies are conducted using a simulated quadrotor with mass 2.10 kg and dimensions  $0.3 \times 0.3 \times 0.1$  m in Gazebo Koenig and Howard (2004). The robot is equipped with an acceleration and yaw-rate tracking controller and a hemispherical dome LiDAR sensor modeled after the RoboSense Airy (FoV  $180^\circ \times 90^\circ$ ). The performance of the ExRL and the SDF-NMPC methods is compared both with and without the C-CBF-based safety filter, across environments of varying density, and under different levels of command mismatch induced by an independent first-order low-pass filter with time constant  $\tau_d$  on each acceleration and yaw-rate command dimension. The slower dynamics introduced by the low-pass filter serve to practically emulate the effects of the closed-loop attitude response of the system, which presents non-instantaneous reference tracking and at times imperfect disturbance rejection. This is of particular interest especially as the actual time constant of the attitude subsystem differs between robots and delayed response poses a challenge to navigation in tight spaces. This allows us to characterize the failure modes of the navigation policies induced by increasingly disturbed system behavior.

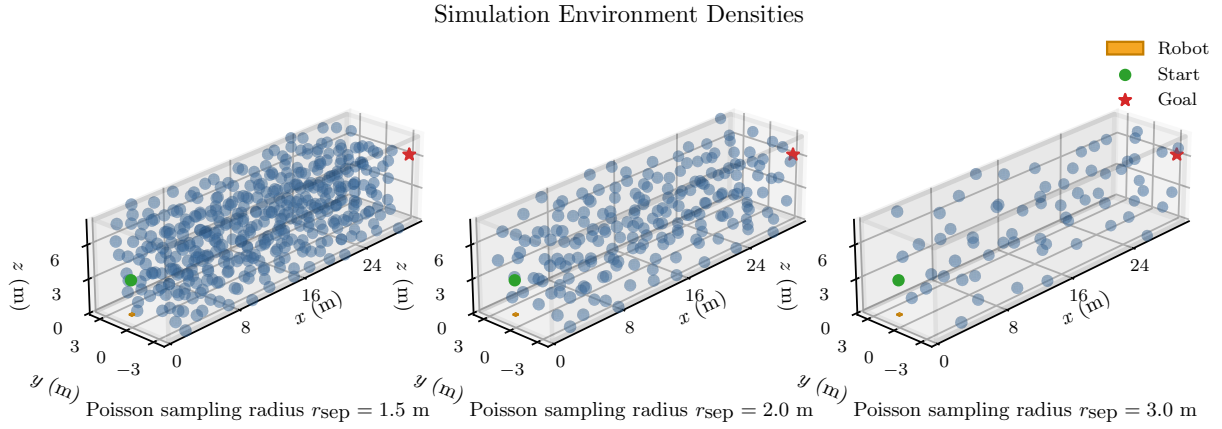
Test environments, illustrated in Figure 8a, are procedurally generated as rectangular corridors of width and height 8 m each, populated with spherical obstacles of 1 m diameter placed using Poisson-disc sampling, guaranteeing a parametric minimum separation  $r_{sep} \in \{1.5, 1.8, 2.0, 2.5, 3.0\}$  m between obstacle centers, i.e., surface-to-surface gaps of  $\{0.5, 0.8, 1.0, 1.5, 2.0\}$  m. The corridor is bounded above, below and on the sides by walls, leaving the longitudinal direction open for traversal. The robot is initialized at the start of the corridor and tasked with following a path through the corridor to the other side.

For each environment, and for each value of the low-pass time constant  $\tau_d$ , 20 independent runs are performed with each of the four configurations and the outcomes are visualized in Figure 8b. Every run terminates in one of three mutually exclusive states: *success*, in which the robot reaches the goal; *stagnation*, in which the robot halts before the goal but remains collision-free; or *crash*, in which a collision with the environment is detected. The figure reports the rate of each outcome as a function of  $r_{sep}$ , with rows corresponding to the three outcome categories and columns to the four values of  $\tau_d$ . Smaller  $r_{sep}$  values correspond to denser, more constrained environments, while larger  $\tau_d$  values correspond to a more severe command mismatch. Solid lines indicate the C-CBF-filtered configurations and dashed lines the baselines without this last-resort filter, with colour distinguishing the upstream policy (ExRL in blue, SDF-NMPC in green). Each marker aggregates the 20 runs for the corresponding combination of parameters.

Two sets of comparisons are performed. Among the values of  $\tau_d$  tested,  $\tau_d \leq 0.10$  s corresponds to the realistic operating regime that the studies are intended to characterize;  $\tau_d = 0.25$  s is included as a deliberate stress test, beyond realistic deployment conditions, in order to probe the limits of each configuration and expose the regime in which the safety ceases to hold. Because both *success* and *stagnation* outcomes correspond to collision-free behaviour, the *crash* rate is treated as the primary safety metric throughout, while the success rate is reported as a secondary but important measure of task completion.

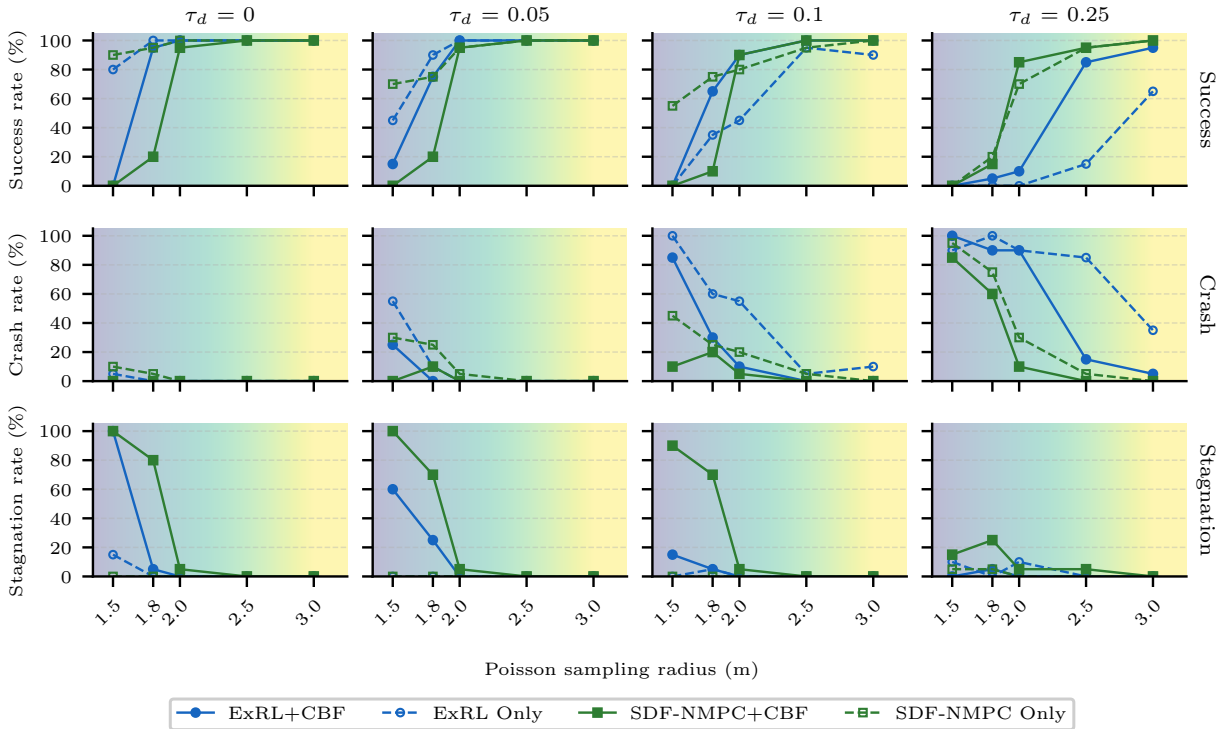
The first comparison contrasts the two unfiltered baselines, ExRL only and SDF-NMPC only, which differ markedly in how they degrade under increasing  $\tau_d$ . At  $\tau_d = 0$  both reach the goal on 80–100% of runs across all densities, with the ExRL policy crashing on 5% of the densest layouts and SDF-NMPC on 10%. As  $\tau_d$  grows, the two baselines diverge sharply. SDF-NMPC degrades gracefully and primarily along the density axis  $r_{sep}$ . At  $\tau_d = 0.25$  s it still succeeds on 100% of runs at  $r_{sep} = 3.0$  m and on 95% at  $r_{sep} = 2.5$  m, with crashes concentrated in the dense environment setup. ExRL, in contrast, degrades globally: at the same  $\tau_d$  it crashes on 85–100% of runs across the three densest settings and even at  $r_{sep} = 3.0$  m retains only 65% success. This asymmetry may reflect SDF-NMPC’s robustness against the induced mismatch, while the learned policy’s reliance on a specific dynamics model employed during training and the subsequent degradation wherever it departs from that model.

The second comparison contrasts each baseline against its C-CBF-augmented counterpart. At  $\tau_d = 0$ , the safety filter eliminates collisions entirely and converts results into stagnations rather than goal completions, preserving safety at the cost of task completion. The filter’s protective effect persists across the realistic regime. At  $\tau_d = 0.10$  s, SDF-NMPC+C-CBF crashes on at most 20% of runs in any environment, always lower than SDF-NMPC alone, and ExRL+C-CBF crashes on 10–85% in the dense band, again lower than ExRL alone. This indicates a substantial reduction in crash rate with the inclusion of the C-CBF. Under the unrealistic  $\tau_d = 0.25$  s conditions, the filter loses authority in the densest environments and both augmented pipelines crash on 85–100% of runs at  $r_{sep} = 1.5$  m,



(a) Procedurally generated test environments used in the ablation studies regarding the `navigation` module. Each environment is a rectangular corridor bounded above, below, and on the sides by walls, with the longitudinal direction left open for traversal. Spherical obstacles of 1 m diameter are placed via Poisson-disc sampling with a parametric minimum separation  $r_{sep}$  between obstacle centers, with lower values representing denser environments. The robot dimensions are visualized in each environment.

Ablation Study — Outcome Rates vs. Obstacle Density



(b) Outcome rates across density (horizontal axis,  $r_{sep}$ ) and command mismatch (columns,  $\tau_d$ ). Rows show *success*, *crash*, and *stagnation* rates over 20 runs for each case. Solid lines: C-CBF-filtered; dashed: unfiltered. Blue: ExRL; green: SDF-NMPC.

**Figure 8.** Ablation study comparing ExRL and SDF-NMPC navigation policies, with and without the C-CBF last-resort safety filter, across obstacle densities (8a) and a sweep of the time constant  $\tau_d$  (8b).  $\tau_d \leq 0.10$  s approximately corresponds to the realistic operating regime;  $\tau_d = 0.25$  s is unrealistic. Since *success* and *stagnation* both correspond to collision-free behaviour, the crash rate is the primary safety metric.

locating the failure boundary that the test is designed to expose. The augmented versions inherit the characteristics of their upstream policy: ExRL+C-CBF crashes earlier and across a wider density range than SDF-NMPC+C-CBF at every  $\tau_d > 0$ , indicating that the C-CBF compensates for command distortion but not for the upstream policy's own degradation under that distortion. This analysis shows that imperfect control can occur in demanding environments and conditions, highlighting the need for navigation strategies

with multiple layers of safety checking and avoidance. The UAstack offers a configurable methodological plurality to support demanding deployments.

**3.4.5 Exteroceptive Overwrite** When the map-based safety of planning module or the specific exteroceptive navigation methods are not desirable for, or compatible with, a given robot, the UAstack allows the use of a conventional state-feedback controller. Examples include the Linear MPC

methods in Greeff and Schoellig (2018); Kamel et al. (2017), the underlying MPC in SDF-NMPC with disabled collision constraints, or a solution for any other particular robot or through existing autopilot (e.g., PX4).

### 3.5 Low-level Interfaces

The UAstack interfaces diverse aerial and ground robots as follows. Although extendable in principle, the currently provided open-source interfaces are as follows:

*Aerial Robots - Full Stack:* When the full stack with multi-layered safety is considered for flying systems, we command acceleration setpoints directly to compatible autopilots and low-level controllers such as PX4- and ArduPilot-based flight controllers.

*Aerial Robots - Without Multi-layered Safety:* If the multi-layered safe navigation is not necessary for flying systems, we provide options for commanding waypoints or 3D accelerations to existing controllers. Waypoints are straightforward for all systems that offer such control. However, this does not deliver the full stack functionality and collision avoidance is ensured only at the map/planning level.

*Ground Robots:* For legged systems and other ground robots, we interface the planning module with a custom PID tracking controller to output velocity commands to follow the path given by the planning module. Velocity-setpoint commands are provided to the platforms for them to track. Those velocity references may be passed through other safety-mechanisms in case those are provided onboard the platforms.

Direct support for widely-adopted low-level control or autopilot interfaces is available out-of-the-box through MAVROS, or more broadly through the ROS framework. As the stack is structured in a Dockerized format, we support both ROS 1 and ROS 2-based robots out of the box.

## 4 Evaluation Studies

To validate the UAstack, a comprehensive set of evaluation studies was conducted including (a) evaluation of the performance, accuracy and overall resilience of the perception module in diverse environments and conditions, (b) evaluation of the performance and safety-inducing behaviors of the navigation module, as well as (c) full-stack results requiring the orchestrated operation of the perception, planning and navigation modules. Studies were conducted using both aerial and ground robots, alongside some handheld experiments (as part of the evaluation regime of the perception module). An overview of these experiments is shown in Table 5 and key parameters are listed in Table 6. All presented field experiments are included in the video files of the submission and can be found at <https://youtube.com/playlist?list=PLu70ME0whad9KCs5PHx-35-qpyK14yZYi&si=E-QJCTTyfhfFUqFo>.

### 4.1 Verified Robot Morphologies

In this paper, we evaluate the UAstack on two multirotor robot configurations and a legged robot. In all robot missions, the UAstack runs fully onboard in real-time,

with module configurations as detailed in Table 5. The released open-source code involves simulation examples with additional morphologies such as ground rovers and helicopters. Verifying on diverse robots – while further expanding the morphologies we support – is aligned with our strategic goal to provide a generalist autonomy stack across broad morphological categories.

#### 4.1.1 Multirotors

*Aerial Robot 1 (AR-1):* The first aerial robot, referred to as AR-1, is an improved version of the RMF-Owl Petris et al. (2022). AR-1 integrates a Khadas Vim4 computer and a sensing suite comprising of an Ouster OS0-128 LiDAR (10 Hz), a Flir Blackfly S 0.4 MP color camera (20 Hz normally, 25 Hz in Fyllingsdal), a Texas Instruments mmWave IWR6843AOP radar sensor (10 Hz normally, 25 Hz in Fyllingsdal), and a VectorNav VN-100 IMU (200 Hz). The sensors and the onboard computer are time synchronized using a separate microcontroller as described in Nissov et al. (2025).

*Aerial Robot 2 (AR-2):* AR-2 is a collision-tolerant quadrotor designed for autonomous operation in GNSS-denied confined environments. AR-2 features a lightweight protective frame made from carbon-foam sandwich measuring approximately  $0.52 \times 0.52 \times 0.24$  m (L  $\times$  W  $\times$  H), weighing 2.3 kg. The robot carries the UniPilot Kulkarni et al. (2025a) sensing and computing payload on which the entire UAstack runs onboard. The module features an NVIDIA Jetson Orin NX as the compute module and a multi-modal sensing suite including a RoboSense Airy dome LiDAR (10 Hz),  $3 \times$  MIPI Vision Components IMX296 color cameras (20 Hz), a D3 Embedded RS-6843AOPU FMCW radar (10 Hz), and a VectorNav VN-100 IMU (200 Hz). The onboard sensors are time-synchronized following the work in Kulkarni et al. (2025a) AR-2 further integrates a Pixracer Pro PX4-based flight control to track the acceleration commands given by the UAstack.

#### 4.1.2 Legged Robots

*Ground Robot 1 (GR-1)* On the ground, the UAstack is evaluated using the ANYmal D legged robot – hereafter referred to as GR-1 – with dimensions of  $0.93 \times 0.53 \times 0.80$  m (L  $\times$  W  $\times$  H), and a mass of 50 kg. The stock standard robot features a Velodyne VLP-16 LiDAR and  $6 \times$  depth cameras for sensing and two 8th-generation Intel Core i7 CPUs (6 cores each) for compute. However, GR-1 is also equipped with the UniPilot module which runs the UAstack for all evaluations. This UniPilot carries the same sensing payload as in the AR-2 platform and is interfaced with the onboard Intel computers which then run the locomotion and velocity tracking controllers. All the stack runs on the onboard UniPilot, considering the data of this module.

### 4.2 Perception Module Evaluation

We first evaluate the performance and resilience of the stack’s perception module, focused around its multi-modal SLAM functionalities. We subsequently evaluate downstream functionalities for VLM-based scene reasoning.

**Table 5.** Overview of the different experiments composing the evaluation.

Purpose	Environment	Robot	U <sub>Astack</sub> Module(s) <sup>1</sup>	Perceptual Challenge(s)	Geometric Challenge(s)
SLAM Validation	Fyllingsdal	AR-1	S	Self-similarity	–
	Runehamar	AR-1	S	Low-light	–
	Frozen Lake	AR-1	S	Self-Similarity	–
	Campus	Handheld	S+V	Visual obscurants	–
Safety Validation	Forest	AR-2	S <sub>LRI</sub> +R+C	Thin features	Thin obstacles and cluttered
		AR-2	S <sub>LRI</sub> +N <sub>S</sub> +C		
		AR-2	S <sub>LRI</sub> +N <sub>U</sub> +C		
	Campus	AR-2	S <sub>LRI</sub> +P <sub>E</sub> +R+C	–	Moving obstacles
AR-2		S <sub>LRI</sub> +P <sub>E</sub> +N <sub>S</sub> +C	–		
Full-Stack Validation	Forest	AR-2	S <sub>LRI</sub> +P <sub>E</sub> +R+C	Thin features	Thin obstacles and cluttered
		AR-2	S <sub>LRI</sub> +P <sub>E</sub> +N <sub>S</sub> +C		
	Mine	AR-2	S <sub>LRI</sub> +P <sub>E</sub> +R+C	Low-light	Narrow and multiple branches
		AR-2	S <sub>LRI</sub> +P <sub>E</sub> +N <sub>S</sub> +C		
		GR-1	S <sub>LI</sub> +P <sub>E</sub>		
	Ship	AR-2	S <sub>LI</sub> +P <sub>E</sub> +P <sub>I</sub>	Low-light	–
Campus	GR-1	S <sub>LRI</sub> +P <sub>E</sub> +V	–	Narrow, varying size, and multiple branches	

<sup>1</sup> Which modules of the U<sub>Astack</sub> were used, including SLAM (denoted by S, with a subscript denoting the configuration used in autonomous missions, where L: LiDAR, R: Radar, I: IMU), VLM (denoted by V), Planning (denoted by P, while P<sub>E</sub> refers to exploration and P<sub>I</sub> to inspection), ExRL (denoted by R), SDF-NMPC (denoted by N<sub>S</sub>), SDF-NMPC without SDF constraints (denoted by N<sub>U</sub>), and C-CBF (denoted by C).

**4.2.1 Multi-Modal SLAM** To evaluate the multi-modal SLAM solution, we assess its accuracy and robustness in perceptually-degraded conditions. Considering a set of diverse environments, specifically a bicycle tunnel (Fyllingsdal), a road tunnel (Runehamar), a frozen lake, and the NTNU main campus, we present a modality-wise ablation as well as comparisons against state-of-the-art methods. The goal of this evaluation is to demonstrate the flexibility of the proposed SLAM system, as well as the comparative advantages of the multi-modal fusion. These experiments are collected with ground truth, such that the estimation performance can be evaluated quantitatively. The same SLAM system runs online to support the autonomous missions conducted in all the other experiments. For these autonomous missions, the SLAM module is operating in the **Ours - LRI** (fusing LiDAR, radar, IMU) configuration, except when noted otherwise (see Table 5), as this has been found to be most robust across diverse environments and conditions.

The results of the evaluation are presented in Table 7. The table compares and ablates our multi-modal solution against state-of-the-art LiDAR-Inertial (FAST-LIO2 Xu et al. (2022)), Visual-Inertial (ROVIO Bloesch et al. (2017) and OpenVINS Geneva et al. (2020b)), LiDAR-Visual-Inertial (FAST-LIVO2 Zheng et al. (2025)), and LiDAR-Radar-Inertial (GaRLIO Noh et al. (2025) and AF-RLIO Qian et al. (2025)) works. GaRLIO and AF-RLIO are selected as a representative set of state-of-the-art methods for LiDAR-radar-inertial fusion which are both: likely to work with the small form-factor sensors considered in this work and with open-source implementations. The different permutations of

our MIMOSA-X multi-modal SLAM (LiDAR (**L**), Radar (**R**), Vision (**V**), and Inertial (**I**)) are noted in the table as **Ours - XXXI**. As the IMU is an integral component of our method, permutations without IMU are omitted. The key parameters used in the evaluation of the SLAM module are reported in Table 6. Note that all parameters are fixed across all tests, with the sole exception of the LiDAR point standard deviation (which is increased in the frozen lake environment), the IMU bias noise densities (decreased in the frozen lake environment), and the D-Optimality threshold for the vision fusion (which is different between environments with and without fog). In turn, the latter is one of the reasons that the robot experiments presented subsequently predominantly rely on the LRI solution. The table reports the Absolute Trajectory Error (ATE) (in m) and Relative Trajectory Error (RTE<sub>10</sub>) (in %), with 10m segment length, following Grupp (2017), calculated against the ground truth estimates. The ground truth for the tunnel trajectories (Fyllingsdal and Runehamar) is generated by fusing the tracking of a Leica GRZ101 mini-prism mounted on AR-1 by a Leica MS60 MultiStation with the onboard IMU in an offline Levenberg–Marquardt (LM) optimization. In the campus and frozen lake datasets, where GNSS is available, ground truth is created using Pix4DMatic for a GNSS-augmented visual bundle adjustment optimization.

The SLAM datasets were collected with (a) AR-1 aerial robot and (b) a helmet-mounted modified version of the UniPilot Kulkarni et al. (2025a) module integrating a Hesai JT-128 LiDAR (10Hz), replacing the Robosense Airy, and a uRAD Industrial radar (10Hz), replacing the 3D Embedded RS-6843AOPU radar (both of which integrate

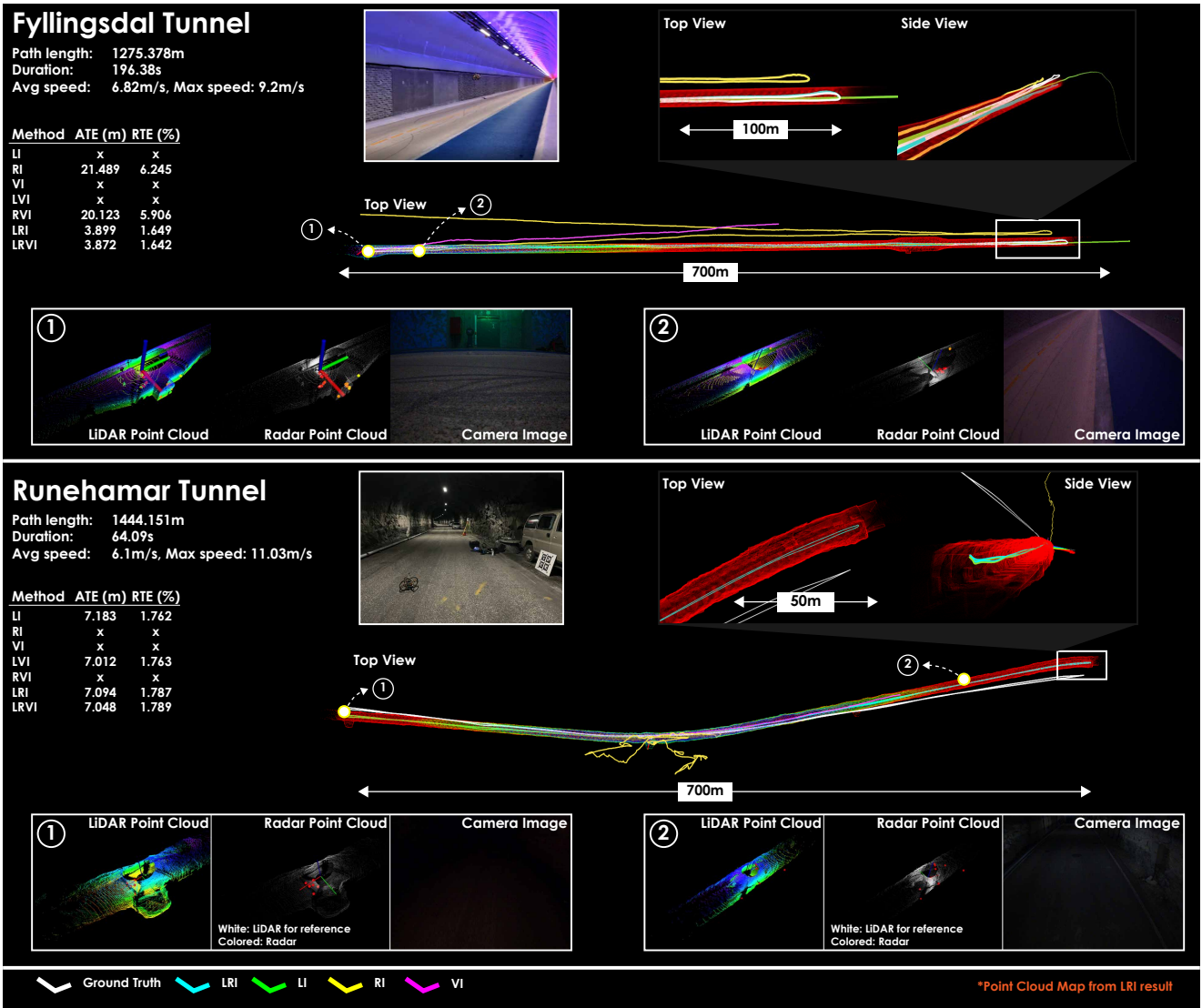


**Figure 9.** Overview of the SLAM performance in the two tunnel environments. The Fyllingsdal tunnel presents an environment with geometric self-similarity, thus causing divergence in LiDAR-geometry-based methods. Multi-modal fusion demonstrates increased performance, by replacing the missing observability of the LiDAR measurements with information from either radar or vision. The Runehammar tunnel contains sections of near geometric self-similarity, too short to cause widespread divergence. This environment also has sections with low-lighting and poor radar returns, complicating state estimation. Again the multi-modal fusion demonstrates robust performance.

the Texas Instruments IWR6843AOP chip). The full datasets including raw data and ground-truth are released to facilitate comparison and reproducibility.

**Fyllingsdal Tunnel** The AR-1 aerial robot was manually piloted at an average speed of 6.82 m/s (max speed 9.2 m/s) in a ~650m section of the Fyllingsdal bicycle tunnel. The tunnel is composed primarily of long geometrically self-similar sections with sparse geometrically dissimilar rest areas. Ground truth for this environment is generated using the Leica-IMU fusion described above. Notably, the chirp configuration for the radar in this experiment is changed for better performance at high speeds. This results in a greater maximum Doppler as well as an increased measurement rate of 25 Hz. GaRLIO could not be evaluated on this sequence as the implementation requires the radar and LiDAR to be at the same rate. Due to the geometric self-similarity affecting the LiDAR optimization, FAST-LIO2 as well as **Ours - LI** failed. AF-RLIO fails similarly, due to the method relying on radar-based scan registration during periods of LiDAR degeneracy, which the small form-factor

radar sensor used on the aerial platform is not well-suited for. The radar-inertial ablation (**Ours - RI**), while able to function, has a significant vertical and yaw drift due to the nature of the sensor. Furthermore, the high speeds created difficulties for vision-based methods, resulting in significant performance deterioration for ROVIO. As a result, **Ours - VI** fails, and **Ours - RVI** does not see large performance improvements over **Ours - RI**. OpenVINS performed better than ROVIO, **Ours - VI**, **Ours - RVI**, and **Ours - LVI**, however still not as well as the nominal multi-modal configuration **Ours - LRI** and **Ours - LRVI**. The proposed method, by fusing the multiple exteroceptive modalities, demonstrates performance robust both to the challenging conditions, but also to the asynchronous measurements, leading to the improved results of **Ours - LRI**, and **Ours - LRVI**. Similarly, FAST-LIVO2 is able to leverage the vision information to outperform most of the other methods, achieving performance similar to, but slightly worse than, **Ours - LRI** and **Ours - LRVI**. The estimated trajectories,

**Table 6.** Key parameters used in the evaluations.

Module	Parameter	Value	Unit <sup>1</sup>
SLAM	$\eta_p$	0.2	m
	$n_p$	20	–
	$\sigma_{\epsilon_{\mathcal{L}}}$ (nom.)	0.07	m
	$\sigma_{\epsilon_{\mathcal{L}}}$ (lake)	0.18	m
	Radar FoV	$120 \times 120$	°
	Map update thresholds	1	m
		10	°
	D-Opt. (nom.)	0.02	–
	D-Opt. (fog)	0.001	–
	Planner	$v_m$	0.2
$v_h$		0.2	m
$\mathbf{b}_R$ (AR-2)		$0.8 \times 0.8 \times 0.8$	m
$\mathbf{b}_R$ (GR-1)		$1.0 \times 1.0 \times 0.4$	m
$\mathbf{b}_L$ (AR-2)		$30.0 \times 30.0 \times 4.0$	m
$\mathbf{b}_L$ (GR-1)		$40.0 \times 40.0 \times 4.0$	m
FoV of $\mathcal{D}$		$180 \times 90$	°
FoV of $\mathcal{C}$		$118 \times 94$	°
$d_{view}$		1.25	m
$d_{path}$		2.0	m
SDF-NMPC	$T_{SDF}$	1.0	m
	$d_{max}$	5.0	m
	$r$	0.5	m
ExRL	$u_n^x$	2.0	m/s <sup>2</sup>
	$u_n^y$	2.0	m/s <sup>2</sup>
	$u_n^z$	1.5	m/s <sup>2</sup>
	$u_n^\psi$	$\frac{\pi}{3}$	rad/s
C-CBF	$\lambda$	3.0	–
	$\sigma$	0.3	–
	$p$	0.8	–
	$\rho_1$	0.5	–
	$\rho_2$	0.5	–
	$\alpha$	4.0	–
	$\kappa$	80.0	–
	$\gamma$	40.0	–
	$\varepsilon$	0.3	m
	$N$	256	points

<sup>1</sup> Unitless quantities denoted by –.

ground truth and the accumulated LiDAR point cloud map from the **Ours - LRI** configuration is visualized in Figure 9.

*Runehamar Tunnel* The AR-1 aerial robot was manually flown through a section of the Runehamar tunnel, for a total trajectory length of  $\sim 1.4$  km. Ground truth for this environment is generated using the Leica-IMU method described above. The tunnel has a rough interior, which allows for LiDAR-based methods (FAST-LIO2 and **Ours - LI**) to function well despite the otherwise minor geometric self-similarity. However, regions of the tunnel are not illuminated. Despite the aerial platform carrying onboard lighting, the scale of the environment is such that the images captured by the camera are dark and hence challenging for visual-based methods, leading to very poor performance from ROVIO (and hence **Ours - VI**). OpenVINS, by doing a histogram equalization of the image is able to better

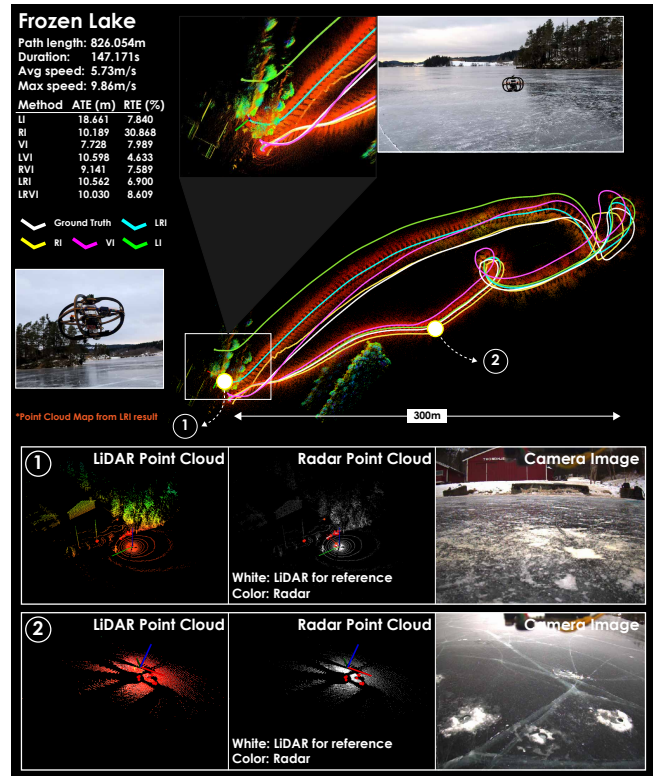


**Figure 10.** Overview of the SLAM performance in the Frozen Lake environment, comparing different uni-modal approaches with the multi-modal LRI configuration. This environment presents difficulty for methods relying only on LiDAR or radar. For the former, the planar geometry of the environment can result in lacking observability in lateral position and yaw. For the radar, the limited number of returns results in increased drift.

extract features from the darkest regions and as a result, demonstrates improved performance over ROVIO, however, still worse than the LiDAR-based fusions. Impacted by the poor visual measurement quality, FAST-LIVO2 performs slightly worse than FAST-LIO2. Radar measurement quality in this environment was also quite poor, in part due to the speed of the trajectory and in part due to low number of reflections. As a result **Ours - RI**, **Ours - RVI**, and the baseline radar-fusion methods (GaRLIO and AFRLIO) do not perform well either. However, in combination with the LiDAR (in **Ours - LVI**, **Ours - LRI**, or **Ours - LRVI**) the proposed multi-modal fusion demonstrates robust performance. Some of the aforementioned results are visualized in Figure 9, alongside the previous tunnel experiment. Note here the sparsity of the instantaneous radar point cloud in this particular environment.

*Frozen Lake* The AR-1 aerial robot was manually piloted on top of a frozen lake, starting from close to a bank, flying out into the middle, and returning close to the starting location. The ground truth was generated using the Pix4DMatic bundle adjustment result. Once the robot has traveled further than the range of the LiDAR away from any bank of the lake, the point cloud is geometrically self-similar and resembles a large plane. Notably, the LiDAR point cloud is also affected by the ice such that rays with a large incidence angle on the ice return invalid points and valid points have increased noise standard deviation. The radar after takeoff and before landing mostly returns less than three points per point cloud with frequently empty point

**Table 7.** Metrics for the multi-modal SLAM evaluation, including ATE [m] and RTE<sub>10</sub> [%].

	Fyllingsdal Tunnel	Runehamar Tunnel	Frozen Lake	Campus Fog	
Length [m]	1275.378	1444.151	826.054	669.609	
ATE [m] / RTE <sub>10</sub> [%]	FAST-LIO2	×	6.578 / 1.891	×	
	FAST-LIVO2	4.930 / 2.852	7.881 / 1.805	×	
	GaRLIO	—	×	×	
	AF-RLIO	×	×	×	
	ROVIO	42.851 / 20.295	62.375 / 29.806	3.112 / 7.177	×
	OpenVINS	13.710 / 6.271	13.337 / 5.443	1.985 / 3.700	×
	<b>Ours - LI</b>	×	7.183 / 1.762	18.661 / 7.840	×
	<b>Ours - RI</b>	21.489 / 6.245	×	10.189 / 30.868	14.075 / 6.189
	<b>Ours - VI</b>	×	×	7.728 / 7.989	×
	<b>Ours - LVI</b>	×	7.012 / 1.763	10.598 / 4.633	×
	<b>Ours - RVI</b>	20.123 / 5.906	×	9.141 / 7.589	17.737 / 6.351
	<b>Ours - LRI</b>	3.899 / 1.649	7.094 / 1.787	10.562 / 6.900	7.324 / 4.240
<b>Ours - LRVI</b>	3.872 / 1.642	7.048 / 1.789	10.030 / 8.609	8.345 / 4.231	

Method failure due to ATE > 5% is indicated by × and due to inability to generalize to sensor configuration (radar being at 25Hz) is indicated by —.

For verifiability and reproducibility, the full implementation and the dataset involved in these studies are openly released.

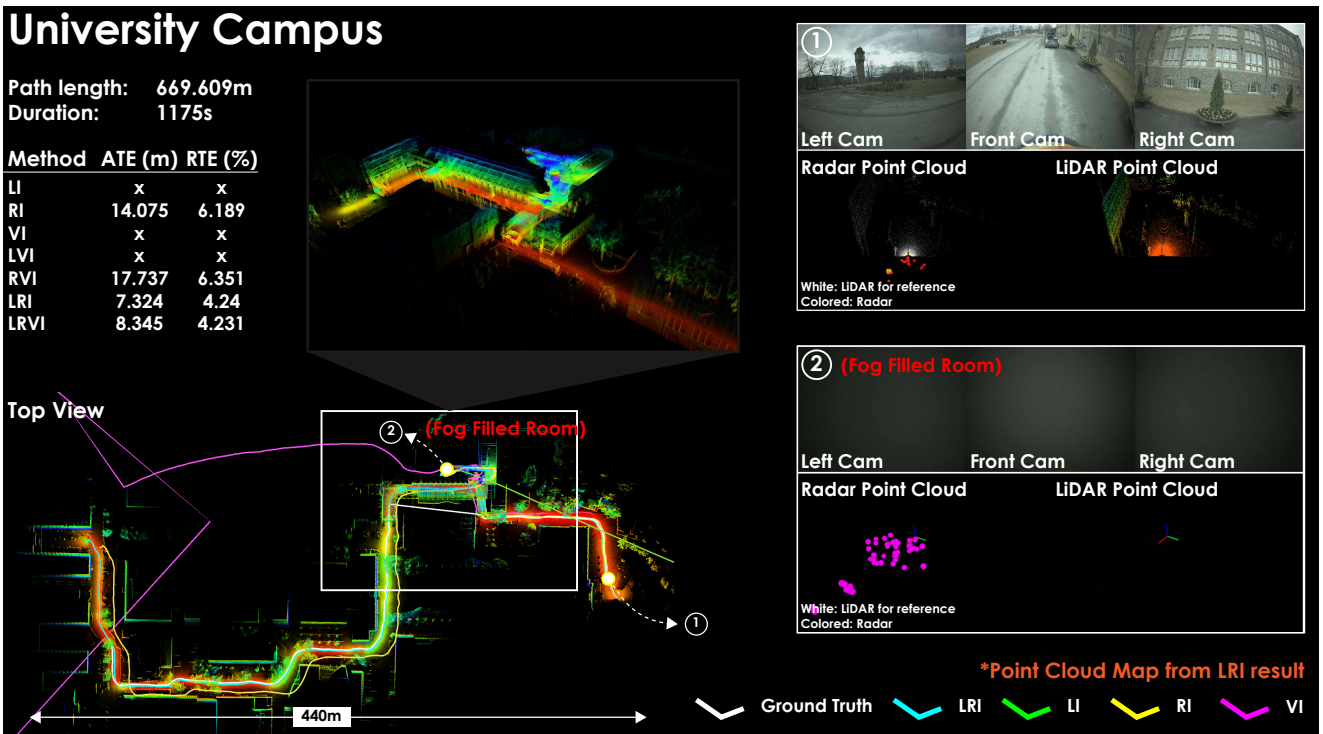


**Figure 11.** Overview of the SLAM performance of the experiment in the campus environment with the handheld module. The experiment has the trajectory passing through a room filled with dense fog, causing large increase of noise present in the LiDAR and vision measurements, whereas the radar remains largely unaffected. The multi-modal fusion retains the accuracy of LiDAR-based methods in nominal conditions alongside the robustness of radar through degraded environments.

clouds. The returns are primarily from the surface directly below the robot as it is flying.

GaRLIO fails in this dataset as it calculates a least-squares estimate of velocity from the radar point cloud for outlier rejection, which requires a minimum of three points. AF-RLIO while functioning initially, quickly breaks once far enough away from the bank due to the sparse radar point clouds. Both FAST-LIO2 and FAST-LIVO2 initially function well, however, their accuracy deteriorates rapidly when the system performs an aggressive yaw maneuver and

accumulates significant error. Despite also based on LiDAR-inertial fusion, **Ours - LI** does not fail in this environment due to parametric differences in **Ours - LI**, that were not replicable in FAST-LIO2, which results in more robust performance. Due to the visually feature-full environment and good outdoor lighting conditions, OpenVINS provides the best baseline performance (followed by ROVIO). Our solution retains performance similar to these baselines across most vision-involving configurations (i.e., **Ours - VI**, **Ours - LVI**, **Ours - RVI**, and **Ours - LRVI**), while it is notable that

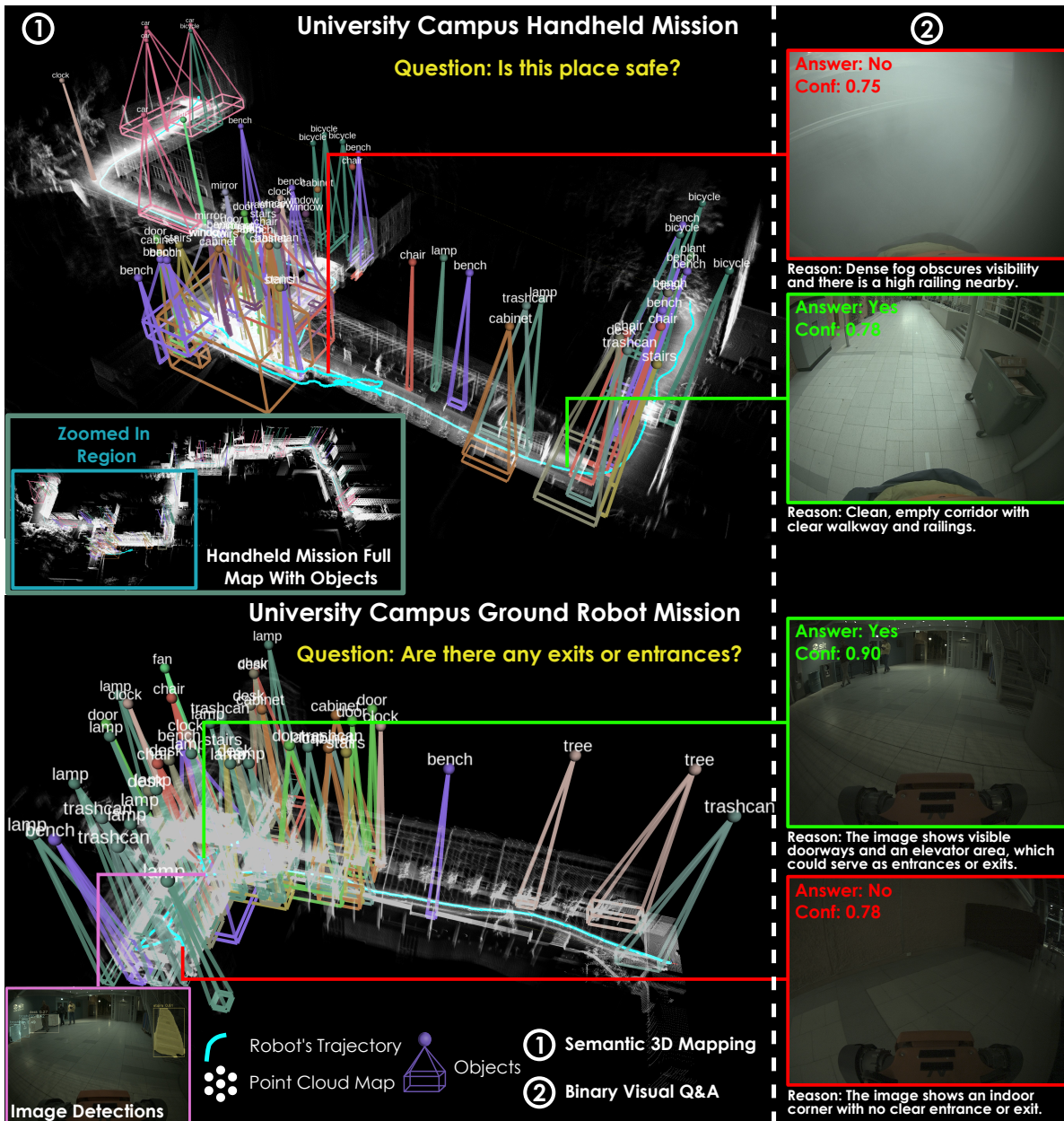


**Figure 12.** Qualitative results of the proposed VLM reasoning system. Left: semantic 3D mapping with open-vocabulary object detections fused into a voxel grid, showing labeled objects and the robot trajectory over time. Right: binary visual question-answering examples, where the model provides “Yes/No” answers with confidence scores and explanations for high-level scene understanding tasks. The figure demonstrates the integration of spatial semantic mapping with high-level reasoning.

**Ours - LI, Ours - RI, and Ours - LRI** remain functional. The performance of the proposed method’s ablation is shown in Figure 10, where the geometric self-similarity of the frozen lake is clear.

*Campus Fog* A handheld UniPilot module is carried through a typical university campus environment, for a total trajectory length of 670 m. The trajectory starts outdoors but proceeds indoors into a fog-filled room before returning outdoors. As a result, the experiment features large variation in the local environment scale as well as dense visual obscurants, which are known to cause problems for LiDAR- and vision-based estimation. The ground truth for this experiment is created using the Pix4DMatic bundle adjustment-based method.

As expected, both the vision- and LiDAR-based methods (i.e., FAST-LIO2, FAST-LIVO2, ROVIO, OpenVINS, **Ours - LI, Ours - VI, and Ours - LVI**) perform well until the room

with visual obscurants (fog), wherein the aforementioned methods accumulate significant error resulting from the extended duration of unusable measurements. The **Ours - RI** ablation functions regardless as the radar is unaffected by such phenomena, however still accumulates drift due to the long mission duration. GaRLIO and AF-RLIO, despite including the radar, are challenged here as well. For the former, the sparseness of the radar point clouds result in challenges with respect to RANSAC-based outlier rejection, and as a result the method fails. For the latter, when LiDAR point cloud degeneracy is detected, the method switches to radar-based registration. This is generally difficult with small form-factor radar sensors, again leading to failure. This also indicates the strengths and inherent robustness of our radar Doppler factor formulation. The proposed multi-modal ablations which include the radar (**Ours - RI, Ours - RVI, Ours - LRI, and LRVI**) perform robustly, as the radar’s

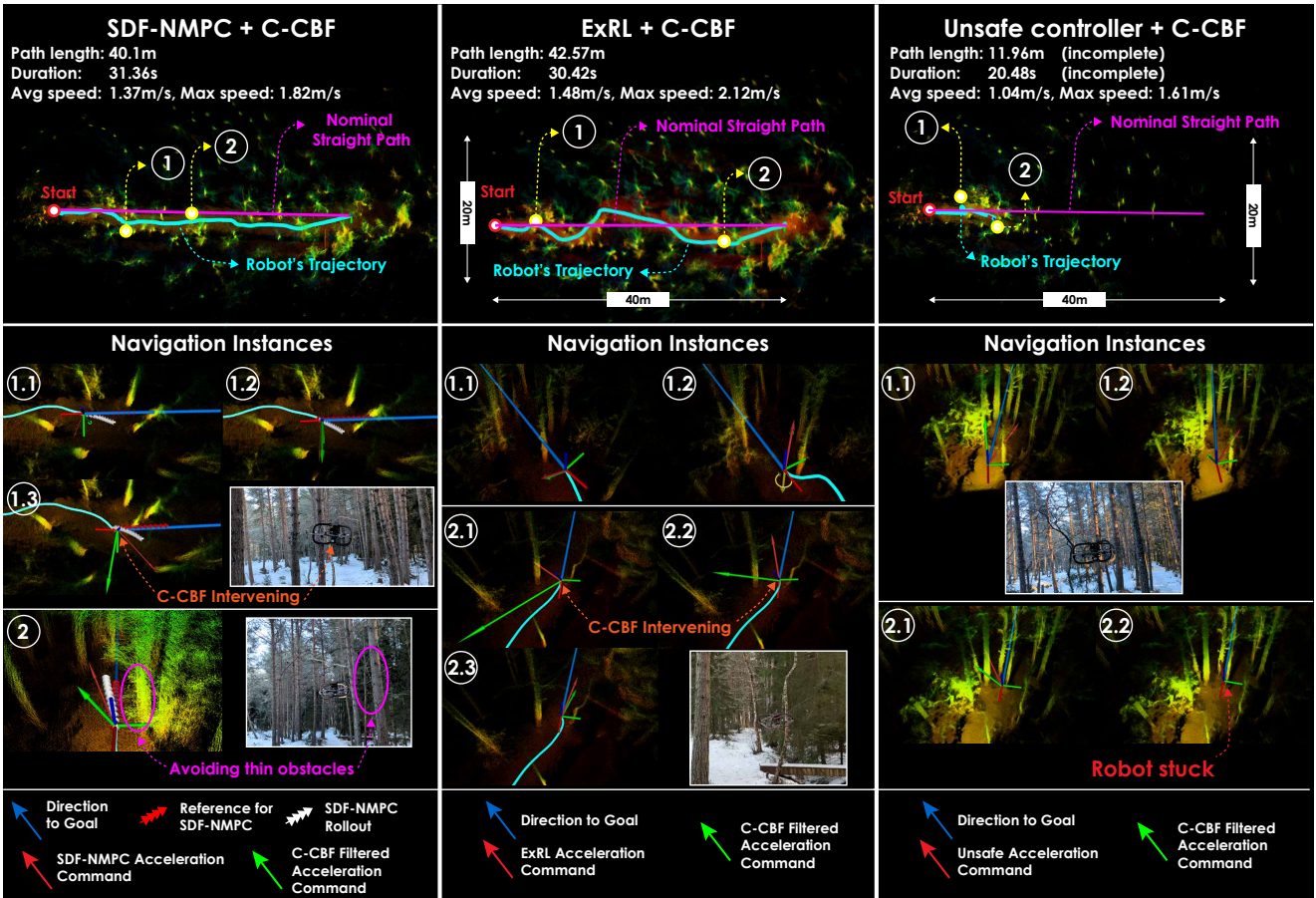


**Figure 13.** Navigation module evaluation is performed in the forest using AR-2 with SDF-NMPC + C-CBF, ExRL + C-CBF, and C-CBF paired with an unsafe policy (SDF-NMPC but with its collision-avoidance constraints disabled) respectively. The robot was tasked to navigate to a waypoint 38 m in front of it, with a reference path going through trees and branches. Individual experiments are shown, with specific instances highlighted. Both the SDF-NMPC + C-CBF and the ExRL + C-CBF methods successfully navigated to the goal location, avoiding obstacles in the path. The C-CBF paired with an unsafe policy does not reach the goal and remains stuck, but remaining safe at all times. The full map is shown with specific instances highlighted.

invariance to visual obscurants is able to be complementarily fused with the accuracy associated with vision- and LiDAR-based methods in suitable conditions. As expected, the ablations which include the LiDAR together with the radar perform best. The results for this experiment are visualized in Figure 11, note in particular the challenge posed on LiDAR- and vision-based sensing by the visual obscurants in the fog-filled room. Here, the LiDAR returns nearly no points and the camera is completely blinded.

**4.2.2 Scene Reasoning** Provided the multi-modal SLAM capabilities of the UStack, we further assess downstream functionality for scene reasoning. Figure 12 presents two real-world examples of the proposed VLM reasoning system. As a straightforward extension to the core perception module capabilities, our open-vocabulary semantic mapping system and 3D object detection are shown on the left side of the figure, where the reconstructed point cloud, together with the bounding boxes of the detected objects, is illustrated. Our semantic mapping pipeline, based on the open-vocabulary object detector, operates at 1 Hz. This result demonstrates the ability of the perception module to consistently maintain semantic understanding over time.

On the right side of Figure 12, we show instances of the visual question/answering module, which provides contextual reasoning beyond geometric perception. As

shown in the examples, the system correctly identifies potentially unsafe conditions in fog with high confidence, as well as determines whether there are exits or entrances in the current view. In our current implementation, GPT-5 is queried through the OpenAI API every 50 s. The end-to-end inference latency across our evaluations was  $5.66 \pm 1.55$  s, including both the API latency and the model inference time. Overall, these results demonstrate that the combination of semantic 3D mapping and binary visual Q&A can enable more robust scene understanding and reasoning.

### 4.3 Navigation Module Evaluation

We conduct experiments to thoroughly evaluate the navigation module. Specifically, two studies are conducted. The first, evaluates the ability of the navigation module to navigate to a waypoint without the presence of a guiding path from the planning module. In the second, the ability of the navigation module to handle the sudden appearance of unmapped obstacles in the planned path is studied. The aim of these experiments is to a) evaluate the performance of the navigation module in the SDF-NMPC + C-CBF, ExRL + C-CBF, and unsafe controller + C-CBF (where applicable) configurations, b) contrast the behaviors of these collision avoidance methods, and c) evaluate the benefits of the multi-layered safety approach. In all these missions, the AR-2 platform was used, with the SLAM module running the graph optimization online after

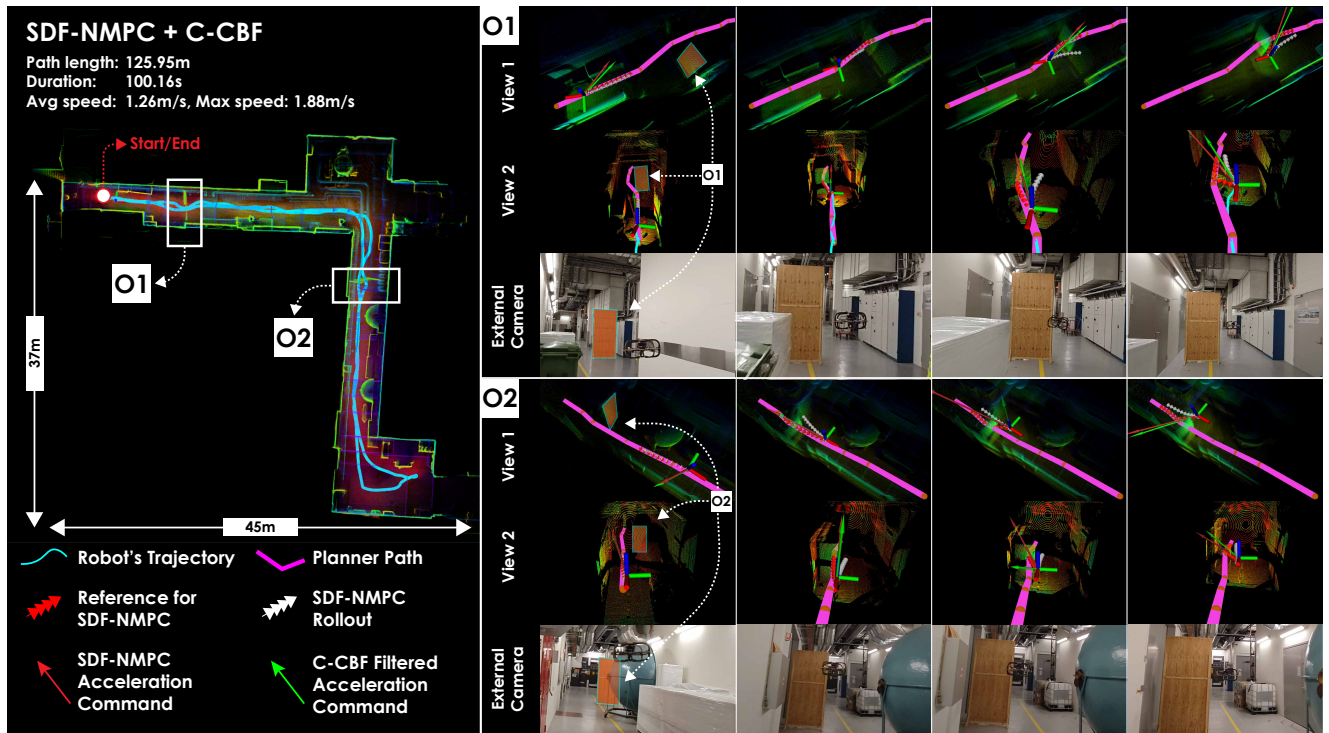


**Figure 14.** Navigation module evaluation is performed in the campus using AR-2 with SDF-NMPC + C-CBF. The robot was tasked to explore the basement autonomously and return home. At two instances, an obstacle was moved into the robot's planned path during the exploration and the return phases respectively, forcing the SDF-NMPC + C-CBF to avoid these previously-absent obstacles in the robot's path. The two specific instances in the mission are highlighted to demonstrate reactive collision-avoidance. The full map is shown alongside the specific instances, with the regions of the specific obstacles highlighted.

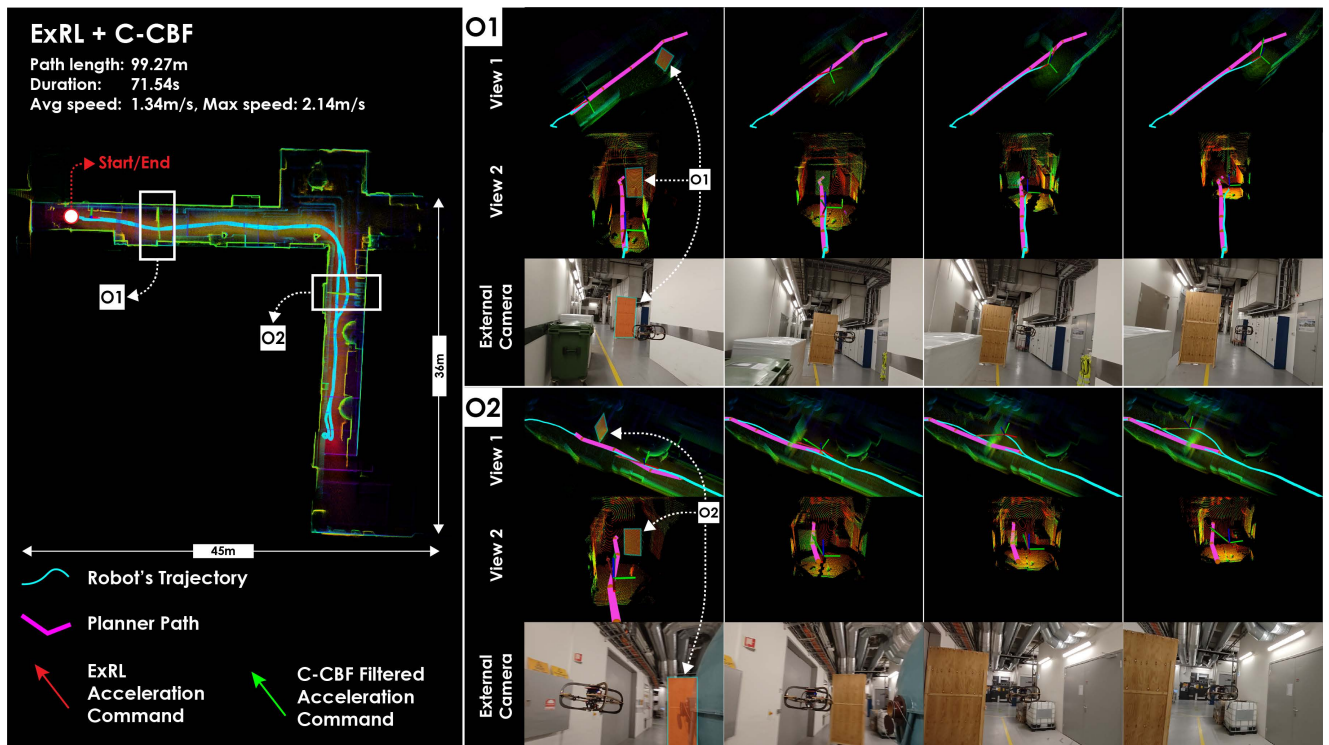


**Figure 15.** Navigation module evaluation is performed in the campus using AR-2 with ExRL + C-CBF. The robot was tasked to explore the basement autonomously and return home. At two instances, an obstacle was moved into the robot's planned path during the exploration and the return phases respectively, forcing the ExRL + C-CBF to avoid these previously-absent obstacles in the robot's path. The two specific instances in the mission are highlighted to demonstrate reactive collision-avoidance. The full map is shown alongside the specific instances, with the regions of the specific obstacles highlighted.

receiving each exteroceptive measurement, considering radar measurements at 10 Hz and LiDAR measurements at 10 Hz. In each experiment (including the evaluations in Section 4.4)

the SDF-NMPC runs at 40 Hz, ExRL at 30 Hz, and C-CBF runs at 50 Hz. The last received exteroceptive sensor measurements and state estimates are used to populate the state

and inputs for each method while it executes at the desired frequency.

**Navigation to Waypoint** The first evaluation studies the ability of the navigation module to navigate to a waypoint without a guiding path from the map-based planning module. The study is conducted in a forest environment. Three experiments are conducted in which the collision avoidance methods used are SDF-NMPC + C-CBF, ExRL + C-CBF, and an unsafe policy (SDF-NMPC but with its collision-avoidance constraints disabled) + C-CBF. In each experiment, the robot starts from the same location, and the same waypoint is given to the navigation module. The results of the study are shown in Figure 13. Both configurations, SDF-NMPC + C-CBF and ExRL + C-CBF, are able to reach the waypoint, avoiding the obstacles. The collision avoidance is predominantly carried out by the SDF-NMPC or ExRL, with the C-CBF intervening only in a few instances (Figures 13.1.3, 13.2.1, and 13.2.2). Engagement of the C-CBF is not a proof that SDF-NMPC or ExRL would necessarily lead to a collision but indicates that the tuning of this last-resort method was such that it triggers it to adjust the reference commands. In turn, close evaluation of the few instances when C-CBF was engaged in these experiments indicates that the robot centroid was on average 0.65 m from the obstacles (which given the robot dimensions, entails less than 0.5 m clearance). On the other hand, the combination of the unsafe version of SDF-NMPC with the C-CBF (which then becomes the only obstacle-avoidance mechanism) is not able to reach the goal and gets stuck, but remains safe at all times. As the C-CBF only aims to remain in the safe set, navigating to the goal is not per se an objective for this method. It is noted that the third configuration (unsafe controller + C-CBF) is not a recommended configuration of the UAS<sub>stack</sub> and is only evaluated to present the different roles of the navigation layers.

Qualitatively, this study further shows the clear difference in the robot's behavior when using SDF-NMPC vs ExRL. The SDF-NMPC follows the straight line from the start to the goal more closely, while the ExRL policy deviates significantly. On the other hand, the ExRL achieves higher speeds throughout the trajectory than SDF-NMPC. Due to this, the resulting mission time for both is comparable. Hence, the selection between SDF-NMPC and ExRL depends on the requirements of the task. The different behaviors manifested between SDF-NMPC and ExRL is among the reasons why the release of the UAS<sub>stack</sub> contains both methods.

**Moving Obstacles** The second study conducted to evaluate the navigation module aims to evaluate its performance in the presence of obstacles appearing in the planned path. Specifically, the following scenario was constructed. The robot was tasked to explore a section of a university building at NTNU. In two separate instances, after the planning module plans a path based on the online map, an obstacle is placed to block this path. The planner is not re-triggered and thus the reference path shall be in collision. The ability of the navigation module to handle this scenario is tested. Two experiments are conducted with the configurations SDF-NMPC + C-CBF and ExRL + C-CBF. Figures 14 and 15 show the result of the

respective experiments. As can be seen, both policies are able to successfully avoid the unseen obstacle. The figures also show that the SDF-NMPC tends to avoid the obstacle with less, yet sufficiently safe, clearance as compared to ExRL as its formulation requires it to have minimal deviation from the reference path. ExRL does not have this constraint and only aims to reach the end of the planned path safely.

#### 4.4 Evaluation of the Full Stack

The full UAS<sub>stack</sub> is evaluated using both aerial and ground robots. When evaluating the full stack, we examine the result of the coordinated interaction between the perception, planning and navigation modules. The perception module is the foundation of the demonstrated autonomy, the planning module drives the behaviors manifested by the robots, while the navigation module provides control and reinforces safety for the autonomous systems. Specifically, the Exploration and Inspection objectives are tested with the Planning to Target being implicitly evaluated through these. Additional insights regarding the Planning to Target behavior can be found in Zacharia et al. (2026). Similarly to Section 4.3 the SLAM module graph optimization is calculated online, with update rate matching what was previously described.

##### 4.4.1 Evaluations with an Aerial Robot

We evaluate the UAS<sub>stack</sub> on the AR-2 in three distinct environments namely a) an underground mine, b) a forest, and c) a ship cargo hold.

**Underground Mine** The first experiment is conducted in a section of the Løkken mine in Norway. We demonstrate results both when otherwise using the SDF-NMPC and ExRL. The selected section of the mine is a 3-way intersection with the robot starting at one end of the narrowest branch (1.5 m wide). The mine has low lighting conditions, and due to the dome FoV, the LiDAR data can quickly become degenerate in narrow branches if the sensor is facing a wall. In both missions, the robot explored the first branch it started in, continued to one of the other branches, repositioned to the next upon exploring it, before finally returning to the start location when the allotted area was fully explored. The robot successfully explored the environment while remaining safe at all times. Figures 16 and 17 show the maps and planning instances in the missions corresponding to SDF-NMPC and ExRL respectively. As the environment topology does not allow much deviation from the planned path, the total path length in both missions is comparable, however, the ExRL policy finishes faster reaching higher speeds. It was observed that at some instances in the narrowest part near the starting area (marked as Start/End in the figures), the SDF-NMPC/ExRL and the C-CBF objectives are competing resulting in transient oscillations. The SDF-NMPC/ExRL are tasked to both make progress along the planned path and maintain safety, while the C-CBF only aims for robot safety thus leading to competing actions in situations that have tight safety margins as here. Nevertheless, the system was always able to continue and this behavior was short-lived.

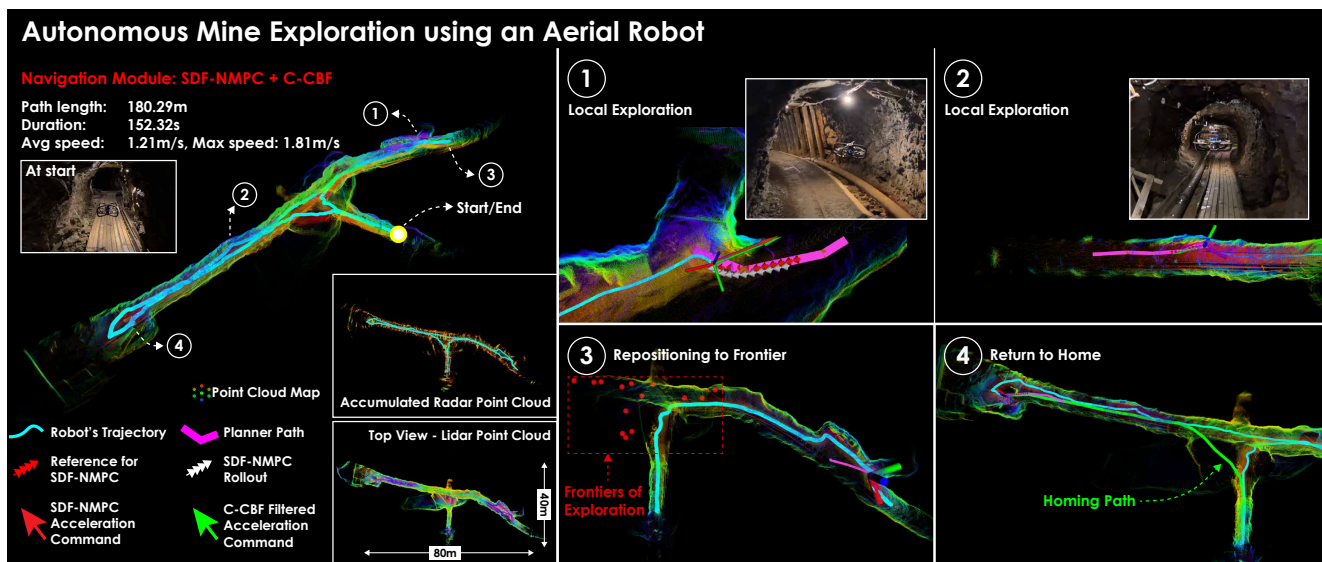


**Figure 16.** Full-stack evaluation in a multi-branched section of an underground mine using AR-2 with SDF-NMPC as the navigation method. The robot started in one branch and explored all three branches, repositioning when needed. The SDF-NMPC tracks the planned path closely, resulting in next to zero interventions from the SDF-NMPC or C-CBF. The figure shows the full map of the environment along with key instances in the mission. Additionally, the mission statistics are shown at the top.

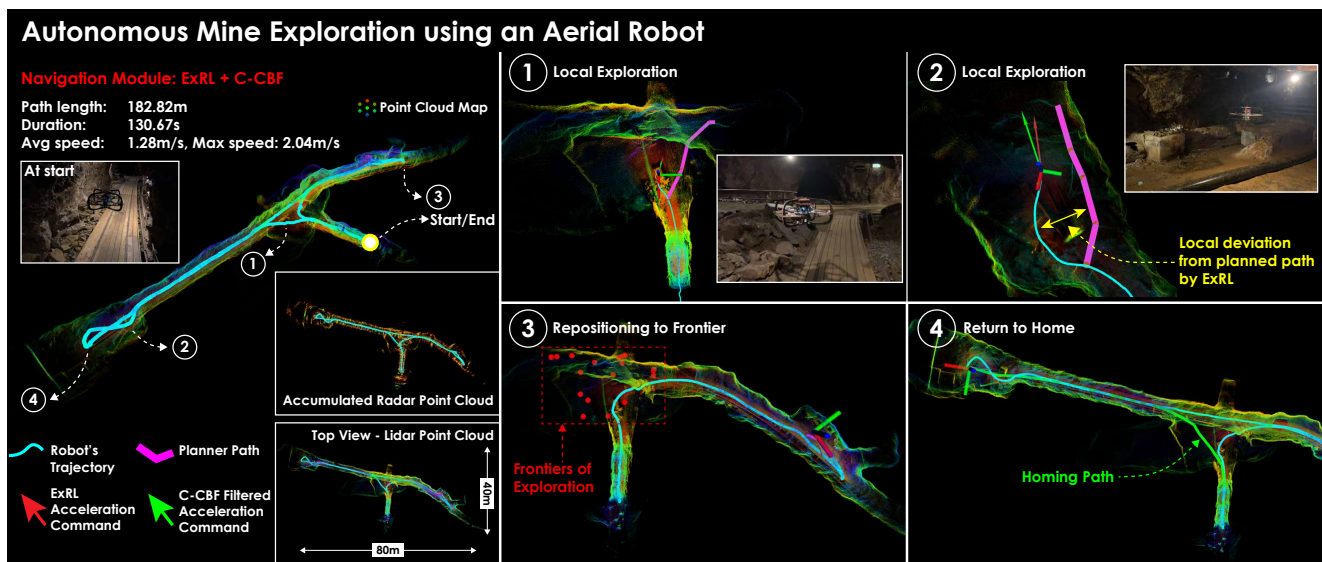


**Figure 17.** Full-stack evaluation in a multi-branched section of an underground mine using AR-2 with ExRL as the navigation method. The robot started in one branch and explored all three branches, repositioning when needed. The ExRL policy only aims to reach the end of each planned path, presenting larger local deviations, but remaining safe at all times. The figure shows the full map of the environment along with key instances in the mission. Additionally, the mission statistics are shown at the top.

*Forest* The AR-2 was deployed in a forest in Trondheim, Norway to explore an area of  $120 \times 80$  m with height limited to 2.5 m. The forest area contains trees at varying densities with thin branches and foliage in some places. The ground was covered in snow at the time of testing. In this test, two missions were conducted, one each with the SDF-NMPC and the ExRL as the core navigation policy feeding into the C-CBF. Figures 18 and 19 show the results for the respective missions. In both missions, the robot started at the same location with identical mission and robot parameters. The robot first performed exploration of the given space and returned back to the start location. As can be seen from Figures 18 and 19, the SDF-NMPC is designed to follow the path given by the planning module more accurately than ExRL. Hence, the robot can take longer trajectories to reach the end of the same path when ExRL is used as

compared to SDF-NMPC. However, as shown by the average and max speed, the ExRL policy generates smoother and faster trajectories than SDF-NMPC (partially as a result of the non-smooth paths given by the planning module), thus resulting in similar mission times. It is thus a decision point for the user of the UASTack to select among these two core navigation policies with the SDF-NMPC being a very reasonable choice when following the planner plans closely is desired, while ExRL is particularly relevant when a more loose tracking of these references combined with agile maneuvering is preferred. Figures 18 and 19 show the full map and planning instances from the respective missions, along with the robot in the environment. In both missions, the robot was successfully able to explore the allotted area, avoiding collisions even in the presence of thin obstacles due to the multi-layered safety. Figures 18.2.1-18.2.4 show

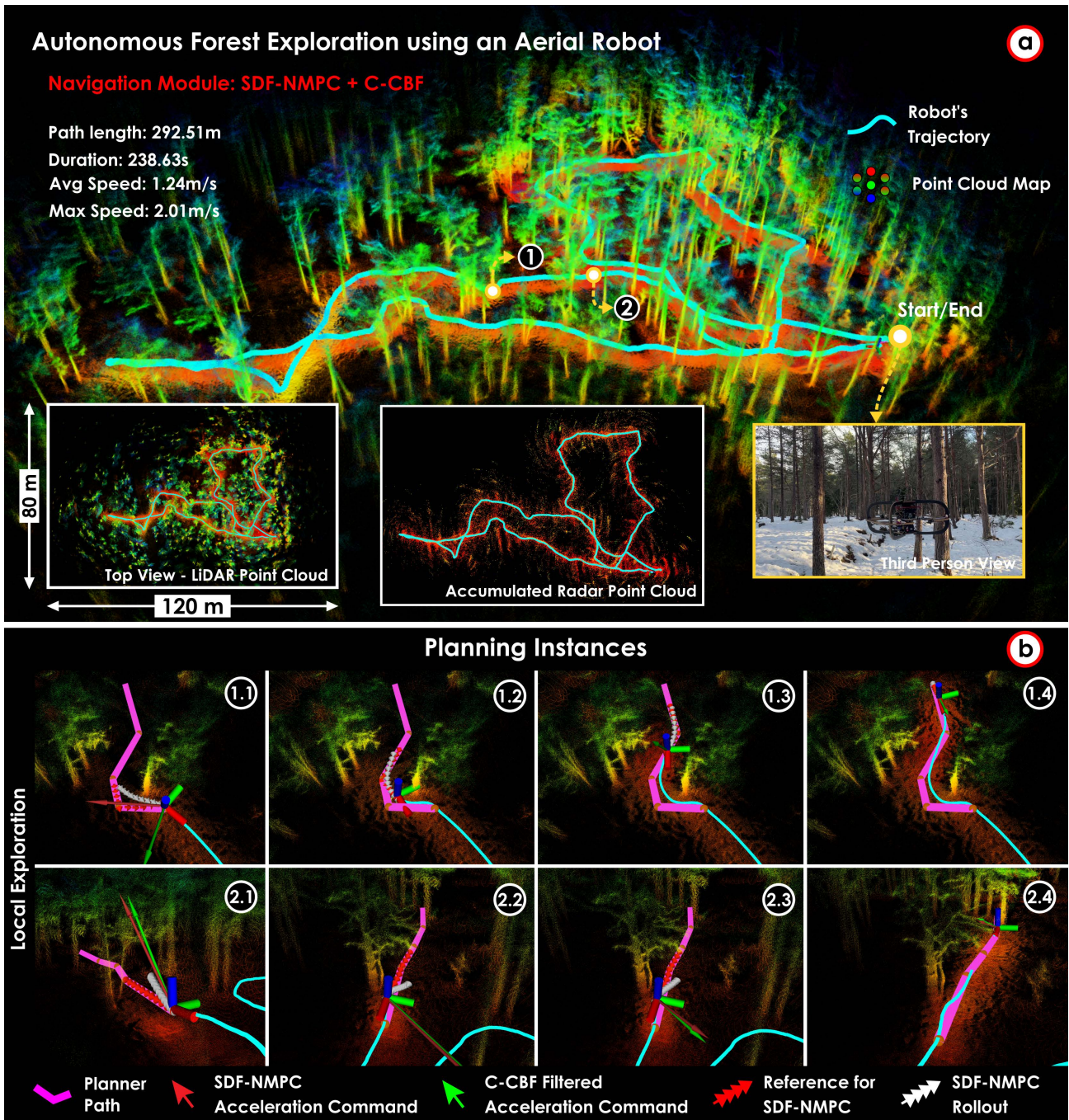


**Figure 18.** Full-stack evaluation in the forest using AR-2 with SDF-NMPC as the navigation method. The robot was tasked to explore a given area autonomously and return home. The figure shows the full map and planning instances in the mission. As the SDF-NMPC follows the planned path closely, it needs to intervene infrequently.

one such instance where the SDF-NMPC deviates from the path planned by the planning module. Similarly, the ExRL policy successfully guides the robot to the end of the path. At one instance in the mission, shown in Figure 19.1.2, the C-CBF can be seen intervening and correcting the command of the ExRL policy as the robot passes through a narrow opening, thus highlighting the importance of the multi-layered safety approach. As when the navigation module was evaluated separately, it is worth mentioning that when the C-CBF was engaged the distance of the robot centroid from the obstacles was 0.68 m and the component of the velocity towards the obstacle was 1.10 m/s. Although the engagement of the C-CBF does not strictly imply that the core method would lead to a collision, it indicates the role

of such a last-resort safety method to assure what proximity and maneuvering towards the obstacles is considered as acceptable.

*Ship Cargo Hold* In the third experiment, the AR-2 was deployed in a cargo hold of an oil tanker ship. In contrast to the previous missions, here the inspection behavior of the planning module is engaged. The dimensions of the cargo hold were  $16 \times 13 \times 15$  m, however, the mission height was limited to 3 m for safety considerations. The robot was tasked to explore the cargo hold and inspect the mapped surfaces. The robot started inside the cargo hold with no prior knowledge, performed exploration, and upon completion switched to the inspection behavior. The complete map and instances of the mission along with an

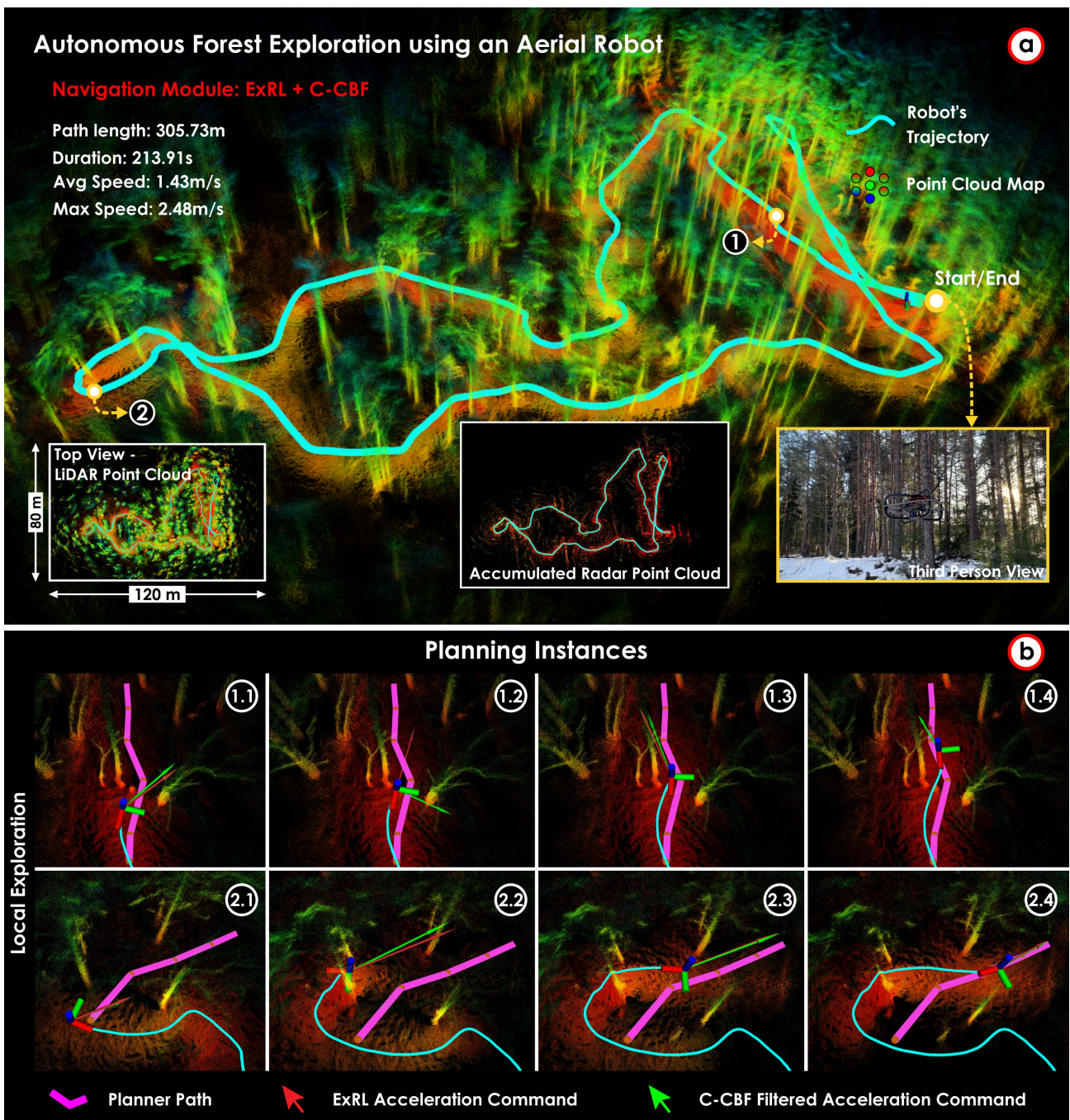


**Figure 19.** Full-stack evaluation in the forest using AR-2 with ExRL as the navigation method. The robot was tasked to explore a given area autonomously and return home. The figure shows the full map and planning instances in the mission. As can be seen, the ExRL is not formulated to follow the planned path strictly, but successfully navigates towards the end of the path, avoiding obstacles.

image of the robot in the environment is shown in Figure 20. As an exception, it is noted that in this experiment the safety policies in the navigation module were disabled as (a) the environment is not demanding in terms of collision avoidance (one large room with no obstacles inside), and (b) this allows the robot to more flexibly travel outside the depth sensor's FoV in the inspection phase.

Through these experiments, we demonstrate the importance and the role of the three layers of safety namely a) map-based collision-avoidance, b) depth-driven SDF-NMPC or ExRL policies, and c) the last resort C-CBF. The map-based safety allows longer horizon planning enabling more complex behavior, and is the safety layer doing the majority

of the collision-avoidance throughout the missions. The depth-driven navigation policies add an additional safeguard against challenges to map-based safety as documented in this work. Finally, the C-CBF provides formal safety guarantees ensuring that the robot remains safe at all times.

#### 4.4.2 Legged

To demonstrate the performance of the UStack on ground robots, we deployed GR-1 in two distinct settings a) in an underground mine, and b) inside a university building at NTNU.

*Underground Mine* In the first mission, GR-1 was deployed in another section of the Løkken mine. This section

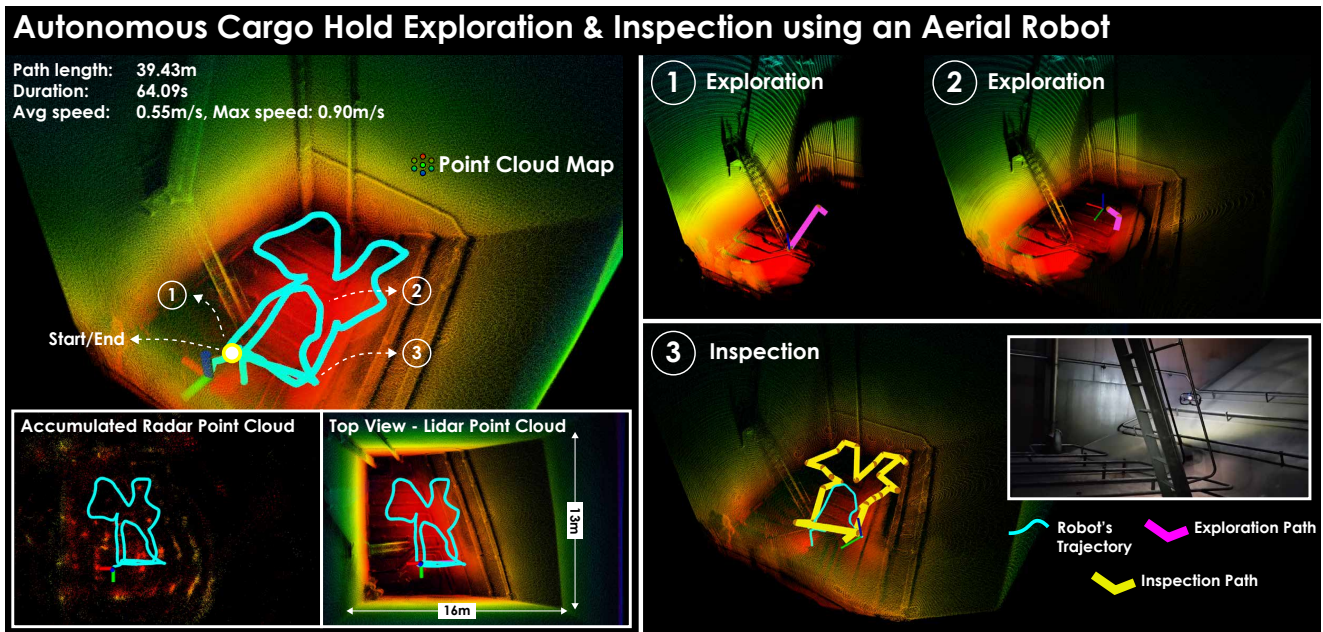


**Figure 20.** Deployment of AR-2 in the ship cargo hold. The robot started with no prior information of the environment. It first performed exploration to map the tank. Upon completion, it switched to the inspection behavior, where it viewed the mapped surfaces with the camera sensor at the desired viewing distance.

consisted of one mine shaft having narrow passages and areas with gaps on the side, requiring careful planning and locomotion. Figure 21 shows the map and planning instances of the mission. Using the dual map representation (volumetric and elevation map), the UAstack is able to successfully complete the mission. It is noted that here the additional safety layers of the navigation module are not utilized as the commercial ANYmal robot already provides the partially analogous feature of “perceptive locomotion” fusing short-range depth from its all-around depth cameras for traversability-aware near-term navigation.

**University Building** The second mission was conducted inside a building at NTNU. The building consists of two sections a) a large open hall with side offshoots, and b) a section with a network of narrow (width  $<1.5$  m) corridors, as can be seen in Figure 22. The robot started in the open hall, and explored it along with the offshoots. Upon completion, the robot repositioned towards the narrow corridor section, explored those, and returned to the start location. This environment presents several challenges to the entire stack, including a) large scale, b) branching corridors, and c) varying environment size. However, the multi-modal SLAM solution provided resilient odometry and consistent maps throughout the mission, as well as the bifurcated architecture of the planning module with traversability-aware planning (exploiting both the volumetric and the elevation maps) lead to successful mission completion.

## 5 Conclusion & Future Work

The UAstack is openly released with the aim of serving as a foundation for a common autonomy blueprint across diverse robot configurations operating in the air, on land, and at sea. Currently, the UAstack supports a wide variety of aerial and ground robot morphologies and enables resilient GNSS-denied, perceptually-degraded localization, mapping, and scene reasoning within target reach, exploration and

inspection missions with a key focus on assured safety through multi-layered navigation. Extensive field evaluation results, alongside openly released datasets, allow for its comprehensive evaluation.

We seek to collaborate with the research community towards enhancing the reliability and resilient performance of the stack, alongside its extension to different robot morphologies and the incorporation of new behaviors. Future development plans specifically include (a) the support of further morphologies, including highly non-holonomic platforms such as fixed-wing uncrewed aerial vehicles, (b) increased emphasis on navigation within dynamic environments, (c) development of further object-centric behaviors, especially guided by natural language, (d) the fusion of additional modalities and specifically infrared vision, (e) improving the vision fusion into MIMOSA-X to be more tightly coupled analogous to what is already done for LiDAR and radar, (f) enhancing the ExRL toward improved long-horizon capabilities, and (g) extend multi-layered safety with traversability-aware reactive modules for ground systems.

Last but not least, we aim to document how lessons learned from the deployment of the stack can lead to certain improvements and adaptations. This currently includes investigations for (a) how to best handle the trade-off between C-CBF and the exteroceptive SDF-NMPC and ExRL methods, (b) computationally-efficient ways to directly fuse vision features in the SLAM solution of the UAstack, alongside (c) refining the rewards of ExRL to better balance between the ability of the method to negotiate complex environments, and how energetically-efficient the trajectories are.

## Acknowledgements

We would like to acknowledge Statens Vegvesen for enabling us to perform tests in Runehamar, Vestland Fylkeskommune for allowing us to perform experiments in the Fyllingsdal sykkel tunnel,

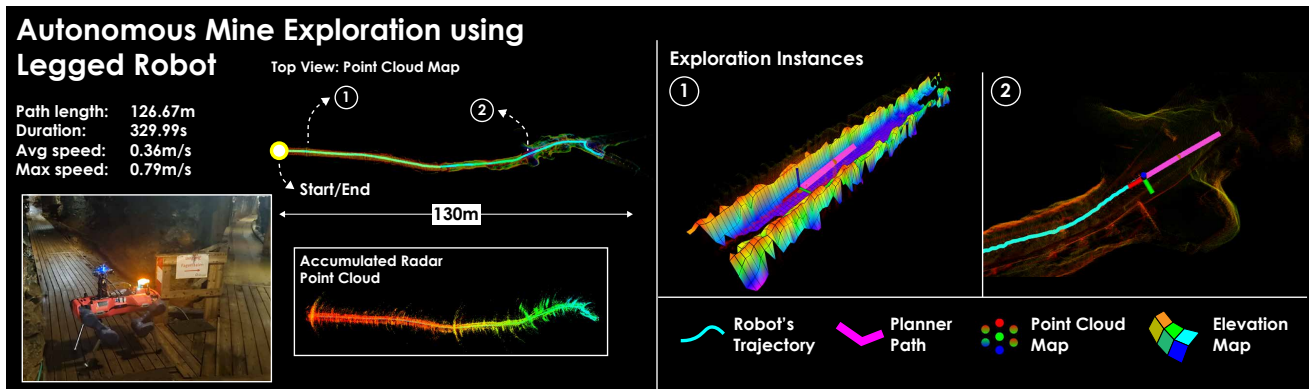


**Figure 21.** Full-stack evaluation in the Løkken underground mine using the GR-1 legged robot. The mission was conducted in one of the mine shafts, presenting narrow cross-section at times, and gaps on the side. Due to the dual map representation (volumetric and elevation maps), the robot was successfully able to handle these challenges completing the mission.

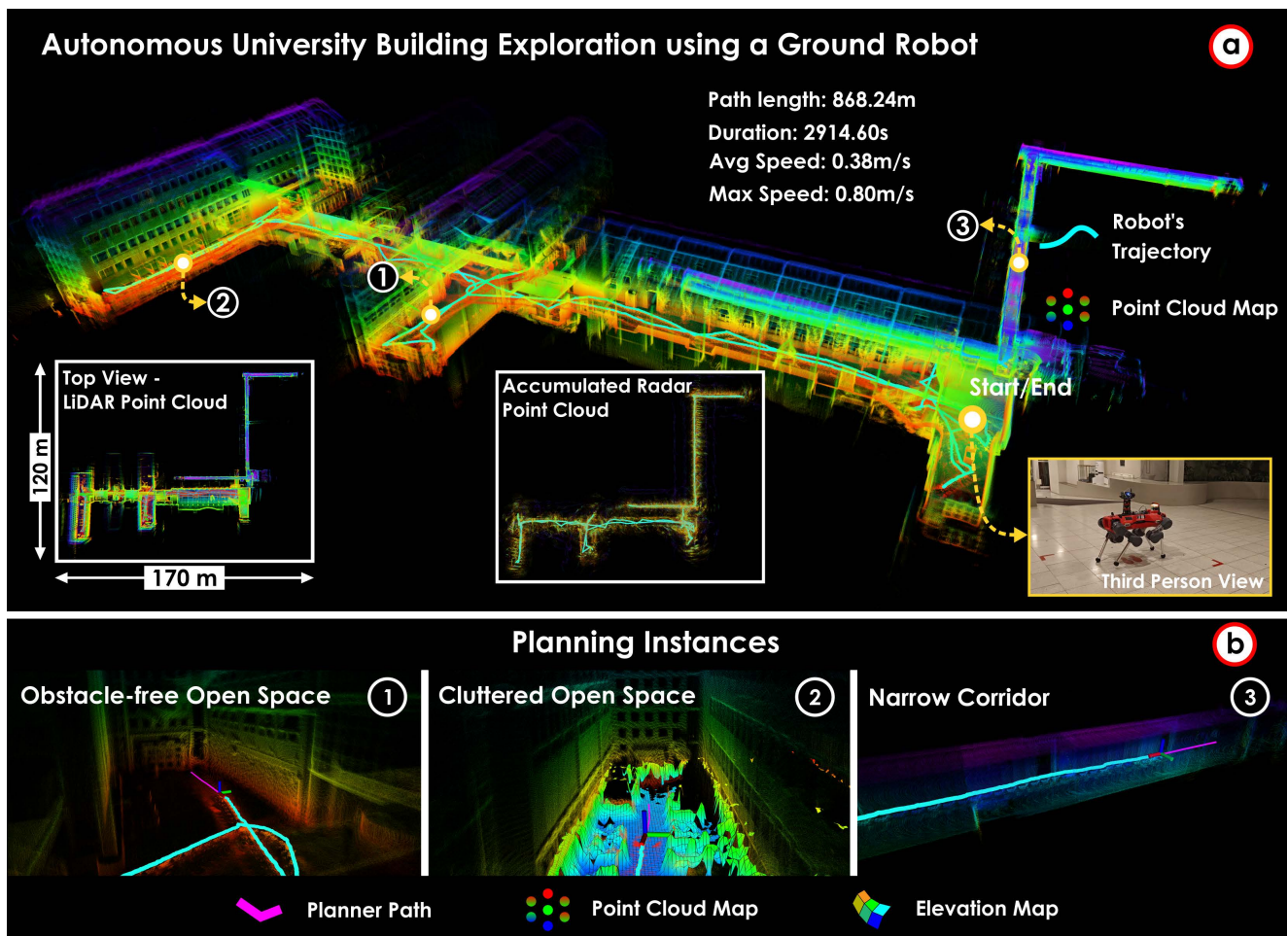


**Figure 22.** Full-stack evaluation was conducted in a university building using the GR-1 legged robot. The robot was tasked with exploring the entire ground floor, which featured both open spaces and narrow corridors. The figure shows the complete map along with the planning instances from the mission.

Leica Geosystems for providing the Robot Operating System (ROS) compatible MS60 and AP20 setup for collection of ground truth, as well as Orkla Industrimuseum for facilitating the tests in the Løkken Mine.

### Author contributions

- Mihir Dharmadhikari: Contributed in the formulation of the idea, the UAstack architecture, and all the evaluations. Furthermore, he is the core developer of the planning module.

- Nikhil Khedekar: Contributed in the formulation of the idea, the UAstack architecture, and all the evaluations. Furthermore, he is a core developer of the multi-modal SLAM, specifically the LiDAR and Vision modalities.
- Mihir Kulkarni: Contributed in the formulation of the idea, the UAstack architecture, and all the evaluations. Furthermore, he is the core developer of Exteroceptive Deep RL navigation policy.

- Morten Nissov: Contributed in the formulation of the idea, the UAstack architecture, and all the evaluations. Furthermore, he is a core developer of the multi-modal SLAM, specifically the Radar modality.
- Martin Jacquet: He is the core developer of the Neural SDF-NMPC and co-developer of the Composite CBF-based Safety Filter, and contributed towards their integration in the UAstack.
- Angelos Zacharia: He is the co-developer of the planning module. He contributed towards its integration in the UAstack and the legged robot experiments.
- Marvin Harms: He is the core developer of the Composite CBF-based Safety Filter. He contributed towards its integration in the UAstack and the evaluations of the safety policies.
- Albert Gassol Puigjaner: He is the core developer of the VLM-based reasoning part of the UAstack and contributed towards its integration in the UAstack.
- Philipp Weiss: Contributed towards the development of the hardware setup and conducting the field experiments.
- Kostas Alexis: Contributed in the formulation of the idea, the UAstack architecture, and planning for all evaluations. Furthermore, he contributed to the planning, problem formulation, and algorithmic approach of each module in the UAstack.

All authors contributed to the writing of this manuscript.

## Statements and declarations

### Ethical considerations

This article does not contain any studies with human or animal participants.

### Consent to participate

Not applicable.

### Consent for publication

Not applicable.

### Declaration of conflicting interests

The author(s) declared no potential conflicts of interest with respect to the research, authorship, and/or publication of this article.

### Funding

The author(s) disclosed receipt of the following financial support for the research, authorship, and/or publication of this article: This work was supported by European Commission Horizon Europe grant agreements a) SPEAR (EC 101119774), b) DIGIFOREST (EC 101070405), c) SYNERGISE (EC 101121321), and d) AUTOASSESS (EC 101120732).

## References

- Agha A, Otsu K, Morrell B, Fan DD, Thakker R, Santamaria-Navarro A, Kim SK, Bouman A, Lei X, Edlund J et al. (2021) Nebula: Quest for robotic autonomy in challenging environments; team costar at the darpa subterranean challenge. *arXiv preprint arXiv:2103.11470*.
- AirLab C (2025) Airstack. <https://github.com/castacks/AirStack>. Accessed: 2025-02-04.
- Alan A, Taylor AJ, He CR, Ames AD and Orosz G (2023) Control barrier functions and input-to-state safety with application to automated vehicles. *IEEE Transactions on Control Systems Technology* 31(6): 2744–2759. DOI:10.1109/TCST.2023.3286090.
- Andersson J, Gillis J, Horn G, Rawlings J and Diehl M (2018) Casadi—a software framework for nonlinear optimization and optimal control. *Mathematical Programming Computation* 11(1): 1–36.
- ArduPilot Dev Team (2024) Ardupilot documentation. URL <https://ardupilot.org/ardupilot/>. Accessed: 2026-03-26.
- Auto A (2017) apollo. URL <https://github.com/ApolloAuto/apollo>. Accessed 2026-04-09.
- Autoware Foundation T (2021) autoware\_universe. URL [https://github.com/autowarefoundation/autoware\\_universe](https://github.com/autowarefoundation/autoware_universe). Accessed 2026-04-09.
- Baca T, Petrlik M, Vrba M, Spurny V, Penicka R, Hert D and Saska M (2021) The mrs uav system: Pushing the frontiers of reproducible research, real-world deployment, and education with autonomous unmanned aerial vehicles. *Journal of Intelligent & Robotic Systems* 102(1): 26.
- Bloesch M, Burri M, Omari S, Hutter M and Siegwart R (2017) Iterated extended kalman filter based visual-inertial odometry using direct photometric feedback. *The International Journal of Robotics Research* 36(10): 1053–1072. DOI:10.1177/0278364917728574.
- Campos C, Elvira R, Rodríguez JJG, M Montiel JM and D Tardós J (2021) Orb-slam3: An accurate open-source library for visual, visual–inertial, and multimap slam. *IEEE Transactions on Robotics* 37(6): 1874–1890. DOI:10.1109/TRO.2021.3075644.
- Carrillo H, Reid I and Castellanos JA (2012) On the comparison of uncertainty criteria for active slam. In: *2012 IEEE International Conference on Robotics and Automation*. pp. 2080–2087. DOI:10.1109/ICRA.2012.6224890.
- Chang Y, Ebadi K, Denniston CE, Ginting MF, Rosinol A, Reinke A, Palieri M, Shi J, Chatterjee A, Morrell B et al. (2022) Lamp 2.0: A robust multi-robot slam system for operation in challenging large-scale underground environments. *IEEE Robotics and Automation Letters* 7(4): 9175–9182.
- Chung TH, Orekhov V and Maio A (2023) Into the robotic depths: Analysis and insights from the darpa subterranean challenge. *Annual Review of Control, Robotics, and Autonomous Systems* 6(1): 477–502.
- Datar A, Pokhrel A, Nazeri M, Rao MB, Rangwala H, Pan C, Zhang Y, Harrison A, Wigness M, Osteen PR et al. (2025) M2p2: A multi-modal passive perception dataset for off-road mobility in extreme low-light conditions. In: *2025 IEEE/RSJ International Conference on Intelligent Robots and Systems (IROS)*. IEEE, pp. 13690–13696.
- Dellaert F and GTSAM Contributors (2022) borglab/gtsam. DOI: 10.5281/zenodo.5794541. URL <https://github.com/borglab/gtsam>.
- Dharmadhikari M and Alexis K (2025) Semantics-aware predictive inspection path planning. *IEEE Transactions on Field Robotics*.

- Ebadi K, Bernreiter L, Biggie H, Catt G, Chang Y, Chatterjee A, Denniston CE, Deschênes SP, Harlow K, Khattak S et al. (2023) Present and future of slam in extreme environments: The darpa sub challenge. *IEEE Transactions on Robotics* 40: 936–959.
- Fankhauser P, Bloesch M, Gehring C, Hutter M and Siegwart R (2014) Robot-centric elevation mapping with uncertainty estimates. In: *International Conference on Climbing and Walking Robots (CLAWAR)*.
- Fankhauser P, Bloesch M and Hutter M (2018) Probabilistic terrain mapping for mobile robots with uncertain localization. *IEEE Robotics and Automation Letters* 3(4): 3019–3026. DOI: 10.1109/LRA.2018.2849506.
- Farrell J (2008) *Aided Navigation: GPS with High Rate Sensors*. 1 edition. USA: McGraw-Hill, Inc. ISBN 0071493298.
- Fernandez-Cortizas M, Molina M, Arias-Perez P, Perez-Segui R, Perez-Saura D and Campoy P (2023) Aerostack2: A software framework for developing multi-robot aerial systems. *arXiv preprint arXiv:2303.18237*.
- Foehn P, Kaufmann E, Romero A, Penicka R, Sun S, Bauersfeld L, Laengle T, Cioffi G, Song Y, Loquercio A et al. (2022) Agilicious: Open-source and open-hardware agile quadrotor for vision-based flight. *Science robotics* 7(67): eabl6259.
- Forster C, Carlone L, Dellaert F and Scaramuzza D (2017) On-manifold preintegration for real-time visual–inertial odometry. *IEEE Transactions on Robotics* 33(1): 1–21. DOI:10.1109/TRO.2016.2597321.
- Geneva P, Eckenhoff K, Lee W, Yang Y and Huang G (2020a) OpenVINS: A research platform for visual-inertial estimation. In: *Proc. of the IEEE International Conference on Robotics and Automation*. Paris, France.
- Geneva P, Eckenhoff K, Lee W, Yang Y and Huang G (2020b) Openvins: A research platform for visual-inertial estimation. In: *2020 IEEE International Conference on Robotics and Automation (ICRA)*. pp. 4666–4672. DOI:10.1109/ICRA40945.2020.9196524.
- Gifftaler M, Neunert M, Stäubli M and Buchli J (2018) The control toolbox—an open-source c++ library for robotics, optimal and model predictive control. In: *2018 IEEE international conference on simulation, modeling, and programming for autonomous robots (SIMPAN)*. IEEE, pp. 123–129.
- Goodin C, Moore MN, Carruth DW, Hudson CR, Cagle LD, Wapnick S and Jayakumar P (2024) The nature autonomy stack: an open-source stack for off-road navigation. In: *Unmanned Systems Technology XXVI*, volume 13055. SPIE, pp. 8–17.
- Greff M and Schoellig AP (2018) Flatness-based model predictive control for quadrotor trajectory tracking. In: *2018 IEEE/RSJ International Conference on Intelligent Robots and Systems (IROS)*. pp. 6740–6745. DOI:10.1109/IROS.2018.8594012.
- Grupp M (2017) evo: Python package for the evaluation of odometry and slam. <https://github.com/MichaelGrupp/evo>.
- Harlow K, Jang H, Barfoot TD, Kim A and Heckman C (2024) A new wave in robotics: Survey on recent mmwave radar applications in robotics. *IEEE Transactions on Robotics* 40: 4544–4560. DOI:10.1109/TRO.2024.3463504.
- Harms M, Jacquet M and Alexis K (2025) Safe Quadrotor Navigation Using Composite Control Barrier Functions. In: *2025 IEEE International Conference on Robotics and Automation (ICRA)*. pp. 6343–6349. DOI:10.1109/ICRA55743.2025.11127368. URL <https://ieeexplore.ieee.org/document/11127368>.
- Huber PJ (1964) Robust estimation of a location parameter. *The Annals of Mathematical Statistics* 35(1): 73–101. URL <http://www.jstor.org/stable/2238020>.
- Jacquet M, Harms M and Alexis K (2025) Neural NMPC through Signed Distance Field Encoding for Collision Avoidance. DOI: 10.1177/02783649251401223. URL <http://arxiv.org/abs/2511.21312>. ArXiv:2511.21312 [cs].
- Jung HY, Paek DH and Kong SH (2025) Open-source autonomous driving software platforms: Comparison of autoware and apollo. *arXiv preprint arXiv:2501.18942*.
- Kaess M, Johannsson H, Roberts R, Ila V, Leonard J and Dellaert F (2011) iSAM2: Incremental smoothing and mapping with fluid relinearization and incremental variable reordering. In: *2011 IEEE International Conference on Robotics and Automation*. IEEE, pp. 3281–3288. DOI:10.1109/icra.2011.5979641.
- Kamel M, Stastny T, Alexis K and Siegwart R (2017) Model Predictive Control for Trajectory Tracking of Unmanned Aerial Vehicles Using Robot Operating System. In: Koubaa A (ed.) *Robot Operating System (ROS)*, volume 707. Cham: Springer International Publishing. ISBN 978-3-319-54926-2 978-3-319-54927-9, pp. 3–39. DOI:10.1007/978-3-319-54927-9\_1. URL [http://link.springer.com/10.1007/978-3-319-54927-9\\_1](http://link.springer.com/10.1007/978-3-319-54927-9_1).
- Kato S, Tokunaga S, Maruyama Y, Maeda S, Hirabayashi M, Kitsukawa Y, Monrroy A, Ando T, Fujii Y and Azumi T (2018) Autoware on board: Enabling autonomous vehicles with embedded systems. In: *2018 ACM/IEEE 9th International Conference on Cyber-Physical Systems (ICCPS)*. IEEE, pp. 287–296.
- Khattak S, Nguyen H, Mascari F, Dang T and Alexis K (2020) Complementary Multi-Modal Sensor Fusion for Resilient Robot Pose Estimation in Subterranean Environments. In: *2020 International Conference on Unmanned Aircraft Systems (ICUAS)*. Athens, Greece: IEEE. ISBN 978-1-72814-278-4, pp. 1024–1029. DOI:10.1109/ICUAS48674.2020.9213865. URL <https://ieeexplore.ieee.org/document/9213865/>.
- Khedekar N and Alexis K (2025) PG-LIO: Photometric-Geometric fusion for Robust LiDAR-Inertial Odometry. DOI:10.48550/arXiv.2506.18583. URL <http://arxiv.org/abs/2506.18583>. ArXiv:2506.18583 [cs].
- Khedekar N, Kulkarni M and Alexis K (2022) MIMOSA: A Multi-Modal SLAM Framework for Resilient Autonomy against Sensor Degradation. In: *2022 IEEE/RSJ International Conference on Intelligent Robots and Systems (IROS)*. Kyoto, Japan: IEEE. ISBN 978-1-66547-927-1, pp. 7153–7159. DOI:10.1109/IROS47612.2022.9981108. URL <https://ieeexplore.ieee.org/document/9981108/>.
- Koenig N and Howard A (2004) Design and use paradigms for gazebo, an open-source multi-robot simulator. In: *IEEE/RSJ International Conference on Intelligent Robots and Systems*. Sendai, Japan, pp. 2149–2154.
- Koide K, Yokozuka M, Oishi S and Banno A (2024) Glim: 3d range-inertial localization and mapping with gpu-accelerated scan matching factors. *Robotics and Autonomous Systems* 179: 104750. DOI:<https://doi.org/10.1016/j.robot.2024.104750>.

- URL <https://www.sciencedirect.com/science/article/pii/S0921889024001349>.
- Kottege N, Williams J, Tidd B, Talbot F, Steindl R, Cox M, Frousheger D, Hines T, Pitt A, Tam B et al. (2024) Heterogeneous robot teams with unified perception and autonomy: How team csiro data61 tied for the top score at the darpa subterranean challenge. *Field Robotics* 4: 313–359.
- Koubâa A, Allouch A, Alajlan M, Javed Y, Belghith A and Khalgui M (2019) Micro air vehicle link (mavlink) in a nutshell: A survey. *IEEE Access* 7: 87658–87680.
- Kulkarni M and Alexis K (2023) Task-Driven Compression for Collision Encoding Based on Depth Images. In: Bebis G, Ghiasi G, Fang Y, Sharf A, Dong Y, Weaver C, Leo Z, LaViola Jr JJ and Kohli L (eds.) *Advances in Visual Computing*. Cham: Springer Nature Switzerland. ISBN 978-3-031-47966-3, pp. 259–273. DOI:10.1007/978-3-031-47966-3\_20.
- Kulkarni M and Alexis K (2024) Reinforcement Learning for Collision-free Flight Exploiting Deep Collision Encoding. In: *2024 IEEE International Conference on Robotics and Automation (ICRA)*. pp. 15781–15788. DOI:10.1109/ICRA57147.2024.10610287. URL <https://ieeexplore.ieee.org/document/10610287>.
- Kulkarni M, Dharmadhikari M, Khedekar N, Nissov M, Singh M, Weiss P and Alexis K (2025a) Unipilot: Enabling gps-denied autonomy across embodiments. *arXiv preprint arXiv:2509.11793*.
- Kulkarni M, Nguyen H and Alexis K (2023) Semantically-enhanced deep collision prediction for autonomous navigation using aerial robots. In: *2023 IEEE/RSJ International Conference on Intelligent Robots and Systems (IROS)*. IEEE, pp. 3056–3063.
- Kulkarni M, Rehberg W and Alexis K (2025b) Aerial Gym Simulator: A Framework for Highly Parallelized Simulation of Aerial Robots. *IEEE Robotics and Automation Letters* 10(4): 4093–4100. DOI:10.1109/LRA.2025.3548507. URL <https://ieeexplore.ieee.org/document/10910148/>.
- Lee T, Leok M and McClamroch NH (2010) Geometric tracking control of a quadrotor UAV on SE(3). In: *49th IEEE Conference on Decision and Control (CDC)*. Atlanta, GA: IEEE. ISBN 978-1-4244-7745-6 978-1-4244-7746-3, pp. 5420–5425. DOI:10.1109/CDC.2010.5717652. URL <http://ieeexplore.ieee.org/document/5717652/>.
- Likhachev M, Gordon GJ and Thrun S (2003) Ara\*: Anytime a\* with provable bounds on sub-optimality. *Advances in neural information processing systems* 16.
- Macenski S, Martín F, White R and Ginés Clavero J (2020) The marathon 2: A navigation system. In: *2020 IEEE/RSJ International Conference on Intelligent Robots and Systems (IROS)*. URL <https://github.com/ros-planning/navigation2>.
- Makoviichuk D and Makoviychuk V (2021) rl-games: A high-performance framework for reinforcement learning. [https://github.com/Denys88/rl\\_games](https://github.com/Denys88/rl_games).
- Meier L, Honegger D and Pollefeys M (2015) Pxl4: A node-based multithreaded open source robotics framework for deeply embedded platforms. In: *2015 IEEE international conference on robotics and automation (ICRA)*. IEEE, pp. 6235–6240.
- Mellinger D and Kumar V (2011) Minimum snap trajectory generation and control for quadrotors. In: *2011 IEEE international conference on robotics and automation*. Ieee, pp. 2520–2525.
- Miki T, Lee J, Hwangbo J, Wellhausen L, Koltun V and Hutter M (2022) Learning robust perceptive locomotion for quadrupedal robots in the wild. *Science Robotics* 7(62): eabk2822. DOI:10.1126/scirobotics.abk2822. URL <https://www.science.org/doi/abs/10.1126/scirobotics.abk2822>.
- Misyats N, Harms M, Nissov M, Jacquet M and Alexis K (2025) Embedded safe reactive navigation for multirotors systems using control barrier functions. In: *2025 International Conference on Unmanned Aircraft Systems (ICUAS)*. IEEE, pp. 697–704.
- Mohta K, Watterson M, Mulgaonkar Y, Liu S, Qu C, Makineni A, Saulnier K, Sun K, Zhu A, Delmerico J, Thakur D, Karydis K, Atanasov N, Loianno G, Scaramuzza D, Daniilidis K, Taylor CJ and Kumar V (2018) Fast, autonomous flight in gps-denied and cluttered environments. *Journal of Field Robotics* 35(1): 101–120.
- Nanayakkara R, Ames AD and Tabuada P (2025) Safety under state uncertainty: Robustifying control barrier functions. URL <https://arxiv.org/abs/2508.17226>.
- NASA CoSTAR (2022) NeBula Autonomy — github.com. <https://github.com/NeBula-Autonomy>. [Accessed 09-04-2026].
- Nemiroff R, Chen K and Lopez BT (2023) Joint on-manifold gravity and accelerometer intrinsics estimation for inertially aligned mapping. In: *2023 IEEE/RSJ International Conference on Intelligent Robots and Systems (IROS)*. pp. 1388–1394. DOI:10.1109/IROS55552.2023.10342424.
- Nissov M, Edlund JA, Spieler P, Padgett C, Alexis K and Khattak S (2024a) Robust high-speed state estimation for off-road navigation using radar velocity factors. *IEEE Robotics and Automation Letters* 9(12): 11146–11153. DOI:10.1109/lra.2024.3486189.
- Nissov M, Khedekar N and Alexis K (2024b) Degradation Resilient LiDAR-Radar-Inertial Odometry. In: *2024 IEEE International Conference on Robotics and Automation (ICRA)*. pp. 8587–8594. DOI:10.1109/ICRA57147.2024.10611444. URL <https://ieeexplore.ieee.org/document/10611444>.
- Nissov M, Khedekar N and Alexis K (2025) Simultaneous triggering and synchronization of sensors and onboard computers. URL <https://arxiv.org/abs/2507.05717>.
- Noh C, Yang W, Jung M, Jung S and Kim A (2025) Garlio: Gravity enhanced radar-lidar-inertial odometry. In: *2025 IEEE International Conference on Robotics and Automation (ICRA)*. pp. 9869–9875. DOI:10.1109/ICRA55743.2025.11128334.
- NVIDIA, :, Mittal M, Roth P, Tigue J, Richard A, Zhang O, Du P, Serrano-Muñoz A, Yao X, Zurbrügg R, Rudin N, Wawrzyniak L, Rakhsha M, Denzler A, Heiden E, Borovicka A, Ahmed O, Akinola I, Anwar A, Carlson MT, Feng JY, Garg A, Gasoto R, Gulich L, Guo Y, Gussert M, Hansen A, Kulkarni M, Li C, Liu W, Makoviychuk V, Malczyk G, Mazhar H, Moghani M, Murali A, Noseworthy M, Poddubny A, Ratliff N, Rehberg W, Schwarke C, Singh R, Smith JL, Tang B, Thaker R, Trepte M, Wyk KV, Yu F, Millane A, Ramasamy V, Steiner R, Subramanian S, Volk C, Chen C, Jawale N, Kuruttukulam AV, Lin MA, Mandlekar A, Patzwaldt K, Welsh J, Zhao H, Anes F, Lafleche JF, Moëne-Loccoz N, Park S, Stepinski R, Gelder DV, Amevor C, Carius J, Chang J, Chen

- AH, de Heras Ciechowski P, Daviet G, Mohajerani M, von Muralt J, Reutsky V, Sauter M, Schirm S, Shi EL, Terdiman P, Vilella K, Widmer T, Yeoman G, Chen T, Grizan S, Li C, Li L, Smith C, Wiltz R, Alexis K, Chang Y, Chu D, Fan LJ, Farshidian F, Handa A, Huang S, Hutter M, Narang Y, Pouya S, Sheng S, Zhu Y, Macklin M, Moravanszky A, Reist P, Guo Y, Hoeller D and State G (2025) Isaac lab: A gpu-accelerated simulation framework for multi-modal robot learning. URL <https://arxiv.org/abs/2511.04831>.
- Oleynikova H, Taylor Z, Fehr M, Siegwart R and Nieto J (2017) Voxblox: Incremental 3d euclidean signed distance fields for on-board mav planning. In: *2017 IEEE/RSJ International Conference on Intelligent Robots and Systems (IROS)*. IEEE, pp. 1366–1373.
- Petrenko A, Huang Z, Kumar T, Sukhatme G and Koltun V (2020) Sample Factory: Egocentric 3D Control from Pixels at 100000 FPS with Asynchronous Reinforcement Learning. *Proceedings of the 37th International Conference on Machine Learning, Online, PMLR 119, 2020*.
- Petris PD, Nguyen H, Dharmadhikari M, Kulkarni M, Khedekar N, Mascarich F and Alexis K (2022) RMF-Owl: A Collision-Tolerant Flying Robot for Autonomous Subterranean Exploration. In: *2022 International Conference on Unmanned Aircraft Systems (ICUAS)*. Dubrovnik, Croatia: IEEE. ISBN 978-1-66540-593-5, pp. 536–543. DOI:10.1109/ICUAS54217.2022.9836115. URL <https://ieeexplore.ieee.org/document/9836115/>.
- Planning R (2012) navigation. URL <https://github.com/ros-planning/navigation>. Accessed 2026-04-09.
- Qian C, Xu Y, Shi X, Chen J and Li L (2025) Af-rlio: Adaptive fusion of radar-lidar-inertial information for robust odometry in challenging environments. In: *2025 IEEE International Conference on Robotics and Automation (ICRA)*. pp. 1–7. DOI: 10.1109/ICRA55743.2025.11128046.
- Qin T, Pan J, Cao S and Shen S (2019) A general optimization-based framework for local odometry estimation with multiple sensors. URL <https://arxiv.org/abs/1901.03638>.
- Ravichandran Z, Cladera F, Hughes J, Murali V, Hsieh MA, Pappas GJ, Taylor CJ and Kumar V (2025) Deploying foundation model-enabled air and ground robots in the field: Challenges and opportunities. *arXiv preprint arXiv:2505.09477*.
- Real F, Torres-González A, Soria PR, Capitán J and Ollero A (2020) Unmanned aerial vehicle abstraction layer: An abstraction layer to operate unmanned aerial vehicles. *International Journal of Advanced Robotic Systems* 17(4): 1–13. DOI:10.1177/1729881420925011. URL <https://doi.org/10.1177/1729881420925011>.
- Sanchez-Lopez JL, Fernández RAS, Bavle H, Sampedro C, Molina M, Pestana J and Campoy P (2016) Aerostack: An architecture and open-source software framework for aerial robotics. In: *2016 International Conference on Unmanned Aircraft Systems (ICUAS)*. IEEE, pp. 332–341.
- Schulman J, Wolski F, Dhariwal P, Radford A and Klimov O (2017) Proximal Policy Optimization Algorithms. URL <http://arxiv.org/abs/1707.06347>.
- Schwarke C, Mittal M, Rudin N, Hoeller D and Hutter M (2025) Rsl-rl: A learning library for robotics research. *arXiv preprint arXiv:2509.10771*.
- Serpiva V, Lykov A, Myshlyaev A, Khan MH, Abdulkarim AA, Sautenkov O and Tsetserukou D (2025) Racevla: Vla-based racing drone navigation with human-like behaviour. *arXiv preprint arXiv:2503.02572*.
- Shan T, Englot B, Meyers D, Wang W, Ratti C and Daniela R (2020) Lio-sam: Tightly-coupled lidar inertial odometry via smoothing and mapping. In: *IEEE/RSJ International Conference on Intelligent Robots and Systems (IROS)*. IEEE, pp. 5135–5142.
- Sucan IA, Moll M and Kavraki LE (2012) The open motion planning library. *IEEE Robotics & Automation Magazine* 19(4): 72–82.
- Tranzatto M, Miki T, Dharmadhikari M, Bernreiter L, Kulkarni M, Mascarich F, Andersson O, Khattak S, Hutter M, Siegwart R et al. (2022) Cerberus in the darpa subterranean challenge. *Science Robotics* 7(66): eabp9742.
- Verschueren R, Frison G, Kouzoupis D, Frey J, Duijkeren Nv, Zanelli A, Novoselnik B, Albin T, Quirynen R and Diehl M (2022) acados—a modular open-source framework for fast embedded optimal control. *Mathematical Programming Computation* 14(1): 147–183.
- Vizzo I, Guadagnino T, Mersch B, Wiesmann L, Behley J and Stachniss C (2023) KISS-ICP: In Defense of Point-to-Point ICP – Simple, Accurate, and Robust Registration If Done the Right Way. *IEEE Robotics and Automation Letters (RA-L)* 8(2): 1029–1036. DOI:10.1109/LRA.2023.3236571.
- Wang A, Liu L, Chen H, Lin Z, Han J and Ding G (2025) Yoloe: Real-time seeing anything. In: *Proceedings of the IEEE/CVF International Conference on Computer Vision (ICCV)*. pp. 24591–24602.
- Wang Z, Zhou X, Xu C and Gao F (2022) Geometrically constrained trajectory optimization for multicopters. *IEEE Transactions on Robotics* 38(5): 3259–3278.
- Wu Y, Zhu M, Li X, Du Y, Fan Y, Li W, Han Z, Zhou X and Gao F (2025) Vla-an: An efficient and onboard vision-language-action framework for aerial navigation in complex environments. *arXiv preprint arXiv:2512.15258*.
- Xu P, Deng Z, Deng J, Gu Z and Wan S (2026) Aerialvla: A vision-language-action model for uav navigation via minimalist end-to-end control. *arXiv preprint arXiv:2603.14363*.
- Xu W, Cai Y, He D, Lin J and Zhang F (2022) Fast-lio2: Fast direct lidar-inertial odometry. *IEEE Transactions on Robotics* 38(4): 2053–2073. DOI:10.1109/TRO.2022.3141876.
- Zacharia A, Dharmadhikari M, Singh M and Alexis K (2026) Omniplanner: Universal exploration and inspection path planning across robot morphologies. URL <https://arxiv.org/abs/2603.04284>.
- Zakka K, Tabanpour B, Liao Q, Haiderbhai M, Holt S, Luo JY, Allshire A, Frey E, Sreenath K, Kahrs LA, Sferrazza C, Tassa Y and Abbeel P (2025) Mujoco playground: An open-source framework for gpu-accelerated robot learning and sim-to-real transfer. URL [https://github.com/google-deeppmind/mujoco\\_playground](https://github.com/google-deeppmind/mujoco_playground).
- Zhang Q, Zheng S, Sun J, Li C, Wu X, Song Z, Cui Z, Lv Y and Tian Y (2026) Uav-track vla: Embodied aerial tracking via vision-language-action models. *arXiv preprint arXiv:2604.02241*.
- Zheng C, Xu W, Zou Z, Hua T, Yuan C, He D, Zhou B, Liu Z, Lin J, Zhu F, Ren Y, Wang R, Meng F and Zhang F (2025) Fast-lio2: Fast, direct lidar-inertial-visual odometry. *IEEE Transactions on Robotics* 41: 326–346. DOI:10.1109/TRO.2024.3502198.

## A Index to multimedia Extensions

Ext.	Media type	Description
1	Video	Filename: 00_unified_autonomy_stack_main_video.mp4. This video provides an overview of this paper including a) the UAstack architecture, b) the details of each core modules, perception, planning, and navigation, and c) videos of indicative field deployments presented in the paper.
2	Video	Filename: 01_full_stack_evaluation_aerial_robot.mp4. This video shows the recording and visualizations of the field experiments evaluating the full stack on the aerial robot as presented in Section 4.4.1. The robot is deployed in an underground mine, a forest, and a ship cargo hold, evaluating the exploration and inspection behaviors.
3	Video	Filename: 02_full_stack_evaluation_ground_robot.mp4. This video shows the recording and visualizations of the field experiments evaluating the full stack on the ground robot as presented in Section 4.4.2. The robot is deployed in an underground mine and a university building, evaluating the exploration behavior in narrow and large scale environments.
4	Video	Filename: 03_navigation_evaluation.mp4. This video shows the recording and visualizations of the field experiments evaluating the navigation module as presented in Section 4.3. The navigation module is tested in a waypoint navigation task and in the presence of moving obstacles demonstrating the usefulness of the multi-layered safety approach.
5	Video	Filename: 04_slam_evaluation.mp4. This video shows the recording and visualizations of the field experiments evaluating the multi-modal SLAM component of the perception module as presented in Section 4.2.1. The multi-modal SLAM is evaluated in datasets including a) flying in self-similar and dimly lit tunnels, b) flying over a self-similar frozen lake, and c) handheld dataset in a university campus containing area filled with fog.
6	Video	Filename: 05_reasoning_evaluation.mp4. This video shows the recording and visualizations of the field experiments evaluating the VLM-based reasoning component of the perception module as presented in Section 4.2.2. The module is tested on two datasets a) the campus dataset from the SLAM evaluation, and b) the ground robot mission in the university building. The video shows the open vocabulary object detection and binary Q&A capabilities of the module.

**Table 8.** Index of multimedia extensions.